

Universität des Saarlandes



Fachrichtung Physik

# Deformability-Induced Effects of Red Blood Cells in Flow

---

Dissertation  
zur Erlangung des Grades  
des Doktors der Naturwissenschaften  
der Naturwissenschaftlich-Technischen Fakultät  
der Universität des Saarlandes  
von

**David Alexander Kihm**

---

Saarbrücken

2021



Tag des Kolloquiums: 19.11.2021

Dekan: Univ.-Prof. Dr. Jörn Walter

Berichterstatter: Univ.-Prof. Dr. Christian Wagner  
Univ.-Prof. Dr. Rolf Pelster

Vorsitz: Univ.-Prof. Dr. Jochen Hub

Akad. Mitarbeiter: Dr. Herbert Wolf



## Abstract

To ensure a proper health state in the human body, a steady transport of blood is necessary. As the main cellular constituent in the blood suspension, red blood cells (RBCs) are governing the physical properties of the entire blood flow. Remarkably, these RBCs can adapt their shape to the prevailing surrounding flow conditions, ultimately allowing them to pass through narrow capillaries smaller than their equilibrium diameter. However, several diseases such as diabetes mellitus or malaria are linked to an alteration of the deformability. In this work, we investigate the shapes of RBCs in microcapillary flow *in vitro*, culminating in a shape phase diagram of two distinct, hydrodynamically induced shapes, the croissant and the slipper. Due to the simplicity of the RBC structure, the obtained phase diagram leads to further insights into the complex interaction between deformable objects in general, such as vesicles, and the surrounding fluid. Furthermore, the phase diagram is highly correlated to the deformability of the RBCs and represents thus a cornerstone of a potential diagnostic tool to detect pathological blood parameters. To further promote this idea, we train a convolutional neural network (CNN) to classify the distinct RBC shapes. The benchmark of the CNN is validated by manual classification of the cellular shapes and yields very good performance.

In the second part, we investigate an effect that is associated with the deformability of RBCs, the lingering phenomenon. Lingering events may occur at bifurcation apices and are characterized by a straddling of RBCs at an apex, which have been shown *in silico* to cause a piling up of subsequent RBCs. Here, we provide insight into the dynamics of such lingering events *in vivo*, which we consequently relate to the partitioning of RBCs at bifurcating vessels in the microvasculature. Specifically, the lingering of RBCs causes an increased intercellular distance to RBCs further downstream, and thus, a reduced hematocrit.

## Zusammenfassung

Um die biologischen Funktionen im menschlichen Körper aufrechtzuerhalten ist eine stetige Versorgung mit Blut notwendig. Rote Blutzellen bilden den Hauptanteil aller zellulären Komponenten im Blut und beeinflussen somit maßgeblich dessen Fließeigenschaften. Eine bemerkenswerte Eigenschaft dieser roten Blutzellen ist ihre Deformierbarkeit, die es ihnen ermöglicht, ihre Form den vorherrschenden Strömungsbedingungen anzupassen und sogar durch Kapillaren zu strömen, deren Durchmesser kleiner ist als der Gleichgewichtsdurchmesser einer roten Blutzelle. Zahlreiche Erkrankungen wie beispielsweise Diabetes mellitus oder Malaria sind jedoch mit einer Veränderung dieser Deformierbarkeit verbunden. In der vorliegenden Arbeit untersuchen wir die hydrodynamisch induzierten Formen der roten Blutzellen in mikrokapillarer Strömung *in vitro* systematisch für verschiedene Fließgeschwindigkeiten. Aus diesen Daten erzeugen wir ein Phasendiagramm zweier charakteristischer auftretender Formen: dem Croissant und dem Slipper. Aufgrund der Einfachheit der Struktur der roten Blutzellen führt das erhaltene Phasendiagramm zu weiteren Erkenntnissen über die komplexe Interaktion zwischen deformierbaren Objekten im Allgemeinen, wie z.B. Vesikeln, und des sie umgebenden Fluids. Darüber hinaus ist das Phasendiagramm korreliert mit der Deformierbarkeit der Erythrozyten und stellt somit einen Eckpfeiler eines potentiellen Diagnosewerkzeugs zur Erkennung pathologischer Blutparameter dar. Um diese Idee weiter voranzutreiben, trainieren wir ein künstliches neuronales Netz, um die auftretenden Formen der Erythrozyten zu klassifizieren. Die Ausgabe dieses künstlichen neuronalen Netzes wird durch manuelle Klassifizierung der Zellformen validiert und weist eine sehr hohe Übereinstimmung mit dieser manuellen Klassifikation auf.

Im zweiten Teil der Arbeit untersuchen wir einen Effekt, der sich direkt aus der Deformierbarkeit der roten Blutzellen ergibt, das Linging-Phänomen. Diese Linging-Ereignisse können an Bifurkationsscheiteln zweier benachbarter Kapillaren auftreten und sind durch ein längeres Verweilen von Erythrozyten an einem Scheitelpunkt gekennzeichnet. In Simulationen hat sich gezeigt, dass diese Dynamik eine Anhäufung von nachfolgenden roten Blutzellen verursacht. Wir analysieren die Dynamik solcher Verweilereignisse *in vivo*, die wir folglich mit der Aufteilung von Erythrozyten an sich gabelnden Gefäßen in der Mikrovaskulatur in Verbindung bringen. Insbesondere verursacht das Verweilen von Erythrozyten einen erhöhten interzellulären Abstand zu weiter stromabwärts liegenden Erythrozyten und damit einen reduzierten Hämatokrit.

## List of author's publications

- A. GUCKENBERGER\*, A. KIHM\*, T. JOHN, C. WAGNER, AND S. GEKLE  
*Numerical-experimental observation of shape bistability of red blood cells flowing in a microchannel*  
Soft Matter **14**(11) (2018), pp. 2032-2043  
(\* equal contribution)
- A. KIHM, L. KAESTNER, C. WAGNER, AND S. QUINT  
*Classification of red blood cell shapes in flow using outlier tolerant machine learning*  
PLoS Computational Biology **14**(6) (2018)
- C. BÄCHER, A. KIHM, L. SCHRACK, L. KAESTNER, M. W. LASCHKE, C. WAGNER, AND S. GEKLE  
*Antimargination of Microparticles and Platelets in the Vicinity of Branching Vessels*  
Biophysical Journal **115**(2) (2018), pp. 411-425
- L. HERTZ, S. RUPPENTHAL, G. SIMIONATO, S. QUINT, A. KIHM, A. ABAY, P. PETKOVA-KIROVA, U. BOEHM, P. WEISSGERBER, C. WAGNER, M. W. LASCHKE, AND L. KAESTNER  
*The Evolution of Erythrocytes Becoming Red in Respect to Fluorescence*  
Frontiers in Physiology **10** (2019)
- S. HIMBERT, M. J. BLACKER, A. KIHM, Q. PAULI, A. KHONDKER, K. YANG, S. SINJARI, M. JOHNSON, J. JUHASZ, C. WAGNER, H. D. H. STÖVER, AND M. C. RHEINSTÄDTER  
*Hybrid Erythrocyte Liposomes: Functionalized Red Blood Cell Membranes for Molecule Encapsulation*  
Advanced Biosystems **4**(3) (2020)
- A. KIHM, S. QUINT, M. W. LASCHKE, M. D. MENGER, T. JOHN, L. KAESTNER, AND C. WAGNER  
*Lingering Dynamics in Microvascular Blood Flow*  
Biophysical Journal **120**(3) (2021), pp. 432-439
- A. RABE\*, A. KIHM\*, A. DARRAS\*, K. PEIKERT\*, G. SIMIONATO\*, A. K. DASANNA\*, H. GLASS, J. GEISEL, S. QUINT, A. DANEK, C. WAGNER, D. A. FEDOSOV, A. HERMANN, AND L. KAESTNER  
*The erythrocyte sedimentation rate and its relation to cell shape and rigidity of red blood cells from chorea-acanthocytosis patients in an off-label treatment with dasatinib*  
Biomolecules **11**(5) (2021), p. 727  
(\* equal contribution)



## Eidesstattliche Erklärung

Hiermit versichere ich an Eides statt, dass ich die vorliegende Arbeit selbstständig und ohne Benutzung anderer als der angegebenen Hilfsmittel angefertigt habe. Die aus anderen Quellen oder indirekt übernommenen Daten und Konzepte sind unter Angabe der Quelle gekennzeichnet. Die Arbeit wurde bisher weder im In- noch im Ausland in gleicher oder ähnlicher Form in einem Verfahren zur Erlangung eines akademischen Grades vorgelegt.

---

Ort, Datum

---

David Alexander Kihm

Gewidmet Mathilde Kihm, in liebevoller Erinnerung.

# Contents

<b>Introduction</b>	<b>1</b>
<b>1 Background</b>	<b>9</b>
1.1 Blood and the cardiovascular system . . . . .	9
1.1.1 Red blood cells . . . . .	10
1.1.2 Thrombocytes . . . . .	11
1.1.3 Leukocytes . . . . .	12
1.1.4 Plasma . . . . .	12
1.2 Hemodynamics and hemorheology . . . . .	13
1.2.1 Mechanistic properties of RBCs . . . . .	13
1.2.2 Axial migration of deformable particles: Balance of forces . . . . .	14
1.2.3 Fåhræus effect . . . . .	16
1.2.4 Fåhræus-Lindqvist effect . . . . .	18
1.2.5 RBC partitioning at bifurcations: The Zweifach-Fung effect . . . . .	19
1.3 Navier-Stokes equation . . . . .	20
1.3.1 Low Reynolds number regimes . . . . .	21
1.4 Pressure driven flow in a rectangular channel . . . . .	22
<b>2 Materials and methods</b>	<b>25</b>
2.1 Preparation of blood suspensions . . . . .	25
2.2 Microfluidics . . . . .	26
2.3 Fabrication of microfluidic devices . . . . .	27
2.3.1 Design of the microfluidic device . . . . .	28
2.4 Experimental setup . . . . .	30
2.4.1 Image acquisition . . . . .	31
2.4.2 Single particle tracking algorithm . . . . .	32
<b>3 Shape phase diagram of flowing RBCs in microchannels</b>	<b>35</b>
3.1 Introduction . . . . .	35
3.2 Experimental setup . . . . .	36
3.3 Modeling the RBC dynamics in silico . . . . .	36
3.4 Experimental results . . . . .	37
3.4.1 Shape phase diagram of flowing RBCs . . . . .	40
3.4.2 Axial distribution of RBCs in the microchannel . . . . .	41
3.5 Numerical results . . . . .	43
3.5.1 Shape phase diagram of flowing RBCs . . . . .	44
3.5.2 Axial distribution of RBCs in the microchannel . . . . .	46
3.6 Discussion of in vitro and in silico results . . . . .	47
3.6.1 Comparison of shape phase diagrams . . . . .	47

3.6.2	Comparison of axial positions of RBCs . . . . .	51
3.7	Summary . . . . .	52
<b>4</b>	<b>Neural network approach for classification of RBC shapes</b>	<b>53</b>
4.1	Introduction . . . . .	53
4.2	Aspects of artificial neural networks . . . . .	54
4.3	State of the art in artificial intelligence . . . . .	55
4.3.1	Classification of biological cells . . . . .	55
4.4	Architecture of the neural network . . . . .	56
4.4.1	Image preprocessing . . . . .	59
4.4.2	Prerequisites and limitations . . . . .	60
4.4.3	Implementation details . . . . .	60
4.4.4	Acquisition and characteristics of training data . . . . .	62
4.4.5	CNN output and benchmark . . . . .	63
4.5	Summary . . . . .	68
<b>5</b>	<b>Lingering dynamics of red blood cells in vivo</b>	<b>71</b>
5.1	Introduction . . . . .	71
5.2	Architecture of microvascular beds . . . . .	73
5.2.1	Constituent vessels in the microcirculation and Murray's law . . . . .	73
5.2.2	Angiogenesis . . . . .	74
5.3	Experimental setup for in vivo measurements . . . . .	75
5.3.1	Animal preparation . . . . .	75
5.4	Image analysis and data acquisition . . . . .	76
5.4.1	Image processing . . . . .	76
5.4.2	Parameter estimation using the maximum-likelihood approach . . . . .	78
5.5	Results . . . . .	79
5.5.1	Void durations: The impact of lingering . . . . .	81
5.5.2	Lingering frequency . . . . .	82
5.5.3	Additional bifurcation geometries . . . . .	84
5.5.4	Deformation of RBCs in the vicinity of bifurcations . . . . .	89
5.6	Discussion . . . . .	91
5.7	Summary . . . . .	94
	<b>General Conclusion and Perspectives</b>	<b>97</b>
	<b>Bibliography</b>	<b>101</b>
	<b>Appendix</b>	<b>117</b>
A	List of devices and consumables . . . . .	117

# Introduction

Among all organs in the human body, blood is the most delocalized one, consisting of a dense aqueous solution of blood plasma, solubles, and cellular entities. Despite being delocalized, the overall blood amount contributes roughly to 7% to the body weight, and thus forms the second largest organ besides the skin. An optimal perfusion of the blood throughout the complex network of blood vessels in the body is a key component to ensure a proper health state from the primordial embryonic state onwards. The red blood cells (RBCs) form the major constituent of all cellular compounds in the suspension, and therefore, the bulk blood flow is governed by the physical properties and behavior of RBCs [1–4]. Physiologically, severe problems are associated with a failure or disturbance of this perfusion. The blockage of entire vessels due to thrombi are known to occur in all parts of the vasculature, and has a fatal impact on the health state, leading to ischemia and myocardial infarctions, the most pronounced cause of deaths in developed countries [5].

Apart from the physiological interest, blood as a model fluid has reached the status of a *drosophila* in the field of biological fluid dynamics due to its remarkable physical properties in coincidence with its relative simplicity regarding the internal RBC structure. As a non-Newtonian liquid, whole blood shows a shear-thinning behavior due to the presence of RBC aggregates [6–8]. With increasing shear stress, the external forces overcome the binding forces, leading to a subsequent break-up of these aggregates.

Such features of blood have been studied extensively throughout scientific history, culminating in the dedicated branches of hemodynamics and hemorheology. However, alongside the thriving development of microscopy techniques and related analytical methods, the impact of blood research has grown extensively. Due to this development, the initial focus on macroscopic phenomena and coarse-grained approaches has shifted towards rather fine-grained investigations on a single cell level in recent years. Despite this progress, a holistic picture of blood-related phenomena is still lacking, as results found in vivo are unmatched in vitro, and in silico, and vice versa.

The analysis of blood in vitro has been a major diagnostic procedure to gain insight into the body functions and reactions to embodied pathogens. However, the procedures typically involve the analysis of blood samples in stasis, such as e.g. blood smears, or in simple geometries, such as in erythrocyte sedimentation protocols. A driven blood suspension enlarges the parameter space towards the accessibility of dynamic blood parameters. Albeit the existence of sophisticated apparatuses yielding blood parameters even on a single cell scale, they typically require pre-treatment of the specimen as e.g. staining. Allegedly, these protocols do not alter the mechanistic properties of RBCs; nevertheless, they do not provide fundamental physical insight into the measurement procedure and are less cost-effective.

A crucial parameter to maintain the blood flow, even in highly concentrated suspensions, is their deformability, i.e., the ability to alter the shape depending on the underlying forces. As a determinant for the fluid-particle interaction, a fundamental knowledge of the deformability is desired, but still lacking. In collective phenomena of RBC suspensions, the deformability of RBCs is known to have a tremendous impact, e.g. in the context of lateral migration

of rigidified RBCs in flow. Even the axial distribution of single RBCs in channels is highly influenced by the deformability of each RBC, as the shape is governed by the applied flow regimes. In vivo, this change in deformability is, among other factors, correlated with the age of individual RBCs and is supposed to be responsible for their removal of the blood flow in the spleen [9, 10]. Hence, if the sensible equilibrium between the RBC production rate and the removal rate is disturbed, anemic states arise.

In lab-on-a-chip devices, profound knowledge of such axial distributions can be employed in cell sorting apparatuses, and in general, for the development of clinical devices and diagnostic tools. We, therefore, investigate straight microfluidic channels through which a highly diluted RBC suspension is perfused. Based on the microscopic footage we construct a shape phase diagram.<sup>1</sup>

Apart from the direct consequence on morphology and correlated axial position in straight channels, the deformability also affects the distribution of RBCs within the microvascular network. As they tend to migrate towards annular regions in proximity to the vessel centerline, they leave a cell-depleted layer close to the endothelium. At bifurcating vessels, this phenomenon leads to a disproportionate partitioning of RBCs in the respective daughter branches, known as the Zweifach-Fung effect [11, 12]. However, in the physical explanation of this effect, no particular investigations have been carried out to study the single-cell behavior of RBCs at the apex. Recent *in silico* studies address cell partitioning with a focus on RBCs that linger at apices, eventually leading to a piling of subsequent RBCs. In vivo, no corresponding studies exist so far, although the phenomenon itself is well known in intravascular physiology. A qualitative and quantitative analysis of the flow characteristics in presence of lingering RBCs could help to unravel open questions in the design of realistic *in vitro* networks and serve as a benchmark for the state-of-the-art in *in silico* approaches. Additionally, these cellular scale effects might have a severe impact on the distribution of RBCs in the living organism and since it they are linked to a strong deformation of RBCs, lead to a discrepancy of tissue oxygen supply in health and disease.

This thesis is organized as follows: In chapter 1, the scientific background of the blood constituents, their mechanical and biological properties, and physical aspects of flow in low Reynolds regimes is provided. Basic principles and phenomena are discussed with regard to the collective phenomena of blood suspensions.

On the basis of this physical description, we develop the metrological procedures and manufacturing protocols in chapter 2. However, we restrict these experimental setup descriptions to the main features, and additional information about specific adjustments accounting for the distinct experiments are presented alongside each chapter, respectively.

Chapter 3 focuses on *in vitro* experiments of RBCs in flow. Therefore, straight microfluidic channels with rectangular cross-sections are connected to a reservoir containing a diluted suspension of RBCs. With the aid of a pressure-driven flow, we then study the shape and position of RBCs as they flow through these capillaries, whose dimensions are in the range of individual RBCs' diameters. Depending on the imposed flow speed, the RBCs take on two characteristic shapes: A symmetric shape, also termed *croissant*, and an asymmetric shape, termed *slipper*. A resulting shape phase diagram is then compared to the outcome of tailored *in silico* approaches.

Based on the experimental data acquired in the *in vitro* experiments subject to chapter 3,

---

<sup>1</sup>The term phase diagram is used as a descriptor of morphological states of RBCs in a steady Poiseuille flow, and does not coincide with the prevalent usage of this expression in the context of equilibrium configurations in thermodynamics.

we develop a classification of the cell shapes based on artificial intelligence. A sophisticated convolutional neural network has been designed and trained to fulfill the specific needs for classifying biological cells. As a result, we obtain an objective, unbiased classification algorithm reducing the human input and increasing the performance. We evaluate the outcome with respect to the manual classification, serving as a benchmark. These features are the topic of chapter 4.

In the following chapter 5, the blood flow in the microcapillaries of living rodents is discussed. In contrast to the straight microfluidic channels being the subject of the previous chapters, we now focus on the influence of RBCs resting at a bifurcation apex on the subsequent bloodstream. We show evidence that the disproportionate partitioning of RBCs, known as the Zweifach-Fung effect, even underpredicts the real disproportion, which is achieved when the previously mentioned, so-called lingering phenomena are taken into account.



## Literature review

The deformability of red blood cells (RBCs) is a key aspect to ensure proper perfusion of distal tissue regions in the body of vertebrates, as this property allows RBCs to alter their shape and pass through constrictions smaller than their equilibrium size [13–17]. Furthermore, a change in the deformability of mature RBCs is linked to their eventual removal in the spleen [18, 19], as well as to the release of ATP [20].

Affected by this physiological importance, the mechanistic properties of RBC suspensions under flow have been investigated extensively. Yet, the variability of geometries in the circulatory system of living beings is mirrored by the vast parameter space of vessels employed *in vitro* and *in silico*, ranging from few microns in diameter up to several millimeters. Apart from the hard-core interaction with the vessel walls' narrow confinements, the intricate interplay of forces acting on suspended RBCs under imposed flow conditions itself can lead to deformations of RBCs, depending on the prevailing flow conditions. In microcapillaries, the most commonly reported cell shapes are the discocyte shape, the axisymmetric croissant, and the asymmetric slipper shape. The term *croissant* is used here distinctively from the term *parachute*, which is reserved for rotationally symmetric shapes ubiquitous in cylindrical channels [21].

Experimentally, these shapes have been reported both *in vivo* and *in vitro*, yet in the context of low hematocrits with nonetheless abundant intercellular interactions [22–31]. Dilute suspensions in microconfined flows, where the RBCs can be regarded as isolated cells, are only scarcely investigated with a focus on these hydrodynamically induced shapes [32, 33]. Goldsmith and Marlow [34] investigated the orientation and deformation of RBCs in tubes with diameters between  $30\ \mu\text{m} - 100\ \mu\text{m}$ , i.e., *much* greater than the individual RBCs' size. Similarly, Gaehtgens *et al.* [24] provided one of the first investigations of converged RBC shapes in glass capillaries with inner diameters in ranging from  $5\ \mu\text{m} - 12\ \mu\text{m}$  and proved the existence of non-axisymmetric shapes, resembling slippers, for a set of confinements. Employing stereomicroscopy, Bagge *et al.* [35] confirmed the existence of this slipper-like shapes *in vitro*. Further conducted *in vitro* experiments noticed the existence of hydrodynamically induced shapes without exploiting any configuration space of the flow parameters [36–39], but rather focusing on transient states during time-dependent flows [40, 41], or qualitatively comparing them to characteristic shapes found *in vivo* [25, 42].

Despite all these scattered results, no systematic experimental investigations of these hydrodynamically induced shapes have been conducted so far. A phase diagram, yet in pure shear flow in a cone-plate geometry of a rheometer, has been proposed by Lanotte *et al.* [150]. By *in situ* application of glutaraldehyde, they hardened RBCs under shear conditions and analyzed the cells *a posteriori*. A manifold of shape categories could be identified for varying shear rates, including multilobated cells. However, the regime of applied shear rates translates into pseudo-shear rates in Poiseuille flow corresponding to a mean flow velocity of  $u \lesssim 2\ \text{mm s}^{-1}$  for an exemplary cylindrical tube with a diameter of  $10\ \mu\text{m}$ .

Similarly, Abkarian *et al.* [17] provided a semi-quantitative phase diagram of symmetric and asymmetric cell shapes, respectively, for flow velocities greater than  $10\ \text{mm s}^{-1}$  in cylindrical

channels. They specifically focused on the influence of the viscosity contrast  $\lambda_{\text{visc}}$ , which has been tuned by viscosity adaptation of the ambient fluid, but generally obeys  $\lambda_{\text{visc}} \lesssim 0.3$ . Tsukada *et al.* [43] investigated rectangular ducts with an aspect ratio of ca. 1.5 (width approx.  $9 \mu\text{m}$ ) and flow velocities  $1 \text{ mm s}^{-1} \lesssim u \lesssim 2 \text{ mm s}^{-1}$ , noticing that parachutes are the prevalent shapes in this regime.

Due to the complex modeling and limited computational resources, theoretical models have been restricted historically to 2D models, employing vesicles [44], or axisymmetric RBCs [45, 46]. Nowadays, 2D models are still used to investigate migration behavior of RBCs [47], and despite their simplicity, reveal rich dynamics up to the occurrence of deterministic chaos [48]. In 2D, the viscosity ratio is a key determinant of the terminal shape. Kaoui *et al.* [49] constructed a phase diagram with the sole branch for highest velocities dedicated to axisymmetric shapes for  $\lambda_{\text{visc}} = 1$ . Tahiri *et al.* [50] revealed the coexistence of these axisymmetric shapes and slipper shapes upon a change to  $\lambda_{\text{visc}} = 5$ . Albeit this indication of modeling RBC flows with realistic, i.e., physiological viscosity ratios  $\lambda_{\text{visc}} = 5$  [51–53], recent 3D simulations in microconfined flow employed a viscosity ratio of internal and external viscosity of the RBC corpuscles of  $\lambda_{\text{visc}} = 1$  [27, 54, 55], or even  $\lambda_{\text{visc}} \lesssim 0.3$  [56].

A joint numerical-experimental approach has been performed by Secomb *et al.* [47]. The in vitro setup consisted of a cylindrical tube with a diameter of  $8 \mu\text{m}$ , through which a dilute RBC suspension is advected with a velocity of ca.  $1.25 \text{ mm s}^{-1}$ . This setup is mirrored in silico by a bounded Poiseuille flow in 2D with otherwise identical dimensions. They revealed a rudimentary form of shape bistability in the sense that cells initiated at the channel center yielded a terminal croissant shape. On the contrary, cells that started at an off-centered position with respect to the channel axis ended up as slippers.

In 2005, Noguchi *et al.* [54] qualitatively obtained a shape phase diagram of RBCs flowing in cylindrical ducts with diameters of  $9.2 \mu\text{m}$ , employing a realistic 3D model in silico. A key observation has been the transition of discocytes to parachutes at a critical velocity, which in turn depends approximately linearly on the mechanistic parameters of the cells.

A fine-grained phase diagram has been proposed by Fedosov *et al.* [55]. They simulated the flow of RBCs through cylindrical tubes with varying confinements and shear rates and recorded the steady RBC shapes. They specifically identified four shapes that are pooled into four adjacent regions in their phase diagram, the slipper and the parachute shape, as well as tumbling discocytes and a shape category, termed snaking shape, referring to an oscillating movement of discocytes close to the channel axis. The existence of the latter has also been established independently via 2D simulations [49]. Interestingly, Fedosov *et al.* tuned the elastic parameters of the RBC capsules, which resulted in qualitatively very different phase diagrams, however, the viscosity ratio has been set to the unphysiological value of  $\lambda_{\text{visc}} = 1$ , and in addition, the imposed flow velocities are in a rather low regime, obeying  $0.2 \text{ mm s}^{-1} \lesssim u \lesssim 1 \text{ mm s}^{-1}$ .

Conclusively, experimental observations indicate the formation of slippers with increasing velocities in microconfined flow and the absence of this shape upon decreasing the flow strength [17, 32, 57]; however, a systematic investigation contributing to a holistic picture of the hydrodynamically induced shapes is still missing. Analogously, the imposed flow velocities in silico are either in a regime far from the physiological one or comprise rather low velocities. Additionally, most models impose unphysiological viscosity ratios rendering a comparison with in vitro results a challenging task. Hence, the development of lab-on-a-chip devices exploiting the potential alterations in RBC deformability as a diagnostic biomarker is ultimately linked to the aforementioned systematic analysis.

Albeit the implementation of straight cylindrical or rectangular channels already reveals rich

phenomena that are associated with the elastic parameters of the RBCs, the comparison with realistic microvascular beds *in vivo* is limited since they exhibit curvilinear channel segments that are interconnected via bifurcations and confluences. Carr *et al.* [58] revealed the importance of the sequential topological structure and the resulting history of the hematocrit profiles as a key contribution to plasma skimming. Thus, recent studies focus on physiological predictions based on complications such as e.g. stenosed vessels [59] or curved microvessels [60]. *In vivo* investigations of blood flow historically developed to assess physical mesoscopic or macroscopic parameters, such as pressure distributions or hematocrit profiles [61–63]. Similarly, the influence of such parameters has been characterized systematically *in vitro* [64]. The pioneering work of Schmid-Schönbein *et al.* [65] focused on the formation of the cell-free layer and the resulting trajectories of RBCs in the vicinity of vascular bifurcations. However, they reliably predicted time-dependent hematocrit distributions based on a one-dimensional model.

The seminal work by Pries *et al.* [66], relying on *in vivo* observations of blood flow in bifurcating vessels, led to a heuristically derived formula to explain the observed skewed hematocrit profiles. The latter have been identified to contribute to plasma skimming, i.e., the advection of hematocrit profiles through bifurcation sites. A second contribution to flux partitioning is given by intercellular interactions and cellular deformations, termed cell screening in the entirety. Even though first probabilistic models [11, 12] provided insights into the disproportionate partitioning of RBCs at bifurcation sites, later referred to as the Zweifach-Fung effect, they failed to account for the finite-sized effects arising from the particulate nature of RBCs. In fact, the classical disproportionate partitioning they predicted (i.e., the RBC flux is relatively increased with respect to the flow rate) and which is regularly observed *in vivo* is also contrasted by reports of an even partitioning of RBCs according to the flow rates in bifurcating vessel geometries in the cat mesentery [63] or even the inverse partitioning behavior, both *in vivo* [65, 66], and *in vitro* [67–69].

Novel *in vitro* studies are typically oriented towards the development of biomedical applications to utilize the non-uniform RBC distribution in microvessels to achieve a phase separation [70] or, to the very least, an increased disproportion of hematocrits [56]. The hematocrit partitioning for two sets of RBCs with varying deformability, the physiological one and a set of RBCs with increased stiffness, emulating malaria-infected cells, has been elucidated by Li *et al.* [71]. Tripathi *et al.* [72] demonstrated the efficiency of plasma-skimming microfluidic devices based on the Zweifach-Fung effect. They even outmatched any previous passive phase separation by extending the formerly accepted maximal channel sizes by two orders of magnitude, i.e., *much* greater than the particle size. Based on these findings, the basic principles have been developed further with sophisticated arrangements of microvessels [73]. In contrast to bulk flow properties and their macroscopic distribution, only a few studies address the flow of isolated RBCs or small clusters of RBCs [74].

Balogh *et al.* [75] mimicked a realistic, 3D microvascular network *in silico*. They observed a phenomenon of RBCs straddling at the apex of a bifurcation, which eventually culminates in a piling up of subsequent RBCs further upstream. These lingering events are shown to be one of the key mechanisms contributing to the final partitioning throughout the vascular network in a second study employing identical *in vivo*-like networks [76]. Lingering is further proven to cause a spatially inhomogeneous wall shear stress at bifurcation sites, which in turn is known to be a chief catalyst of angiogenesis. In recent 2D simulations, this lingering could be evoked by tuning the flow rates of the adjacent daughter branches of a feeding vessel. Yet, the lingering itself has not been quantified but was rather obtained as a byproduct [74]. Qualitatively, a straddling of RBCs at bifurcation apices resembling the previously noted lingering

phenomenon has also been observed in a further study; however, they only considered one unique geometry exhibiting a symmetric opening angle between the two daughter branches, and thus, the findings are incommensurable to the actual topology in vivo [77]. Ye *et al.* [78] qualitatively observed a state of RBCs at a symmetric bifurcation apex in silico that resembles the lingering phenomenon without further quantitative analysis.

In sum, no systematic studies addressing the impact of lingering in vivo, and in vitro, respectively, exist in the scientific literature to provide a compliant description of the lingering phenomenon, which has been proven to be of major importance in silico for the advection of RBCs throughout the microvasculature. Since the lingering is an inherent feature of deformable entities, we conjecture a correlation between alterations of elastic parameters of RBCs and the resulting lingering events.

# Chapter 1

## Background

The transport of cellular components through the complex plumbing network in the human body and microfluidic channels is subject to the physical principles of hydrodynamics. These principles are at the focus of this chapter, providing an overview of the governing mechanisms and derived phenomena. Additionally to the physical background, physiological and biological aspects of blood and blood flow are provided. Concerning the overall complexity, we restrict the discussion to the main characteristics and provide a more fine-grained approach in the respective chapters of this work.

### 1.1 Blood and the cardiovascular system

For the development of living beings on earth, a working metabolism is a key factor. This metabolism consists roughly of an intake of nutrients and soluble gases and a discharge of waste. On a more fine-grained scale, the nutrients have to be transported to the cells inside the body. While this transport can be achieved solely by diffusion for unicellular living beings, the evolution of pluricellular life such as vertebrates would have been impossible without active transport processes. In the case of human living beings, this active process is performed by the heartbeat, transporting oxygen-enriched blood from the lung towards the organs and tissues through a complex network of vessels, the cardiovascular system. As Schrödinger stated in his famous essay “What is life” [79], living beings evade the status of thermodynamical equilibrium by homeostasis, an adaptive self-regulating process, yielding an increase in entropy of the coupled surroundings.

For vertebrates such as human beings, this is ensured by the blood flow, which is responsible for the heat transfer within the body limits, which itself can be adjusted by vasodilation and vasoconstriction, respectively. The blood flow is organized in a way that it is enriched with oxygen in the alveoli of the lungs and then transported to the heart, from where it is flowing in arteries. These arteries then divide up into vessels of smaller diameters, the arterioles. Arterioles themselves divide up into the capillary bed, which is embedded into the tissues and responsible for the gas and nutrient exchange to these as well as the organs. The capillaries merge again into bigger venules, and these merge into veins, finally delivering the carbon dioxide-rich blood towards the lung. The oxygen binds chemically onto the hemoglobin molecule encapsulated in erythrocytes, also termed red blood cells (RBCs).

RBCs form the main cellular constituent of whole blood, with a volume fraction of approx. 44 % on average, depending on interindividual factors such as sex. Other cellular components are composed of leukocytes or white blood cells (WBCs), respectively, and platelets. Together, their volume fraction in whole blood is about 1 %. The remaining 55 % is the blood plasma,

which is an aqueous solution of 93 % water, with dissolved proteins, monosaccharides, ions, and vitamins among further nutrients and gases.

In vivo, the blood components form a suspension, whereas due to the influence of gravity and a difference in densities, they separate ex vivo. This sedimentation is a reversible process, whereas RBCs form irreversible aggregates in the case of blood clotting, caused by the activation of platelets. In the presence of macromolecules such as Dextran and Fibrinogen, RBCs form reversible aggregates resembling a stack of coins and often termed rouleaux [80], in contrast to these irreversible aggregates. Under the influence of shear forces, these rouleaux may break up and are responsible for the reported shear-thinning behavior of blood. The magnitude of these shear forces spans several orders of magnitude for the entire cardiovascular system, depending on the vessel type and size. Accordingly, the mean flow velocity differs for the various vessel types, as is noted in Table 1.1.

**Table 1.1:** Typical dimensions of human vessel types, with according mean velocities and wall shear rates, given by  $\dot{\gamma} = 4u/r$ , with the tube radius  $r$ , and the velocity  $u$ . Data reproduced from reference [80]

vessel type	diameter (mm)	$\bar{u}$ (mm s <sup>-1</sup> )	wall shear rate (s <sup>-1</sup> )
aorta	16 – 32	600	150 – 300
artery	2 – 6	150 – 500	200 – 2,000
arteriole	0.04	5	1000
capillary	0.005 – 0.01	0.5 – 1	400 – 1,600
post-capillary venule	0.02	2	800
venule	0.1	5	400
vein	5 – 10	150 – 200	120 – 320
vena cava	20	100	40 – 60

### 1.1.1 Red blood cells

The genesis of human RBCs, the so-called erythropoiesis, occurs in the bone marrow and comprises a multitude of differentiated cell types from erythropoietic stem cells to the final mature RBCs [81]. During this process, the structural composition of RBCs changes, most notably leading to the absence of a nucleus. Thus, the integrity of RBCs is reduced to a membrane encapsulating the internal fluid, termed cytosol.

Separating the cytosol from the outer plasma, the RBC membrane is composed of a lipid bilayer containing a manifold of embedded proteins that are linked to a triangular spectrin network on the inner membrane layer. This bilayer largely contributes to the RBC's bending resistance while rendering its surface area practically inextensible, even under deformations [82–84]. In fact, persistent area dilatations in the order of approx. 4 % of the total surface area are known to rupture the cell body [85, 86]. Remarkably, the RBC exhibits a significantly increased tolerance of area dilations, if the latter are only short-lasting [87]. The spectrin network, on the other hand, is responsible for the resistance against two-dimensional shear deformations.

Healthy RBCs obey a biconcave discocyte shape, with a diameter of 7.8  $\mu\text{m}$  and a height between 1.5  $\mu\text{m}$  in the center up to 2.2  $\mu\text{m}$  at the rim, cf. Fig. 1.1. On average, they cover a

surface area of ca.  $135 \mu\text{m}^2$  [32, 88], and an enclosed volume of ca. 90 fl [32].

A valid parametrization of the RBC has been proposed by Evans and Fung [89, 90], yielding

$$z(r) = \pm \frac{R}{2} \sqrt{1 - \left(\frac{r}{R}\right)^2} \left[ C_0 + C_1 \left(\frac{r}{R}\right)^2 + C_2 \left(\frac{r}{R}\right)^4 \right], \quad (1.1)$$

the  $z$ -axis as symmetry axis and  $r = (x^2 + y^2)^{1/2}$ . Under physiological conditions, the RBCs obey a tonicity of 300 mOsm, yielding the parameters  $R = 3.91 \mu\text{m}$ ,  $C_0 = 0.81 \mu\text{m}$ ,  $C_1 = 7.83 \mu\text{m}$  and  $C_2 = -4.39 \mu\text{m}$ .

Normalizing the RBC volume by the volume of a sphere with the given surface area, one obtains the corresponding reduced volume of  $\mathcal{V} \simeq 0.6$ . During its lifespan of 120 days, the membrane vesiculates partially, resulting in a reduction of both the surface area and the enclosed volume. Linked to these changes is an increase of the reduced volume, from  $\mathcal{V} = 0.58$  to  $\mathcal{V} = 0.64$ . By measuring the hemoglobin content in the RBCs during the aging, it is known that relatively more water than hemoglobin is lost, leading to an increased concentration in the cytosol.

By a change in osmolality of the surrounding media, morphological changes of the RBC can be induced. Whereas for a hypotonic solution, the RBC takes on a mono concave cup-like shape, spicules are formed in a hypertonic solution. The first shape is called stomatocyte, and the latter is referred to as echinocyte. Apart from the change in osmolality, these transitions can also be caused by a change in pH, a change in the concentration of ATP, and by the addition of special drugs, such as sodium salicylate (yielding echinocytosis), or chlorpromazine (yielding stomatocytosis). In between these two extreme morphological shape classes, there is no discrete transition from one to the other, but rather a continuous shape transformation, also known as the stomatocyte-discocyte-echinocyte (SDE) scale.

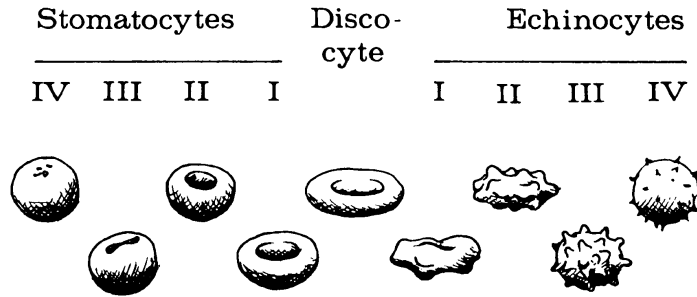


**Figure 1.1:** Various categories of RBC shapes, from stomatocytes to echinocytes, also referred to as the SDE-scale. In between, the discocyte shape which is the most common RBC cell shape under physiological conditions in healthy human individuals. The image has been adapted from reference [91].

### 1.1.2 Thrombocytes

Thrombocytes, also termed platelets, form the third moiety of solid blood constituents. These cell fragments originate from megakaryocytes and are responsible for the hemostasis in wounds and blood coagulation in general. With a diameter up to  $3 \mu\text{m}$ , they are significantly smaller than RBCs and WBCs, albeit their biconvex oblate shape resembles the morphology of RBCs. As a physical prerequisite to perform hemostasis, they need to adhere to the ruptured endothe-

lium, where they induce a complex coagulation cascade [92] after being activated, alongside a morphological transformation process.

In contrast to physiological clot formation, pathological states arise when the blood coagulation occurs within the vessel, causing thrombi that eventually separate from the endothelium and circulate in the vasculature. These thrombi then lead to a potential blockage of the vessel and a malfunction of the oxygen supply or, in the worst case, entire tissue death. One determinant in the origin of these thrombi is the apparent shear stress in the vessel geometry, leading to a conformational change of proteins, which in turn triggers the activation of platelets [93, 94]. This mechanoenzymatical trigger is also known to hinder the action of biomedical devices and therefore, needs to be accounted for when designing such apparatuses [95, 96].

### 1.1.3 Leukocytes

With a volume fraction of approximately 1%, leukocytes, or WBCs, are responsible for immune response. Given their relatively low occurrence in whole blood, their role in the bulk rheological properties of blood is negligible. Unlike RBCs and platelets, they are nucleated cells with organelles and form several subcategories of functional classes, such as e.g. monocytes, and lymphocytes. The latter form the basis of the adaptive immune response in vertebrates as they retain the immunological memory. Flowing in the vascular network, they need to address infection sites, or in general, sites of adhered pathogens effectively. Due to their physical properties, they tend to marginate in the bloodstream, i.e., unlike RBCs, they preferentially migrate to axial positions close to the vessel walls [97, 98]. Although this margination phenomenon has been subject to numerous studies, basic information about the physical origin is still lacking. In context to alterations of lymphocyte concentrations in infectious states and the influence of this change on the lateral migration remains unanswered. In the microvascular system, leukocytes play an important role and are known to substantially alter the flow resistance due to their presence [99, 100]. Similarly, they are further associated with a partial or entire blockage of vessels in the microvascular bed [101].

### 1.1.4 Plasma

The formed constituents of blood are immersed in an aqueous solution, the blood plasma. The plasma itself is composed of water with a volume fraction of 90% and the rest being composed of solubles such as dissolved respiratory gases, ions (mainly  $\text{Na}^+$ ,  $\text{K}^+$ , and  $\text{Ca}^{2+}$ ), metabolites, polysaccharides, and proteins ranging from small molecules up to several kDa in molecular mass. The latter are known to cause the reversible aggregation of RBCs under physiological conditions in stasis and under low, i.e., up to few  $\text{s}^{-1}$  shear rates. A break-up of these rouleaux into single RBCs under higher shear rates is responsible for the shear-thinning behavior of whole blood, and thus, the rheology of whole blood is governed to a large extent by the presence of these proteins. Albeit the plasma is known to exhibit a constant shear viscosity of  $\mu_{\text{plasma}} = 1.2 \text{ mPa s}$  at a body temperature of  $37^\circ\text{C}$ , recent investigations indicate that under pure extensional flow, the plasma exhibits a visco-elastic behavior [102].

## 1.2 Hemodynamics and hemorheology

### 1.2.1 Mechanistic properties of RBCs

It is the relative simplicity of human RBCs that makes them an ideal model object to study deformable microscopic entities, and the absence of a nucleus and further organelles renders them a membraneous sack. This structural simplicity is linked to investigations of two iconic microparticles: the vesicle and the capsule. While artificial capsules typically contain a liquid encapsulated by a polymerized surface, vesicles consist of a lipid bilayer surrounding the internal liquid phase. This lipid bilayer exhibits a thickness of approx. 5 nm in artificial vesicles up to approx. 100 nm in the case of RBCs [103], and consists of two adjacent sheets of lipid molecules whose hydrophilic heads are oriented towards the external and the internal fluid phase, respectively, while the hydrophobic tails are facing each other in the intramembranous volume.

The thin shell of capsules endows them with an extensible surface while maintaining the total volume of the object. As a consequence, the dynamics of capsules in flow are governed by their shear modulus as well as the area dilatation. Bending, on the other hand, although existent, plays a minor role. In contrast to capsules, the lipid bilayer of vesicles is endowed with a high area dilatation modulus, rendering the surface area practically constant. Together with the volume conservation, they must be non-spherical to be able to deform under external forces. A second difference is the absence of the shear elasticity in the case of vesicles.

Instead, the bending rigidity plays an important role in the vesicle dynamics [104]. RBC structurally share distinct properties with each of these aforementioned model objects, and therefore, they are often modeled as either one or as a combination of both models. A special case arises in 2D *in silico* approaches, where the shear elasticity is absent, thus rendering vesicles as the prevalent model system. Several experimental investigations study the complex vesicle dynamics in flow, exhibiting rich phenomena such as tumbling (TB), tank-treading (TT) or vacillating breathing states [105–112]. These findings are also reported *in silico* [48, 49, 113–115]. Tumbling motion is characterized by a periodic flipping of the inclination angle versus the flow field, as sketched in Fig.1.2. If the vesicle undergoes a TB motion,

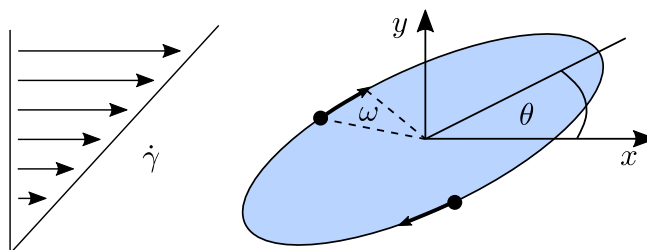


**Figure 1.2:** Sketch of two common scenarios of vesicle motion in linear shear flow. For lower shear rates  $\dot{\gamma}$ , the vesicle exhibits a tumbling motion, i.e., the inclination angle  $\theta$  is time-dependent. As the shear rate  $\dot{\gamma}$  increases, the lipid bilayer of the vesicle exhibits a tank-treading movement, such that fixed points on the membrane (depicted as black dots) are non-stationary. In contrast to the former case, the inclination angle in the latter case remains constant. In the transition regime between TB and TT motion, the membrane is performing a TT motion, however, the inclination angle is typically oscillating around the flow direction. The latter is known as vacillating breathing motion.

the relative position of the membrane is fixed apart from minor fluctuations. As the flow

strength increases, this TB motion changes into the TT motion upon surpassing a critical shear rate [111]. Then, the membrane starts to rotate around the steady inner fluid, i.e., the inclination angle of the vesicle remains constant. In between these two regimes, a combination of both motions is observed, known as swinging motion or vacillating breathing. This state is characterized by a rotating membrane while the inclination angle of the vesicle oscillates around the flow direction. However, we stress that these considerations are only a rough scheme and the motion of the vesicle depends on additional parameters, such as e.g. the reduced volume of the vesicle and the Reynolds regime (cf. section 1.2.2).

To model the vesicle dynamics in flow, one has to have a profound knowledge of the membrane constitutive equations in order to determine its physical properties and to reliably predict the fluid-structure interaction. At rest, the vesicle shape results from a minimum energy principle, which is also applicable when exposed to external forces such as under flow conditions. In the case of vesicles and RBCs, the bending energy associated with the existence of the lipid bilayer is of major importance. Although various approaches exist to quantify the bending energy, the one which is most common throughout the scientific literature and also employed in the joint numerical-experimental approach as proposed in chapter 3, is the Helfrich-Canham [116, 117] formulation. In this model, the energy density per unit area,  $\epsilon_B$ , has been obtained phenomenologically as

$$\epsilon_B = 2\kappa_B(H(\mathbf{r}) - H_0)^2 + 2\kappa_G K, \quad (1.2)$$

with the bending modulus  $\kappa_B$ , the Gaussian modulus  $\kappa_G$ , the Gaussian curvature  $K(\mathbf{r})$ , the spontaneous curvature  $H_0$ , and the local mean curvature  $H(\mathbf{r})$ . The latter is hereby defined as the arithmetic mean of both principal curvatures  $H(\mathbf{r}) = 1/2 (R_1^{-1}(\mathbf{r}) + R_2^{-1}(\mathbf{r}))$ ,  $\mathbf{r} \in S$ . The total energy of the vesicle is then computed as

$$E_B = \oint 2\kappa_B(H(\mathbf{r}) - H_0)^2 dS + \oint 2\kappa_G K dS. \quad (1.3)$$

According to the Gauss-Bonnet theorem [118], the closed surface integral over  $K$  is a topological invariant and can thus be omitted to facilitate the calculations. With the aid of a multitude of various measurement techniques, the elastic modulus  $\kappa_B$  is found to fit in the regime  $\kappa_B = 0.1 \times 10^{-19} \text{ J} - 3 \times 10^{-19} \text{ J}$  [32].

The bending energy and associated bending forces have a tremendous impact on the vesicle dynamics, as is pointed out in the subsequent section. However, the congruence of experimental and numerical is essential to maintain a holistic view on the elastic properties of RBCs. Due to the inherent complexity of modeling RBCs in flow, *in silico* approaches are benchmarked by the experimental counterparts and therefore, the study of the governing fluid-structure interaction is of high interest.

### 1.2.2 Axial migration of deformable particles: Balance of forces

Although the flow of all entities in the blood is governed by deterministic physical equations, the complex interplay between cells and endothelium as well as the interactions among adjacent cells still reveals unknown phenomena. In contrast to a continuous liquid phase, the particulate nature of blood implies collective phenomena as a result of heterogeneous partitioning. If one considers the perfusion of blood suspensions through a pipe, analytic expressions are scarcely derived. However, as a rough approximation, we might consider the

fluid-structure interaction of rigid spherical objects in Poiseuille flow.

One of the very first systematic investigations on this subject has been performed by Segré and Silberberg [119, 120]. They studied the properties of dilute suspensions consisting of neutrally buoyant, non-deformable spherical particles immersed in a liquid and driven through a pipe with circular cross-section and the radius  $R_{\text{tube}} = 11.2$  mm. Since two particle sizes have been employed, with diameters 0.8 mm, and 1.71 mm, respectively, the Reynolds numbers are in a range of  $3 \lesssim \mathcal{Re} \lesssim 17$ , given the fluid viscosity of  $\mu = 400$  mPa s and the imposed fluid velocities. For comparably low flow velocities, they found that the particles remain randomly distributed across the tube diameter. Similarly, they observed a random distribution for higher velocities when the distance from the input reservoir was small. However, for high velocities and observation points far enough from the entrance, they discovered an annular region at around  $r = 0.6R_{\text{tube}}$  from the channel axis, where the particle concentration is significantly increased. Although they revealed a linear dependency of this effect on the Reynolds number and analogously, on the squared fluid velocity, they ultimately failed to explain the true origin of this effect. Nevertheless, they conjectured that due to the aforementioned dependencies, the origin of the transverse forces acting on the suspended particles is inertially driven.

Saffman [121] concluded from observing particles in bounded shear flow that the existence of a wall is a key ingredient due to an additional drag force acting on the particles effectively reducing their individual speed below that of the surrounding fluid. Ho and Leal [122], however, identified this velocity difference to play only a minor role as long as the particles are neutrally-buoyant. Instead, the lateral migration of the suspended particles can be understood as a linear combination of a wall-induced lift force  $F_{\text{lw}}$ , and a second force  $F_{\text{ls}}$  opposing the former  $F_{\text{lw}}$ . While  $F_{\text{lw}}$  originates from a disturbance of the velocity field by the presence of the particle and its interaction with the wall,  $F_{\text{ls}}$  emerges from the interaction of the disturbed flow field with the curvature of the flow, yielding a net force towards regions with higher shear rates. In Fig. 1.3, these forces are schematically depicted. Di Carlo *et al.* [123]

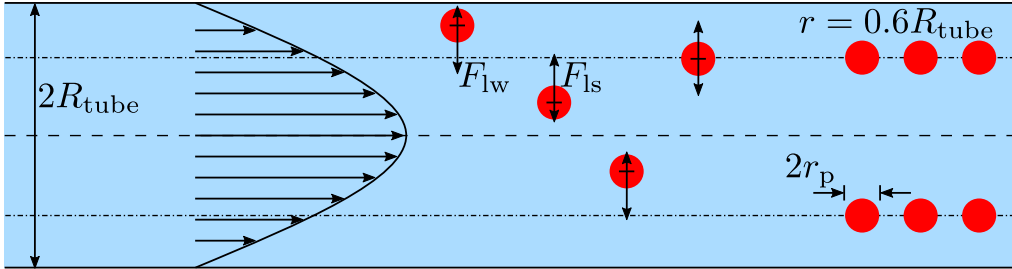


**Figure 1.3:** Schematic flow of a dilute particulate suspension at an intermediate to high Reynolds number regime  $\mathcal{Re} = \mathcal{O}(10^1)$ , similar to the experimental setup of Segré and Silberberg [119, 120]. Two forces act on the particles in the Poiseuille flow profile, the shear-induced lift force  $F_{\text{ls}}$  being directed away from the channel axis, and the wall-induced lift force  $F_{\text{lw}}$ , pointing towards the channel center (dashed line). The strength of both forces depends on the relative lateral position of the particles, yielding a tubular pinch effect at a distance  $r = 0.6R_{\text{tube}}$ , indicated by the dash-dotted lines.

revised the scaling behavior of the transversal lift force acting on a solid particle obtained for confinements  $2r_p \simeq w$ , with  $r_p$ , and  $w$  being the particle radius and the channel width (of a quadratic cross-section), respectively, culminating in the expression

$$F_{\text{ls}} = f_1 \frac{\rho u^2 (2r_p)^3}{w}, \quad (1.4)$$

for the shear-induced lift force. Additionally, the wall-induced lift force scales as

$$F_{1w} = f_1 \frac{\rho u^2 (2r_p)^6}{w^4}, \quad (1.5)$$

with  $u$  denoting the maximum velocity of the fluid and the fluid density  $\rho$ . The factor  $f_1$  denotes a lift coefficient.

In the limit of  $\mathcal{Re} \rightarrow 0$ , the Navier-Stokes equation reduces to the linear Stokes equation, which has tremendous impact on the qualitatively observed particle movement. Mathematically, the formerly described limit implies a reversibility of the resulting Stokes equation, which in turn disables non-deformable objects to migrate transversally in flow. A more detailed description about Low Reynolds number regimes is presented in section 1.3.1. Indeed, several theoretical studies focus on the necessary flow regimes to observe a transversal migration of suspended particles and concluded that inertia is a crucial ingredient. Experimentally, Goldsmith and Mason [124] even proofed the threshold of  $\mathcal{Re} \leq 10^{-6}$  for the existence of an inertial drift of solid particles towards the channel axis.

Deformable particles such as vesicles, however, adapt their shape to the prevailing flow conditions, causing an impaired particle symmetry, and thus, these deformable entities can migrate in very low Reynolds regimes, where inertial effects are negligible. The lift force exerted on vesicles in shear flow has been quantified experimentally by Abkarian *et al.* [110]. They found for the lift force

$$F_1 = \mu \dot{\gamma} \frac{r_{\text{eff}}^3}{w} f(1 - \mathcal{V}), \quad (1.6)$$

with the shear rate  $\dot{\gamma}$ , the effective particle radius  $r_{\text{eff}}$ , the channel width  $w$ , and a dimensionless function  $f(1 - \mathcal{V})$ , which depends solely on the reduced volume  $\mathcal{V}$  of the vesicle.  $r_{\text{eff}}$  is defined via the vesicle volume  $V$  as  $R_{\text{eff}} = (3V/4\pi)^{1/3}$ .

Kaoui *et al.* [125] showed that 2D vesicles migrate in unbounded Poiseuille flow with Reynolds numbers  $10^{-2} \lesssim \mathcal{Re} \lesssim 10^{-3}$ . Yet, they revealed a different scaling law, with the migration velocity is proportional to the capillary number of the channel and the curvature of the flow profile. Couplier *et al.* [126] similarly found experimental evidence that the migration velocity of vesicles in bounded Poiseuille flow exhibits a power-law  $\propto \dot{\gamma}/y$ , with  $y$  being the lateral position in the flow profile. This scaling behavior has been confirmed by simulations and is the consequence of an intricate coupling between the flow curvature and the induced vesicle shape, which in turn affects the resulting force acting on the vesicle.

Despite the extensive research conducted in the field of vesicle dynamics, a comprehensive formulation is still lacking. This circumstance especially holds for the coupling of cells, such as RBCs, and the fluid, where additional parameters affect the migration.

### 1.2.3 Fåhræus effect

The complex interplay of the previously described forces acting on deformable particles in flow has a tremendous impact on the flow properties of blood suspensions. One of the most prominent phenomena is the formation of annular concentric regions with different particle concentrations when blood suspensions are perfused through straight tubes. Whereas close to the vessel walls, a cell-depleted or even cell-free layer is established, a densely packed region close to the axial core of the tube is maintained.

In his seminal work, Fåhræus conducted experiments on particulate flow in tubes of various

cross-sections [127]. These tubes were connected to a reservoir containing blood suspensions at a discharge hematocrit  $H_D$ , and a collecting reservoir, as depicted in Fig. 1.4. For a

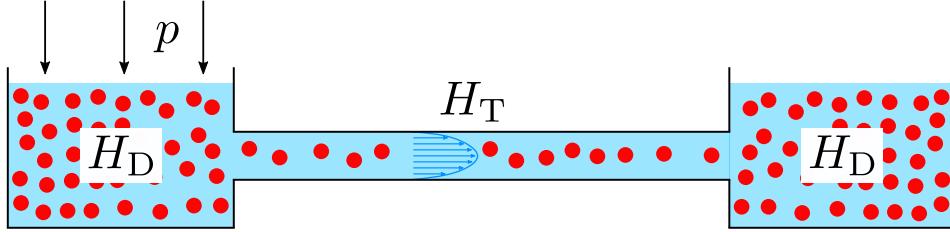


**Figure 1.4:** Illustration of the Fåhræus effect: Two reservoirs containing RBCs are interconnected via a narrow tube, i.e., the diameter of the capillary is in the order of the equilibrium size of RBCs. Cells flowing in the capillary clearly leave a cell-depleted layer close to the tube walls. Thus, they obey a higher mean speed than the surrounding fluid, due to the Poiseuille profile of the flow.

given discharge hematocrit, the measured hematocrit in the vessel, the tube hematocrit  $H_T$  is decreased. Eventually, this phenomenon has been termed the Fåhræus effect. Ongoing investigations revealed a strong non-monotonic behavior with increasing tube diameters and culminate in the empirical equation derived by Pries *et al.* [128] for the tube hematocrit  $H_T$  in glass capillaries:

$$\frac{H_T}{H_D} = H_D + (1 - H_D) (1 + 1.7e^{-0.415D} - 0.6e^{-0.011D}) , \quad (1.7)$$

with the reservoir hematocrit  $H_D$ , and the vessel diameter  $D$  in microns. As can be seen from the graphs displayed in Fig. 1.5, the minimum of this reduced hematocrit is given for vessel diameters in the range of the RBC size. Qualitatively, this relative hematocrit reduction

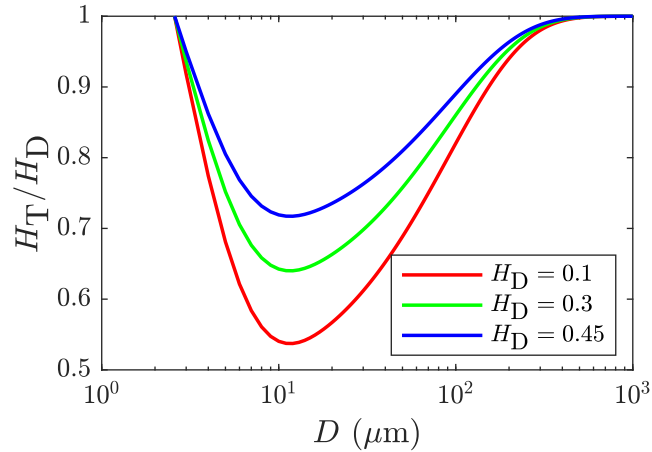


**Figure 1.5:** Reduction of the relative tube hematocrit  $H_T$  due to the Fåhræus effect, according to Eq. (1.7). The normalization factor is given by the discharge hematocrit of the reservoir,  $H_D$ .

in capillaries can be explained by a mass balance analysis: Due to the imprinted Poiseuille profile, the fluid in regions close to the axial core of the tube obeys a higher mean speed than in outer regions. Since the axial core is more densely populated by RBCs, their mean speed is higher than the mean speed of the fluid. Thus, the measured concentration of the

sum of particle volumes and the total volume inside the tube, in the case of blood flow the hematocrit, is decreased with respect to the feeding hematocrit:

$$\frac{H_T}{H_D} \propto \frac{\bar{u}_{\text{blood}}}{\bar{u}_{\text{RBC}}} < 1, \quad (1.8)$$

where  $\bar{u}_{\text{blood}}$  refers to the mean speed of the perfused blood suspension and  $\bar{u}_{\text{RBC}}$  to the mean speed of the RBCs. Interestingly, the effect of relative hematocrit reduction is most pronounced in capillaries with diameters in the range of the equilibrium size of RBCs. For smaller diameters, the CFL vanishes, leading to an increase in reduced hematocrit. On the other hand, the impact of the established CFL on the overall bulk flow is negligible for diameters much larger than the RBC size.

#### 1.2.4 Fåhræus-Lindqvist effect

The biphasic nature of blood and resulting heterogeneities in the particle distribution not only manifests in the former Fåhræus effect but also affects the viscosity of blood suspensions. As the cells tend to migrate to the vessel centerline, they leave a cell-depleted layer in proximity to the channel walls. This CFL serves as a lubrication layer for the bulk blood flow, and thus a decreased viscosity compared to whole blood suspensions. To quantify this drop in viscosity, we define a so-called apparent viscosity  $\mu_a$ . For Newtonian fluids, the Hagen-Poiseuille law (Eq. (1.17)) is valid, stating a proportionality between the volumetric flow rate and the pressure gradient. Since blood suspensions are non-Newtonian, the law does not hold. However, by defining the apparent viscosity  $\mu_a$  as

$$\mu_a = \frac{\pi r^4 \Delta p}{8 Q l}, \quad (1.9)$$

we can relate the hydrodynamic resistance of the fluid to the flow of a Newtonian fluid, translating through a vessel of diameter  $2r$ , length  $l$ , with a volumetric flow rate  $Q$  caused by a pressure gradient of  $\Delta p$ .

However, the impact of this lubrication layer is most pronounced for vessels with a diameter similar to the size of individual RBCs, i.e., around diameters of  $8 \mu\text{m}$ . As the diameter of the vessel increases, the impact of the CFL is negligible, and thus, for vessel diameters  $\gtrsim 300 \mu\text{m}$ , the apparent viscosity is almost constant. On the other hand, as the vessel diameter is less than the individual RBC size, the deformation of the RBC impacts the apparent viscosity, leading to a rapid increase of  $\mu_a$ . This phenomenon has been termed Fåhræus-Lindqvist effect. In Fig. 1.6 the apparent viscosity is depicted for a variety of species and suspending media. This change in suspending media is accounted for by normalizing the apparent viscosity with the outer viscosity of the medium and termed relative apparent viscosity.

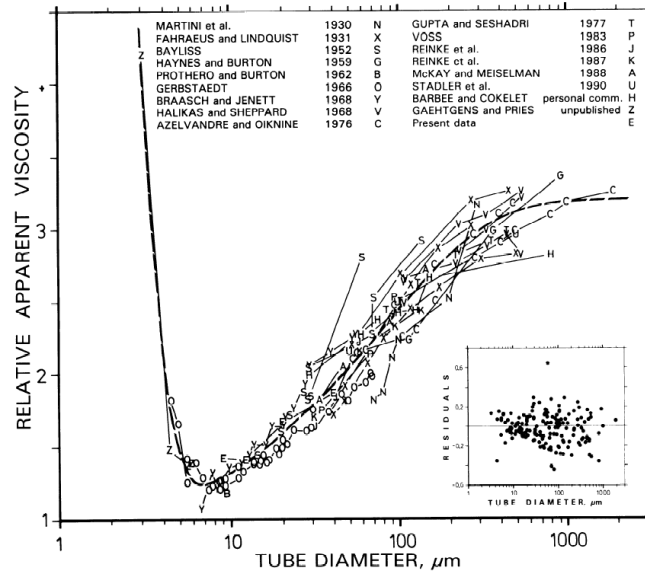


**Figure 1.6:** Relative apparent viscosity  $\mu_{rel}$  of blood suspensions with an adjusted discharge hematocrit of  $H_D = 0.45$ . The suspension is perfused through glass capillaries. The distribution of  $\mu_{rel}$  obeys a minimum at  $\simeq 7 \mu\text{m}$  as a result of the Fåhræus-Lindqvist effect. The image has been adapted from reference [128].

### 1.2.5 RBC partitioning at bifurcations: The Zweifach-Fung effect

The aforementioned effects arising from the particulate nature of blood not only affect the lateral migration of RBCs within curvilinear channels but eventually the distribution of RBCs in networks, i.e., interconnected vessel segments. A crucial parameter in the distribution pattern of RBCs is the bifurcation apex connecting adjacent vessels, where cells end up in either one. Svanes and Zweifach [12] and Fung [11] provided a phenomenological approach to characterize the distribution of suspended particles in bifurcation geometries. They observed that in adjacent vessels the one exhibiting a higher flow rate is entered by relatively more RBCs than its counterpart. The latter vessel thus obeys a decreased hematocrit.

While they ultimately fail to quantify the hematocrit reduction due to this disproportionate partitioning, they developed a physical explanation of this phenomenon. As the fluid approaches the bifurcation site, the streamlines split up according to the flow rates in the daughter vessels. An RBC located in proximity to the bifurcation apex, therefore, experiences a net force due to the skewed force balance of the fluid forces and the finite size of the particle. Statistically, this skewed force profile results in the phase separation effect, commonly referred to as the Zweifach-Fung effect.

Pries *et al.* [66, 134] studied 65 bifurcation sites in the rat mesentery. By means of regression, they obtained an empirical correlation between the partitioning of the blood flow in both daughter vessels and the respective partitioning of RBCs in these vessels. With the parameters  $X = 0.4/d_M$ , and  $B = 1 + 6.98 \times (1 - H_D)/d_M$ , the partitioning function  $\psi$  of RBCs in a symmetrical bifurcation, where both daughter vessels exhibit identical diameters, reads

$$\psi = \begin{cases} 0, & \text{if } \phi < X, \\ 1, & \text{if } \phi > 1 - X, \\ \frac{1}{1 + \left(\frac{\phi - X}{1 - \phi - X}\right)^{-B}}, & \text{otherwise.} \end{cases} \quad (1.10)$$

The dimensionless parameters  $A$  and  $B$  as defined above depend on the discharge hematocrit  $H_D$  in the mother vessel, as well as the diameter of the mother vessel  $d_M$ . Fig. 1.7 indicates the analytical RBC flux in dependence of the blood flow fraction in one arbitrary daughter vessel according to Eq. (1.10). This *classical* phase separation has been reviewed in microvascular

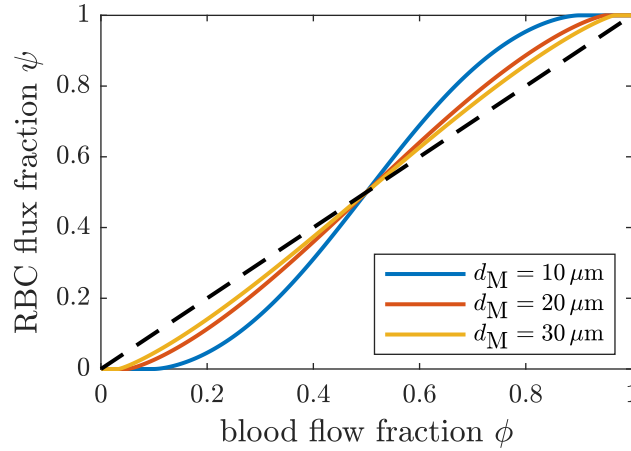


**Figure 1.7:** Illustration of the Zweifach-Fung effect: The disproportionate partitioning of the RBC flux fraction  $\psi$  for a given blood flow fraction  $\phi$  entering the daughter vessel. The black dashed line yields identity, and the solid colored lines are generated according to the empirical formula derived by Pries *et al.* [66, 134], for three different daughter vessel diameters. For the sake of simplicity, a symmetrical bifurcation has been chosen, where the diameters of both branching vessels are identical. The feeding hematocrit in the mother vessel is set to  $H_D = 0.2$ , representing typical physiological values in the microvasculature.

networks in vitro, showing a strong dependence on both the elastic cell parameters as well as the hematocrit [69, 129]. However, due to manufacturing processes and their limitations, these in vitro experiments on a scale  $\lesssim 10 \mu\text{m}$  focusing on vessel networks are surprisingly scarce. Notably, significant progress to investigate cell partitioning has been made recently regarding the development of realistic in vitro networks, consisting of bifurcation cascades [130], and dilating vessels [131, 132].

### 1.3 Navier-Stokes equation

Newton's laws form the deterministic set of equations of motion for solid bodies. Their counterpart in fluid dynamics are the Navier-Stokes equations, obtained in the continuous limit of Newton's laws, i.e., by applying the latter to infinitesimal volume elements. The Navier-Stokes equations can be formulated as a balance of rescaled forces  $\mathbf{f} = \mathbf{F}/V$ ,

$$\mathbf{f}_{\text{inertia}} = \mathbf{f}_{\text{ext}} + \mathbf{f}_{\text{stress}}, \quad (1.11)$$

with the inertial forces  $\mathbf{f}_{\text{inertia}}$ , the external forces  $\mathbf{f}_{\text{ext}}$ , and the stress term  $\mathbf{f}_{\text{stress}}$ . For incompressible fluids, the continuity equation yields  $\nabla \cdot \mathbf{u} = 0$ , and the resulting force balance in Eq. (1.11) can be expressed via the generalized Navier-Stokes equation

$$\rho \partial_t \mathbf{u} + \rho (\mathbf{u} \cdot \nabla) \mathbf{u} = -\nabla p + \mu \nabla^2 \mathbf{u} + \mathbf{f}_{\text{ext}}, \quad (1.12)$$

with the fluid density  $\rho$ , the viscosity  $\mu$ , the velocity field of the fluid  $\mathbf{u}$ , and the pressure gradient  $\nabla p$ .

Written in this form, the inertial forces correspond to the terms on the left hand side, being composed of the variation  $\rho \partial_t \mathbf{u}$ , and the convective acceleration  $\rho (\mathbf{u} \cdot \nabla) \mathbf{u}$ . On the right-hand side of Eq. (1.12), the rescaled forces are composed of a term  $\nabla p$ , taking into account the pressure from the surrounding fluid, the internal force due to viscosity,  $\mu \nabla^2 \mathbf{u}$ , and an external force  $\mathbf{f}_{\text{ext}}$ , e.g. in the case of gravity.

The ratio of inertial forces and viscous forces is a key determinant of the qualitative behavior of fluid flows. If the inertial effects dominate the system, then the flow is considered turbulent. On the other hand, if the viscous forces govern the system, then the flow is considered laminar. To classify the flow, a dimensionless quantity called the Reynolds number  $\mathcal{R}e$  is defined as the quotient of inertial and viscous forces [135], and reads

$$\mathcal{R}e = \frac{\rho l u}{\mu}. \quad (1.13)$$

From Eq. (1.13), the Reynolds number depends on the flow speed  $u = \|\mathbf{u}\|$  being the absolute value of the velocity and a characteristic length scale of the system  $l$ . In the context of particle suspensions, a second quantity is often calculated, the so called particle Reynolds number  $\mathcal{R}e_p$ , given as

$$\mathcal{R}e_p = \frac{(2r)^2}{l^2} \mathcal{R}e. \quad (1.14)$$

The quantity  $\mathcal{R}e_p$  is thus suitable to characterize the influence of a particle's disturbance of the surrounding flow field. To avoid confusions among the quantity defined in Eq. (1.13) and the particle Reynolds number, the former is often termed tube or channel Reynolds number and indexed as  $\mathcal{R}e_c$ . Henceforth, and if not stated otherwise, the term Reynolds number refers to the channel Reynolds number without further mentioning.

In the case of a microfluidic channel with a width and a height, respectively, of  $l = 10 \mu\text{m}$ , through which water ( $\rho = 1,000 \text{ kg m}^{-3}$ ,  $\mu = 1 \text{ mPa s}$ ) is flowing with a speed of  $u = 10 \text{ mm s}^{-1}$ , the Reynolds number yields  $\mathcal{R}e = 10^{-2}$ , which is far below the critical value of  $\mathcal{R}e \simeq 2000$ , marking the transition point from laminar to turbulent flow [136].

### 1.3.1 Low Reynolds number regimes

As the Reynolds number decreases for a system, the influence of viscous forces dominates over the inertial effects. Implications rise from the flow profile itself up to the movement of particles suspended in the fluid. While the flow is turbulent for sufficiently high Reynolds numbers, it becomes laminar for low Reynolds numbers. In this low Reynolds number regime, actively propelling objects such as algae or bacteria can only travel a net distance with non-reciprocal movements. This phenomenon is known as the scallop theorem [137], referring to the motion

of scallops in the sea. By using a time-reversible motion of their shells, namely opening and closing, they are able to maintain a net propulsion while submerged in the sea. However, by increasing the Reynolds number, e.g. by submerging the scallops in fluid with increased viscosity while keeping their size, this net propulsion will stop, indicating the overcome of viscous forces.

## 1.4 Pressure driven flow in a rectangular channel

In the laminar flow regime, i.e. for low Reynolds numbers, inertial effects are negligible. The steady flow is then characterised by  $\partial_t \mathbf{u} \equiv 0$ , and the Navier-Stokes equation for incompressible Newtonian fluids in Eq. (1.12) reduces to the Stokes equation

$$\nabla p = \mathbf{f}_{\text{ext}} + \mu \nabla^2 \mathbf{u}. \quad (1.15)$$

For manufacturing purposes, we are limited to the use of rectangular microchannels in our conducted experiments, as is further described in section 2.3. We therefore restrict the following considerations to such a geometry and the solution to the Stokes equation (1.15) for a rectangular channel of length  $l$ , width  $w$  ( $-w/2 \leq y \leq w/2$ ) and height  $h$  ( $0 \leq z \leq h$ ) is given in this case by [135]

$$u_x(y, z) = \Delta p \frac{4h^2}{\pi^3 \mu l} \sum_{n, \text{odd}} \frac{1}{n^3} \left[ 1 - \frac{\cosh\left(\frac{n\pi y}{h}\right)}{\cosh\left(\frac{n\pi w}{2h}\right)} \right] \cdot \sin\left(\frac{n\pi z}{h}\right), \quad (1.16)$$

where we assume that the fluid flows due to the exerted pressure drop  $\Delta p$  in  $x$ -direction. We further assume without loss of generality that  $h \leq w$ , which holds for our microfluidic channels and can always be maintained in by rotation of the underlying coordinate system for generalized rectangular geometries. In Fig. 1.8, the velocity profile for a rectangular channel is depicted, obeying the dimensions as the one used in the microfluidic experiments. Due to the intricate structure of the velocity profile in rectangular geometries, one typically approximates the flow profile by the parabolic one of cylindrical channels, since deviations are negligible in most cases, as can be seen in Fig. 1.8 (b).

By integrating Eq. (1.16) over the channel dimensions, one obtains the volumetric flow rate  $Q$  as

$$Q = 2 \int_0^{w/2} dy \int_0^h dz u_x(y, z) = \Delta p \cdot \underbrace{\frac{wh^3}{12\mu l} \left[ 1 - \frac{h}{w} \sum_{n, \text{odd}} \frac{192}{(n\pi)^5} \tanh\left(\frac{n\pi w}{2h}\right) \right]}_{1/R_h}. \quad (1.17)$$

The proportionality factor  $R_h$  only depends on the geometric properties of the channel, and is referred to as the hydraulic resistance. The general proportionality between volumetric flow rate and pressure drop in Eq. (1.17) is known as Hagen-Poiseuille's law.

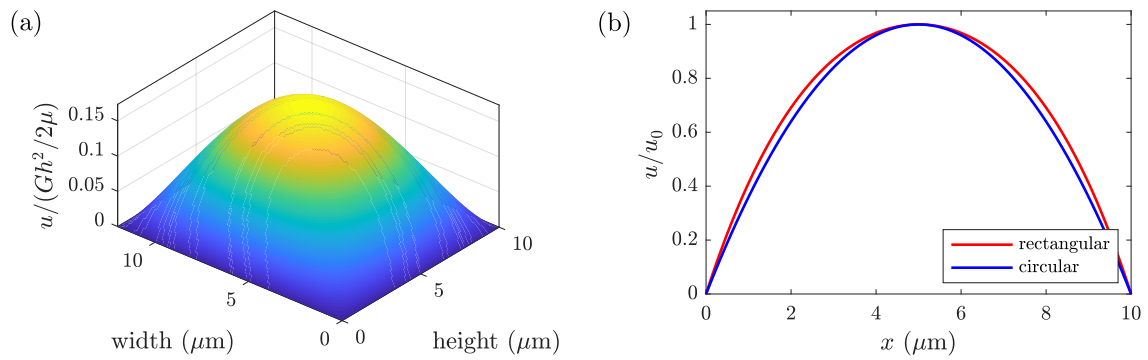


**Figure 1.8:** (a) Laminar flow profile in a microfluidic channel with a width  $w = 12 \mu\text{m}$  and a height  $h = 10 \mu\text{m}$ . The flow speed  $u$  is hereby rescaled by a factor  $Gh^2/2\mu$ , with  $G = -\partial p/\partial x$  being the applied pressure drop per unit length causing the flow. (b) Comparison of imposed flow profiles in channels with a rectangular cross-section as in (a) and a circular cross-section with a diameter of  $10 \mu\text{m}$ , respectively. The flow profile has been obtained in both cases in the channel center. Deviations of both flow profiles are insignificant for both channel geometries.



# Chapter 2

## Materials and methods

This chapter is intended to provide profound background information on the materials and methods that have been employed for the experiments described in the subsequent chapters. The focus is set to cover the main experimental setups, from biological sample preparations to technical imaging specifications. Additional information is provided in the sections of the respective experiments, where special prerequisites and setups have to be accounted for. However, if not stated otherwise, the steps described in the following remain valid.

### 2.1 Preparation of blood suspensions

For all performed in vitro experiments, and if not stated otherwise, the blood withdrawal and preparation followed one distinct protocol. While the extraction of blood from healthy donors is performed according to regulations and protocols that have been approved by the ethic commission of the “Ärztchamber des Saarlandes” [Medical Association of the Saarland] (reference 24/12), the routine for preparing the blood solutions and the handling follow the guidelines by Baskurt *et al.* [138] and will be described in the following.

Blood withdrawal was either realized by a sterile needle prick in the fingertip or by venipuncture and collecting the blood in a sealed vacutainer containing ethylenediaminetetraacetic acid (EDTA) as an anticoagulant. Whereas the total blood amount is governed by skin temperature and exact position of the needle prick in the first case and may vary between ca. 10  $\mu\text{l}$  – 100  $\mu\text{l}$ , the amount is fixed to 9 ml in the latter case. To remove the autologous plasma of the blood sample, gentle centrifugation is carried out for 5 min at 1,500 g. After this step, a pellet of densely packed RBCs has formed on the bottom of the container, with a top layer of autologous plasma and an intermediate layer of WBCs and platelets, also termed buffy coat. Both the supernatant and the buffy coat are then pipetted away and discarded with the remaining pellet being resuspended in the same quantity of isotonic phosphate-buffered saline (PBS), according to [139]. This entire washing process is then repeated three times, cf. Fig. 2.1. After the last centrifugation, 10  $\mu\text{l}$  of the pellet are suspended in a solution of 1 ml PBS and 1 mg bovine serum albumin (BSA), the latter causing an inactivation of the surface of RBCs and thus avoiding the glass slide effect, causing a morphological change of RBCs [140]. Hence, the final blood solution yields a hematocrit of approx. 1%. Since the influence of sex and individual habits may influence the mechanical properties of RBCs and hence lead to non-uniform results throughout the conducted experiments, the blood withdrawal has been performed at different day times and furthermore the blood has been collected from different individuals. In total, blood from three individuals has been used, avoiding any interindividual

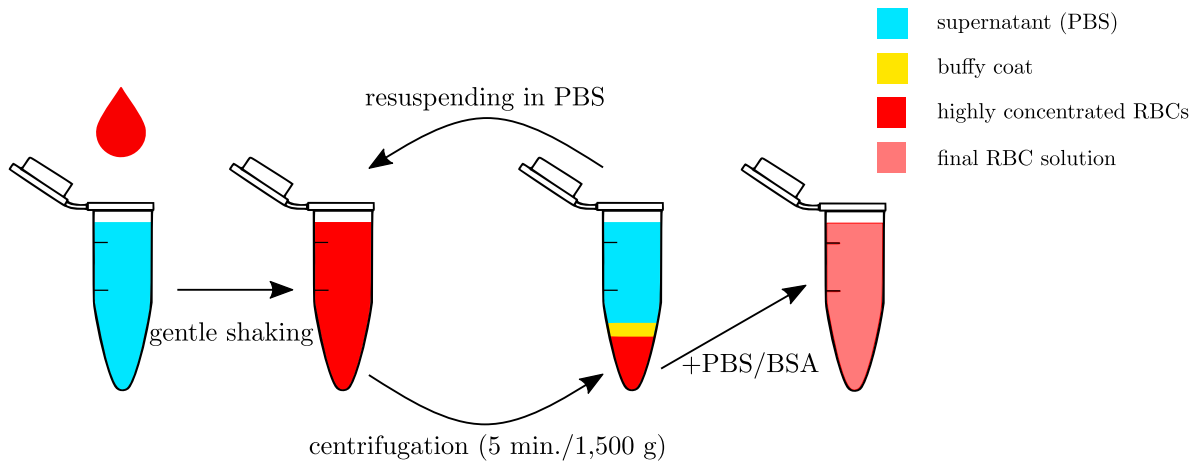


**Figure 2.1:** Blood washing scheme: From left to right, blood from sterile needle prick is suspended in PBS. After gentle shaking, the obtained suspension is centrifuged according to the blood handling guidelines [138]. After centrifugation, a pellet of highly concentrated RBCs formed at the bottom of the Eppendorf tube, which is then resuspended in PBS. The buffy coat, consisting of WBCs and platelets, as well as the supernatant, is discarded. This centrifugation procedure is repeated three times in total. The final blood solution is obtained by diluting the desired amount of the RBC pellet to a solution of 1 ml PBS and 1 mg BSA. For the conducted experiments, we fix the final hematocrit value to approx. 1%.

and intraindividual effects. Between the blood withdrawal and the conduct of the experiment a maximum time span of 3 h is ensured.

## 2.2 Microfluidics

To perform the microfluidic experiments as explained in the following chapter 3, a subtle tool to mimic the capillary vessels in humans is desired. Since the prevalent dimensions of their cross-sections are in the micrometer range, special fabrication techniques are needed to ensure the high precision of the outcome. Several approaches exist to fabricate these capillaries, depending on the complexity of the architecture and the geometrical constraints of the individual microchannels. Conventional techniques comprise mechanical procedures, such as micro-milling [141], embossing or imprinting [142], in contrast to recently developed techniques, ranging from etching procedures [143] to laser micro-channeling [144]. Among all different approaches, an outstanding role in the context of biomedical investigations has become the soft lithography. Numerous advantages are linked to this technique, creating microchannels in polydimethylsiloxane (PDMS). Besides its cost efficiency compared to other techniques, it allows for complex architectures and possesses high biocompatibility. These features culminate in its prevailing status in many current lab-on-a-chip devices. However, due to the inherent manufacturing procedure, one is typically restricted to channels with rectangular cross-sections, although there has been recent progress in developing spherical cross-sections [145].

## 2.3 Fabrication of microfluidic devices

To produce a microfluidic chip utilizing soft lithography, a variety of single processing steps is necessary. The final product will be a negative mold on a silicon wafer, also termed master mold, from where identical copies of the architecture can be replicated using soft elastomers, as the previously described PDMS.

Starting with a silicon wafer, we apply a photoresist, whose thickness is precisely adjusted via spin-coating, see Fig. 2.2 (a), and (b). The light-sensitive photoresist is available in two differing manifestations, specifying their behavior when exposed to light radiation. For our purpose, we use the negative photoresist SU-8, indicating that it hardens under UV exposure, in contrast to a positive photoresist, showing the inverse behavior. A binary lithography mask, consisting of a transparent film containing the imprinted lateral channel geometries, is placed in physical contact with this photoresist. In a subsequent step the assembly is radiated with a collimated UV light source from the top, as depicted in Fig. 2.2 (c). To hold the mask and the wafer in place and prevent any shifts, a glass plate is fixed on top using vacuum suction. By rinsing the illuminated silicon wafer thoroughly with acetone, the unexposed photoresist will be dissolved and removed, leaving a projection of the mask on the substrate of the wafer in the desired thickness, see Fig. 2.2 (d). To further harden the substrate on the wafer, the assembly is baked in the oven at 80 °C, increasing its mechanical strength. The relief structure on the substrate is now the negative mold for the microchannels, and by pouring the soft elastomer PDMS into this mold, we obtain the positive structure of the desired microchannels, see Fig. 2.2 (e). A degassing step in a vacuum-sealed container is necessary to remove bubbles before the entire chip can be cured in the oven at 80 °C for at least two hours prior to being peeled off the mold. The removed cured PDMS contains now the microchannels, except the bottom sealing, see Fig. 2.2 (f). Before attaching the bottom part, the PDMS is cut in shape, i.e. residues from the mold are gently cut off. Additionally, holes are drilled in the reservoirs of the microchannels to allow for connecting tubes to the microfluidics. After these holes are drilled, the chip, as well as a glass cover slide (thickness  $170 \pm 5 \mu\text{m}$ ), are cleaned with the aid of an ultrasonic bath, and then activated in a plasma-cleaner. The activated surfaces are then joined together and the covalent bonding will unify the chip. To increase mechanical resistance, the chip is baked in the oven again for at least two hours at 80 °C.

Although the previous steps in manufacturing microchannels are well-documented, some aspects are hard to control, leading to slight aberrations in the outcome. While the height is adjusted via spin-coating, a subtle change in viscosity due to temperature and aging effects leads to a differing systemic height than desired. Similarly, the lateral dimensions of the structure might be altered due to diffraction at the mask edges, or a falsely collimated UV light beam. For this purpose, the real dimensions of the microchannels need to be measured and may show an imprecision with respect to the desired dimensions. However, once the deviations are acceptable regarding the experimental design, it is appropriate to duplicate the master mold. To this aim, the positive PDMS chip is immersed into an epoxy resin. After hardening, the PDMS can be removed and the resin keeps the negative relief of the channels again, from where steps (e) and (f) in Fig. 2.2 are perpetuated. In this way, the efficiency of the manufacturing process is increased and a copy of the channels is secured.

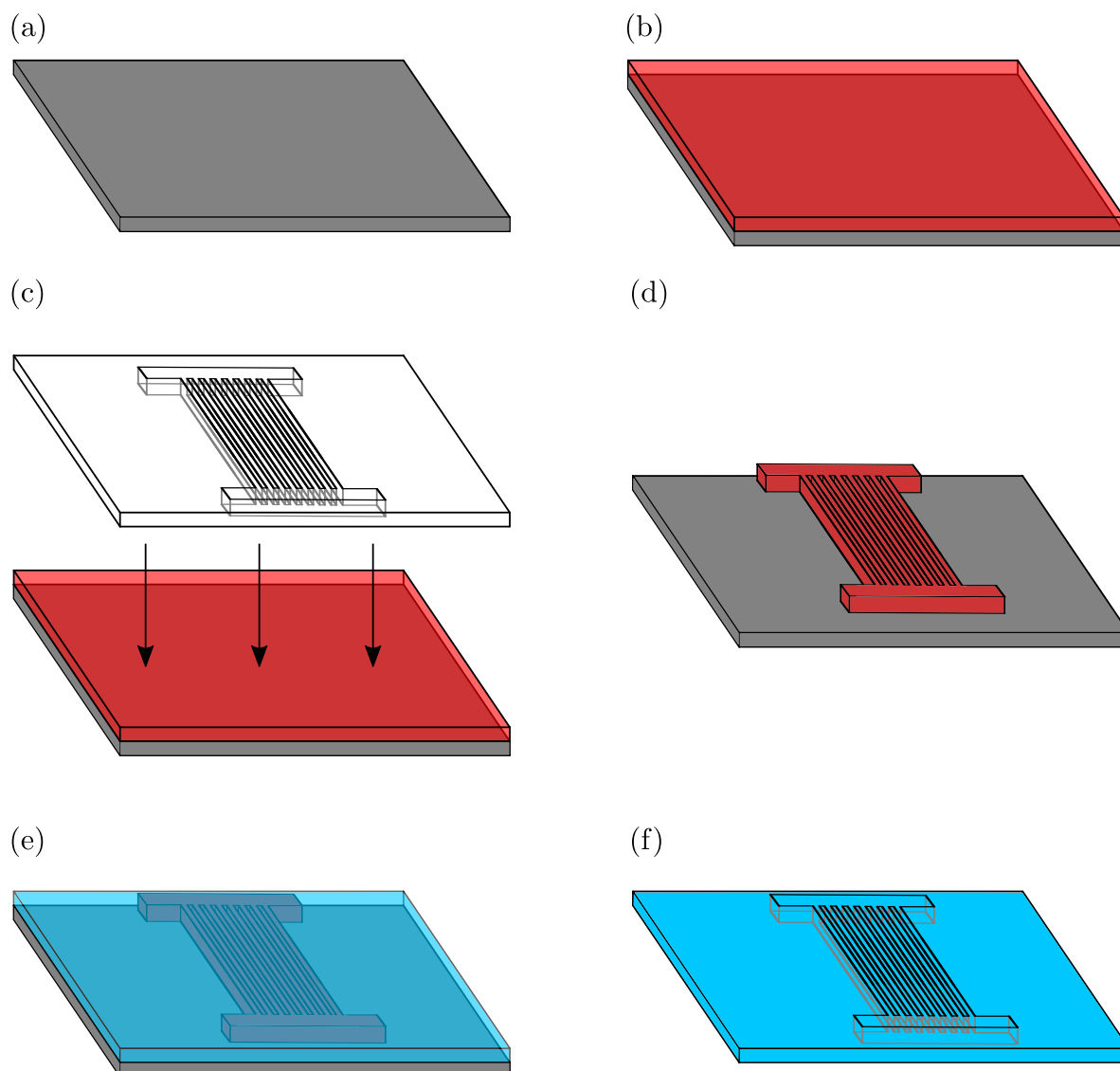


**Figure 2.2:** Schematic of the fabrication of microfluidic devices. (a) Silicon wafer forms the substrate of the photoresist. (b) A photoresist is applied onto a silicon wafer via spin coating to ensure a homogeneous spread and leaving a submillimeter-thick layer of precise height. (c) A binary mask with the desired geometrical constraints is applied onto the photoresist and then exposed to UV light, leading to a partial polymerization of the resist. (d) Using solvents, the photoresist which was not exposed to UV light is rinsed thoroughly. (e) The mold with the relief of the channels is filled with a soft elastomer and then processed in the oven to cure. (f) After removing the elastomer from the mold, the channel structures remain in the PDMS. The next step consists of covalent bonding to a glass slide.

### 2.3.1 Design of the microfluidic device

The microfluidic chip consists of 90 straight channels in parallel with rectangular cross-sections and a length of 4 cm. The entire set of channels is hereby divided into four subsets, each containing channels with varying widths. Starting with the largest cross-section and in decreasing manner, the channel widths are determined as:  $28.7\ \mu\text{m}$ ,  $19.4\ \mu\text{m}$ ,  $15.1\ \mu\text{m}$ , and  $11.9\ \mu\text{m}$ . The

channel heights are given by the height of the substrate and equal  $9.7\mu\text{m}$ . Each channel subset consists of a multitude of either 30 channels in the case of the two widest channels or 15 channels in the two remaining cases. To ensure optimal perfusion of the channels and allowing for an easy connection of the tubing, a reservoir is interconnecting the outlets and the inlets of the channels, respectively. The flow through each channel can be calculated em-

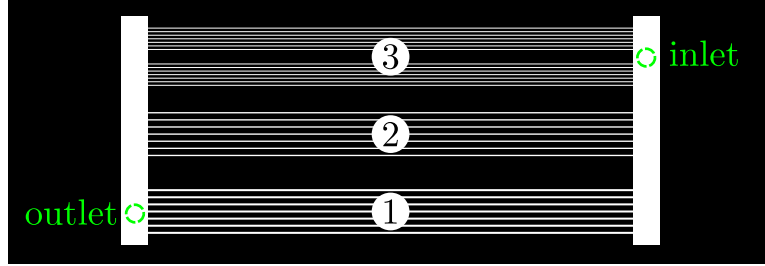


**Figure 2.3:** Design of the microfluidic chip. The channels are divided into four groups, depending on their cross-sections. With decreasing order, the channel widths are  $28.7\mu\text{m}$  (1),  $19.4\mu\text{m}$  (2),  $15.1\mu\text{m}$  (3), and  $11.9\mu\text{m}$  (3). All channels obey the identical relief height of  $9.7\mu\text{m}$ . Liquid inflow towards the channels and outflow of the channels is provided by the reservoirs, respectively, indicated as white vertical bars, with a length of  $\approx 1.0\text{mm}$  and a width of  $\approx 2.0\text{cm}$ .

ploying the hydrodynamic counterpart to Kirchhoff's laws in electrostatics. Analogous to the electrical resistance, the hydraulic resistance is abbreviated with  $R$ , whereas the volumetric flow rate  $Q$  and the pressure drop  $\Delta p$  are the equivalent of the electrical current and the voltage, respectively. The mesh rule and the nodal rule are then given by

$$(a) \sum_{k=1}^M \Delta p_k = 0, \quad (b) \sum_{k=1}^N Q_k = 0. \quad (2.1)$$

We stress that  $M$  is the total number of pressure drops in one mesh and  $N$  is given by the total count of incoming nodes. Together with the Hagen-Poiseuille law in Eq. (1.17), we then find for the volumetric flow rate in each channel  $k$ :

$$Q_k = \frac{\Delta p}{R_k}, \quad (2.2)$$

with the global pressure  $\Delta p$  as applied by the pressure controller and the hydrodynamic resistance  $R_k$  in the  $k$ -th channel. Eq. (2.2) demonstrates the advantage that even in case of a partial blockage of some of the microchannels, the flow rates in the remaining undisturbed channel geometries remain constant. Together with the repetitive design of the channels, we ensure a useful redundancy on one chip.

For a tube with circular cross-section, the hydrodynamic resistance  $R_h$  is given by

$$R_h = \frac{8\mu L}{\pi r^4}, \quad (2.3)$$

and we hence find for the resistance of the employed connection tubing (see section 2.4) a value of  $R_h \approx 9.4 \times 10^{10} \text{Pa}\cdot\text{s}/\text{m}^3$ , where we set the viscosity to  $\mu = 1.0 \text{mPa}\cdot\text{s}$ .

Similarly, the hydrodynamic resistance of a rectangular duct of length  $L$ , width  $w$ , and height  $h$  can be computed via the approximation

$$R_h \approx \frac{12\mu L}{wh^3 \left(1 - 0.63\frac{h}{w}\right)} \quad (2.4)$$

in the regime  $h < w$ . Inserting the numerical values of the channel inlet reservoir, we obtain a resistance of  $R_h \approx 6 \times 10^{11} \text{ Pa}\cdot\text{s}/\text{m}^3$ . Accordingly, we find the resistance of one microchannel with the given dimensions to be  $R_h \approx 2.1 \times 10^{16} \text{ Pa}\cdot\text{s}/\text{m}^3$ . Compared to the resistance of both the inlet reservoir and the connection tubing, the resistance of the channel is five orders of magnitude larger and hence, the contribution of the reservoir and tubing to the overall flow resistance are negligible.

## 2.4 Experimental setup

Once the microchannels are readily manufactured, they are fixed onto an aluminum plate with a rectangular duct to ensure a torsionally rigid underlying structure not provided by the microfluidic chip itself. This aluminum plate is then fixed onto a stage, allowing for precise horizontal positioning under the microscope.

Albeit the tremendous technological developments in the field of microscopy that emerged in the last decades, we use a brightfield microscope (Nikon TE2000-S) to capture the flowing RBCs in the microfluidic channels. For this microscopy technique, light is transmitted through the specimen, and depending on their optical density, they cause attenuation of light and create a contrast in the final footage. Besides its simplicity, we eschew the necessity of staining RBCs, which in turn might lead to structural and mechanical alterations of the cytoskeleton. To suppress any environmental noise, the whole microscopy setup is decoupled from the surroundings via a damping table.

A polyethylene (PE) tubing (outer diameter 1.3 mm, inner diameter 0.9 mm) is inserted in each of the drilled holes towards the channel reservoirs. The approximate length for both the inlet and the outlet tubing is 30 cm. An Eppendorf tube is then connected to the outlet tubing, collecting all the liquid debris after being flown through the microchannels. The inlet tubing on the other hand is connected through a drilled hole in a custom-tailored sample holder providing an airtight sealing of an Eppendorf tube containing the final blood solution according to section 2.1. A second opening in this sample holder is connected to a high-precision pressure controller (Elvesys Elveflow OB1-MkII), providing a stable pressure supply from 0 mbar – 2,000 mbar. The experimental setup including the various steps involved is presented in Fig. 2.4. A high-power red light-emitting diode (LED) is employed in the bright-field illumination unit, delivering a monochromatic light with a wavelength of 640 nm. Using fiber optics, the light is bundled into the optical path of the microscope. This divergent light then passes a condenser lens, rendering it into a convergent light beam to ensure optimal illumination of the specimen. The light which is passing through the object is collected by the objective to create a magnified real image, which is then projected onto the chip of the attached camera.

In the conducted experiments, we primarily seek to resolve the exact shape of flowing RBCs as well as to achieve a high position accuracy. Due to its high magnification and numerical aperture, an oil-immersion objective (Nikon Plan Apo VC 60 $\times$ ) has been used. Given the physical

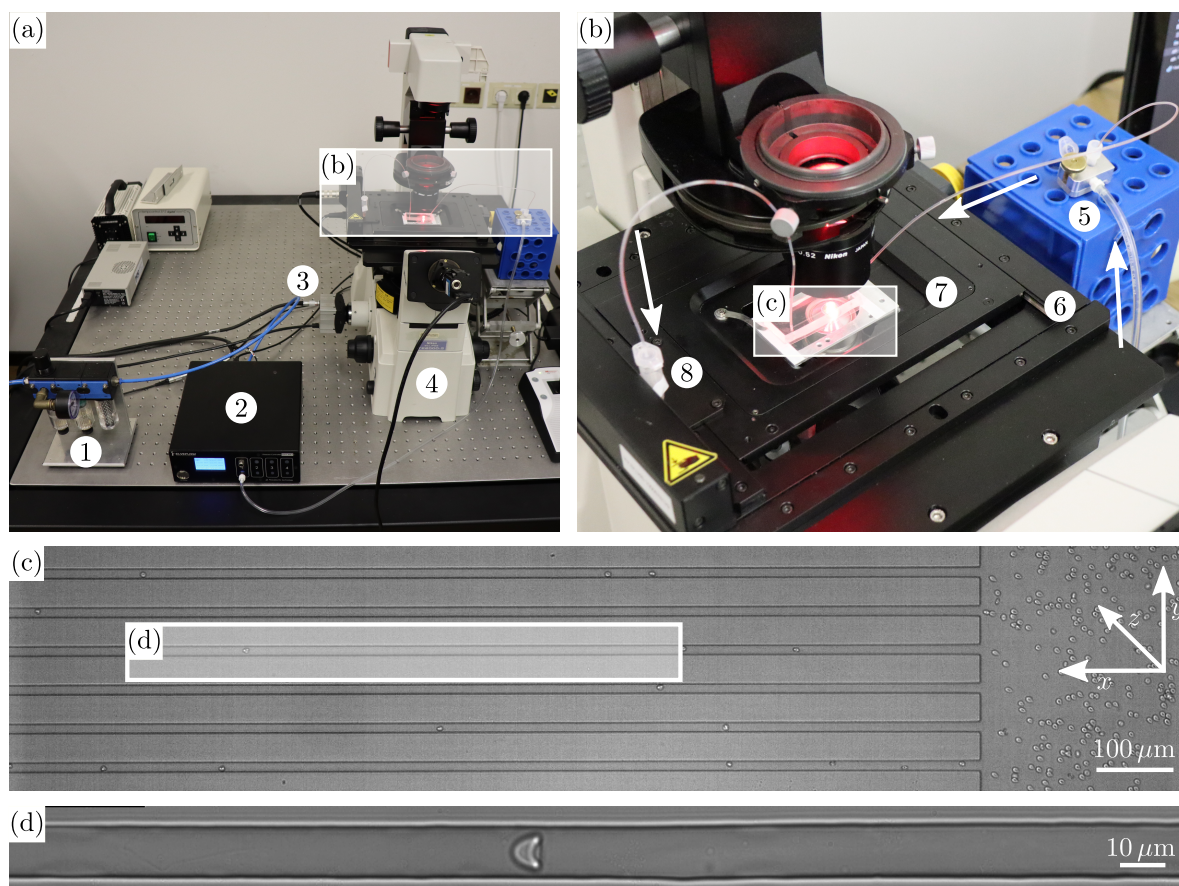


**Figure 2.4:** Experimental setup to study RBCs in microcapillary flow. (a) Pressurized air (1) is fed into a high-precision pressure controller (2), whose output is connected to the sample holder containing the dilute RBC suspension. A brightfield microscope (4) equipped with a high-speed camera (3) is employed to record the footage. (b) Detailed view of the sample holder (5) being connected to the microfluidic chip (7). The outlet of this chip is connected to a waste container (8). To precisely control the positioning of the microfluidic chip, the latter is mounted with all the necessary attachments on a moveable stage (6). White arrows indicate the direction of the blood flow and the pressure gradient, respectively. (c) Snapshot of RBCs in the microchannel at a pressure drop of 200 mbar for illustration purposes. On the right-hand side, the inlet reservoir is partly visible containing inflowing RBCs. (d) Final cropped image with the default magnification capturing a flowing RBC exhibiting a croissant shape.

pixel size of the camera chip,  $14\ \mu\text{m}$ , we achieve a theoretical resolution of approx. 230 nm, which is sufficiently large to resolve the characteristic features of the cellular shapes.

### 2.4.1 Image acquisition

Image series of flowing RBCs in the microfluidic channels were recorded at 50 – 500 fps using a high-speed camera (Fastec HiSpec 1, cf. Appendix A). The actual framerate within this range hereby depends on the set pressure of the pressure controller and hence the mean velocities of the RBCs and is chosen to capture the moving RBCs but suppressing motion blur. The footage is obtained in the so-called *single mode* of the camera, yielding a single image sequence.

The camera is equipped with an internal memory, which makes the acquisition independent of the CPU power since no data stream has to be processed by the operating PC. Albeit the possibility of high-speed image acquisition, the data amount in one recording sequence is limited to the internal memory size of the camera (2 GB). We, therefore, crop a region of interest with the length of the field of view (1280 px) and a height slightly larger than the channel width ( $\approx 100$  px). Theoretically, multiple channels can be recorded by enlarging the region of interest, however, since the intermediate space between neighboring channels is comparably large, this would reduce the net output of recorded cells in one sequence.

## 2.4.2 Single particle tracking algorithm

*The base version of the algorithm has been implemented by Thomas John to trace the movement of microswimmers. Severe adjustments and extensions to adapt the algorithm to the detection and tracking of RBCs have been carried out by the author.*

In contrast to particle imaging velocimetry (PIV), where a frame-to-frame correlation is calculated to obtain the velocity field of tracer particles in a surrounding fluid [146], we apply a single particle tracking (SPT) method to the recorded image sequences. By this technique we do not obtain any detailed information about the flow profile within the channel; however, we are able to extract the necessary velocity and position data of every individual cell and are therefore able to calculate a phase diagram of cell shapes in dependence on cell velocity and axial position within the channel. The SPT algorithm consists of numerous steps and is widely available and documented throughout scientific literature and thus we will only focus on the features of the custom-tailored algorithm designed to fit the specific needs to detect RBCs in our experiments.

As a first step in reliably detecting RBCs, we subtract the background of the image sequence. Since the images capture a static channel, i.e. static pixel information, and dynamically changing pixels when cells are flowing through the field of view, this background  $B_{ij}$  is estimated by the arithmetic mean of a subset of  $N$  images  $I_{nij}$ :

$$B_{ij} = \frac{1}{N} \sum_{n=1}^N I_{nij}, \quad (2.5)$$

with the pixel coordinates  $i, j$ . A value of  $N = 100$  has been proven to be sufficient, such that only small fluctuations are reminiscent in the resulting image after the background has been subtracted iteratively from individual images. This  $n$ -th resulting image  $R_{nij}$  is then given by

$$R_{nij} = |B_{ij} - I_{nij}|, \quad (2.6)$$

where the absolute value has been calculated since all deviations from the background are of interest. To smooth the resulting images, a median filter with a stride of  $3 \times 3$  pixels is then applied subsequently, removing artifacts and leaving a despeckled image. After the conversion of the gray-value image to a binarized image, we obtain of all white pixel clouds their respective centers of mass, which is equivalent to the center of mass of the RBCs. Since the binarized images of flowing RBCs may contain neighboring black pixels within the white cell cores, we fill these holes in the input binary images. An example of this overall process with the single steps is sketched in Fig. 2.5.

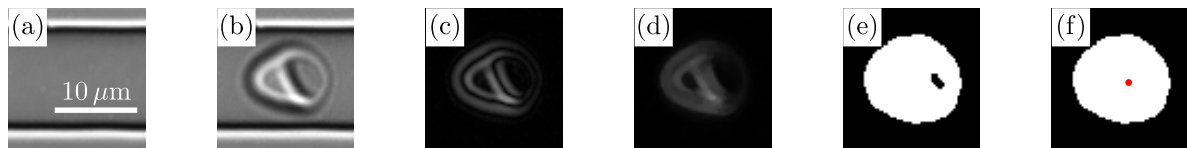


**Figure 2.5:** Scheme of image post-processing steps for RBCs in microcapillary flow. For better visualization, the widths of the individual images have been cropped to fit one RBC. (a) Background of the cropped channel, obtained by the arithmetic mean of 100 images of one image sequence, cf. Eq. (2.5). (b) Raw image of a flowing RBC captured at the identical channel position as in (a). (c) Resulting image after subtracting the background image (a) from (b), according to Eq. (2.6). (d) Image after application of a median filter. (e) Binarized image, obtained from gray-value image (d). (f) Filling the connected black pixels in (e), we omit any holes in the final cell image. The red dot indicates the position of the center of mass.

Additionally to the centers of mass, we obtain further shape descriptors such as the area, the orientation, and the eccentricity of an ellipsoid exhibiting identical second moments. Due to the installed optical components and the resulting resolution, we conjecture a general uncertainty in the detection of the center of mass of  $s_p = \pm 0.1 \mu\text{m}$ .

To obtain trajectories from these RBC positions, we minimize the distances of these positions in adjacent image pairs. This linking protocol is applied to the entire image sequence yielding the trajectories of all recorded cells.

We further apply a filter to the obtained trajectories, omitting all trajectories of RBCs that cannot be regarded as isolated cells since the intercellular distance, i.e. the distance to the preceding or succeeding cell is too close, such that hydrodynamic interactions are no longer negligible. Images of RBCs fulfilling the isolated cell property are cropped within a section of  $90 \text{ px} \times 90 \text{ px}$ , an image size large enough to cover the entire channel width including the channel borders. A sophisticated algorithm ensures that the whole cell is captured within this section, independent of the exact position of the center of mass.



## Chapter 3

# Shape phase diagram of flowing RBCs in microchannels

In this chapter, we present results from a joint numerical and experimental study, performed in close collaboration with the *Biofluid Simulation and Modeling* group at Bayreuth University, who carried out all numerical simulations shown in the subsequent sections. The addressed research goal was the establishment of profound knowledge of single RBC behavior under laminar flow conditions in microcapillaries. The results presented in this chapter have been subject to prior publication [147].

### 3.1 Introduction

The mechanistic behavior of red blood cells as the major cellular constituent governs the overall blood flow to a large extent. As a key to fully understand the flow dynamics and to reliably predict blood flow in arbitrary confinements, e.g. in realistic *in vivo* networks, we seek to analyze the dynamics of single RBCs traveling in a straight rectangular duct. Albeit the simplicity of this setup, we present a rich shape phase diagram consisting of two distinct shape categories, the axisymmetric croissants, and the asymmetric slippers. Based on our experimental setup, an *in silico* approach has been tailored to mimic the employed channel geometries *in vitro*. Both approaches show a very good agreement between the phase diagrams and the radial distribution of RBCs in the channel.

These phenomena form the cornerstone for the development of cell sorting techniques, specifically for those being based on individual cell deformability, such as deterministic lateral displacement devices [148]. Other possible applications involve diagnostics tools integrated on lab-on-a-chip devices as a subtle tool to detect pathological conditions affecting the cell deformability. In addition to current techniques that mainly deal with RBCs in stasis, a wide parameter space can be explored using dynamic techniques.

One of the very first conducted experiments on dilute driven blood suspensions *in vitro* has been performed by Gaegtgens *et al.* [24], describing distinct shape categories consisting of axisymmetric and asymmetric shapes. A comparative study of *in vitro* and *in silico* experiments was performed by Secomb *et al.* [47]. They used a cylindrical tube with a diameter identical to the equilibrium diameter of the RBC discocyte, i.e., 8  $\mu\text{m}$ . Tomaiuolo *et al.* [57] employed slightly larger channel diameters of 10  $\mu\text{m}$ , observing both croissants as well as slippers for various velocities.

Most studies addressing blood flow in narrow capillaries focus on rather dense suspensions and associated phenomena, such as e.g. collision dynamics and intercellular interactions [17,

22, 24, 30, 78, 149]. Often, the assumed typical diameters of the channels are larger with respect to our microfluidic setup [34, 150].

Among those studies addressing the isolated RBC behavior there are mostly numerical investigations with RBC models that do not capture the entire complexity of the real underlying structure. Simplifications consist e.g. of the use of 2D vesicles as RBC models.

## 3.2 Experimental setup

Following the preparation and handling protocols outlined in section 2.1, we obtain a suspension of RBCs in a phosphate buffer and bovine serum albumin solution. The hematocrit of this solution has been adjusted to  $\lesssim 1.0\%$  to maintain on the one hand a solution dense enough in RBCs such that the recorded image series contain sufficient cells. On the other hand, we seek to record individual RBCs rather than (hydrodynamic) clusters with an insufficient intercellular distance. Nevertheless, we find single RBCs as well as agglomerates of cells advecting through the channel. The former have been further processed to extract velocity data and cropped images capturing only the cell shape, whereas the latter have been omitted for our study. In accordance with both experimental and theoretical observations stating that the hydrodynamic interactions can be neglected for intercellular distances twice the channel width [27, 151], we set an intercellular distance of  $40\ \mu\text{m}$  as the threshold to define isolated cells.

## 3.3 Modeling the RBC dynamics in silico

*This study has been designed as a comparative study of experimental and numerical research goals. The following modeling of the RBC flow in microcapillaries has been entirely designed and carried out by Achim Guckenberger and Stephan Gekle from the Biofluid Modeling and Simulation group at Bayreuth University.*

The setup for the numerical simulations is based on the given experimental restrictions and setup. A single RBC is modeled in a straight channel with a rectangular cross-section, obeying a width  $l_y = 12\ \mu\text{m}$  and a height of  $l_z = 10\ \mu\text{m}$ . The length of the channel segment is set as  $l_x = 42.7\ \mu\text{m}$ , with employed periodic boundary conditions. The channel walls themselves are undeformable, with hardcore interactions being present between them and the RBC body.

Both the internal as well as the surrounding fluid of the RBC are modeled as Newtonian fluids. Based on physiological values, the dynamic viscosity of the surrounding phase equals the viscosity of plasma,  $\mu_{\text{ext}} = 1.2\ \text{mPa}\cdot\text{s}$ . The internal viscosity of RBCs is subject to variations spanning multiple orders of magnitude under physiological conditions and increases over the lifetime of each RBC [83]. Yet, an average viscosity contrast  $\lambda_{\text{visc}} = \mu_{\text{RBC}}/\mu_{\text{ext}} = 5$  of inner and outer fluid is assumed as a realistic average value and hence maintained throughout the performed simulations if not explicitly stated otherwise [83, 147].

The modeled RBC exhibits a surface with an area of  $140\ \mu\text{m}^2$ , enclosing a volume of  $100\ \mu\text{m}^3$ , in accordance to the measured quantities of RBCs ex vivo, as described in section 1.1.1. The RBC membrane is further modeled as an infinitely thin layer, whose bending resistance is set to  $\kappa_B = 3 \times 10^{-19}\ \text{J}$ . Additionally, the area dilatation modulus  $\kappa_A$  is set to  $\kappa_A = 100\kappa_S$ ,

effectively limiting the total relative area change below 2%.  $\kappa_S = 5 \times 10^{-6} \text{ N m}^{-1}$  denotes the shear elasticity of the membrane. Further implementation details are not provided in this section; however, they are available in references [147, 152].

In the experimental approach, we are limited in influencing the initial RBC shape upon entry of the microchannel. Additionally, the radial position when entering the channel remains an uncontrollable parameter in the current experimental setup. In the numerical simulations, however, these two parameters can be assessed and varied according to the underlying physical restrictions, namely:

- (i) Variation of the initial cellular configuration, and
- (ii) Variation of the initial radial position.

In the first case, we vary the initial shape between discocyte, croissant, and slipper shapes. The radial offset in the latter case is given as the Euclidean distance of the center of mass with respect to the centerline as a reference point,  $r_{\text{init}} = \sqrt{y_{\text{init}}^2 + z_{\text{init}}^2}$ .  $r_{\text{init}}$  is further varied along a line parameterized as  $z_{\text{init}} = 5y_{\text{init}}/9$ , in very good approximation to the diagonal axis, as depicted in Fig. 3.1.

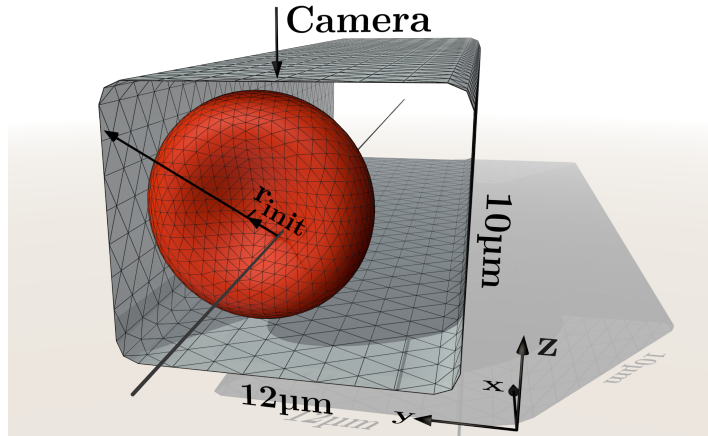


**Figure 3.1:** Starting configuration in the numerical model. A discocyte initial shape is placed in a rectangular duct, with the symmetry axis of the RBC being aligned with the channel centerline. The initial offset  $r_{\text{init}}$  can be varied along a parameterized line (see main text for further specifications). Image adapted from reference [147].

In the case of the discocyte initial shape, whose symmetry axis is aligned with the channel axis, we thus obtain a maximal initial offset of  $r_{\text{init}}^{\text{max}} \simeq 2.06 \mu\text{m}$ .

### 3.4 Experimental results

Among the final recorded cell images, we discriminate three hydrodynamically induced shape classes by manual evaluation: The “croissant” and the “slipper” shapes as well as a class we refer to as “others”, containing all cell shapes that do not fit into either of the previous categories. The croissant shape characterizes an axisymmetric RBC shape with respect to the flow direction, contrasting the asymmetric slipper shape, describing off-centered RBCs with respect to the channel centerline. The latter can be found in two configurations, originating

from one another through mirroring on the channel axis.

Although the others are defined as outliers with respect to the distinct shape classes croissants and slippers, subclasses within these others can be observed, depending on the prevailing flow conditions. A collection of others prevalent in different flow conditions, alongside croissant shapes and slippers, obtained both from experiments and simulations, is shown in Fig. 3.2. Typically, discocytes displaying a tumbling motion are observed regularly at low flow veloc-

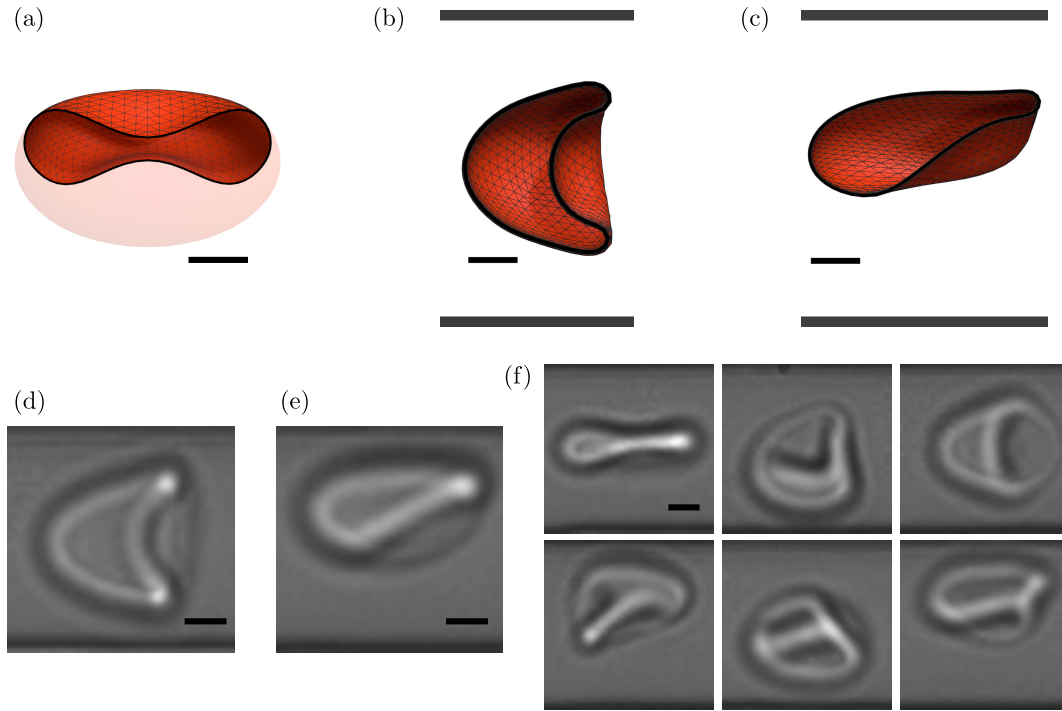


**Figure 3.2:** Comparison of cell shapes obtained in vitro and in silico. (a) In silico discocyte shape, with a visible mesh and a diameter of  $8\ \mu\text{m}$ . For the sake of visibility, the front half has been made translucent. (b) Typical croissant shape obtained in the numerical simulations, which has been employed also as an initial shape in some simulations. The cell velocity is around  $1.1\ \text{mm s}^{-1}$  and the cross-section of the middle plane has been marked by a solid black line. (c) Similarly, a slipper shape from simulations is obtained at a cell velocity of ca.  $5.2\ \text{mm s}^{-1}$ . As in the previous case, the circumference of the center cut is highlighted by the solid black line. The black horizontal lines on the top and bottom, resp., of (b,c) indicate the channel borders. (d) A typical croissant shape obtained in vitro at a cell velocity of  $1.0\ \text{mm s}^{-1}$ . (e) Representative slipper shape for a cell velocity of  $6.2\ \text{mm s}^{-1}$ . (f) A collection of various cell shapes classified as others. Starting anti-clockwise in the upper left corner, a tumbling discocyte in side view is depicted, with a cell velocity of approx.  $0.4\ \text{mm s}^{-1}$ . Subsequently, the cell velocities increase, with the individual cells flowing at  $2.1\ \text{mm s}^{-1}$ ,  $4.3\ \text{mm s}^{-1}$ ,  $6.3\ \text{mm s}^{-1}$ ,  $8.2\ \text{mm s}^{-1}$  and  $9.9\ \text{mm s}^{-1}$ , respectively. Multilobated cells are seen to undergo either a tumbling motion or a membrane movement resembling tank-treading behavior. For each cell image depicting a hydrodynamically induced shape, the flow is coming from the right. All scale bars correspond to a length of  $2\ \mu\text{m}$ . Image adapted from reference [147].

ities  $u_{\text{RBC}} \lesssim 0.5\ \text{mm s}^{-1}$ . As the flow strength increases, the hydrodynamic forces become more pronounced, inducing shape changes from the equilibrium discocyte shape to deformed shapes. Others then consist mainly of multilobated cell shapes, similar to the ones found in shear flow by Lanotte *et al.* [150]. They performed additional experiments in Poiseuille flow

with adapted wall shear rates and confirmed the existence of the formerly obtained shapes. In an intermediate flow regime, they observed the tumbling discocytes population to vanish, and the most pronounced cell shape resembles a folded stomatocyte, which can be associated with tilted slippers in top view, as depicted in one of the cell images in Fig. 3.2 (f).

Besides multilobated cells, formed wrinkles are regularly observed for others in a velocity regime, where slippers are the most populous cell category. Although the position of these wrinkles is non-stationary with respect to the cell, a tank-treading movement (cf. section 1.2.1) cannot be confirmed in the current experimental setup. Apart from these previously described subcategories of cell shapes, additional, highly irregular cell shapes are observed. In general, the multitude of different shapes renders a more refined approach virtually impractical and therefore, others do not comprise a well-defined cell shape but are rather defined as shape outliers not fitting into the croissants or the slippers category.

We stress that in most scientific literature, the nomenclature is preallocated for the symmetric cell shapes by the term parachutes. However, since a perfectly rotationally symmetric shape (parachute) can only emerge in cylindrical ducts [21], we distinguish croissant shapes prevailing in the employed rectangular duct from these parachutes.

For a systematic investigation, we apply a pressure drop on the microchannels containing the final blood solution (cf. section 2.1), ranging from 20 mbar – 1,000 mbar in discretized steps. These pressure drops translate linearly into mean cell velocities  $u_{\text{RBC}}$ , ranging from  $0.14 \text{ mm s}^{-1}$  –  $10.6 \text{ mm s}^{-1}$ , and thus cover the entire range of RBC velocities found in humans (cf. table 1.1).

Yet, due to different axial positions within the channel and resulting velocity differences according to the imprinted Poiseuille flow profile, the individual mean velocities of slippers, croissants, and others slightly differ. In Fig. 3.3 the mean velocities and corresponding standard deviations  $\sigma_u$  are depicted.

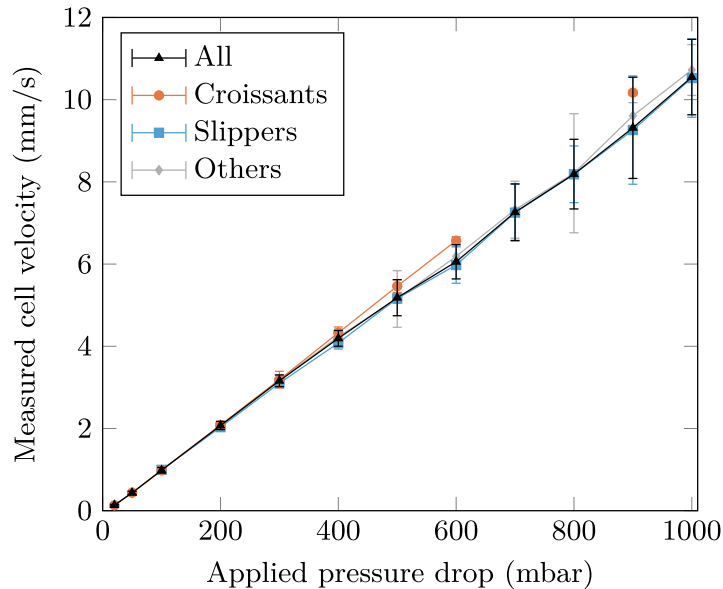


**Figure 3.3:** Obtained cell velocity for the applied pressure drop in the microfluidic channel with a cross-section of  $12 \mu\text{m} \times 10 \mu\text{m}$  for all cell shape categories. The error bars indicate the standard deviation from the mean speed (denoted by symbols). Image adapted from reference [147].

The error bars for the given mean velocities in Fig. 3.3 correspond to the calculated standard deviations.

In the following sections, we restrict our findings to the channel cross-section of approx.  $12\ \mu\text{m} \times 10\ \mu\text{m}$ , since the experiments performed with divergent cross-sections show a less rich phase diagram. Only the discussed geometry obeys significant slipper and croissant populations due to the specific dimensions and the resulting aspect ratio.

Further, the cell images are recorded at two distinct positions: the channel entrance  $x = 0\ \text{mm}$ , i.e. the transition from inlet reservoir and channel, and the position  $x = 10\ \text{mm}$  further downstream, respectively. The first position reveals the initial distribution of RBCs upon entering the confined geometry. At the latter position, on the other hand, transient shapes converged to the steady-state shape, as was also confirmed by Clavería *et al.* [30], observing only minor quantitative changes in the cell shapes recorded at  $x = 2\ \text{mm}$  and  $x = 10\ \text{mm}$ .

### 3.4.1 Shape phase diagram of flowing RBCs

By manual classification of the individual cell shapes at a certain applied pressure drop, we compute the fraction of croissants and slippers in each image set. In Fig. 3.4, these fractions are shown, constituting the shape phase diagram.

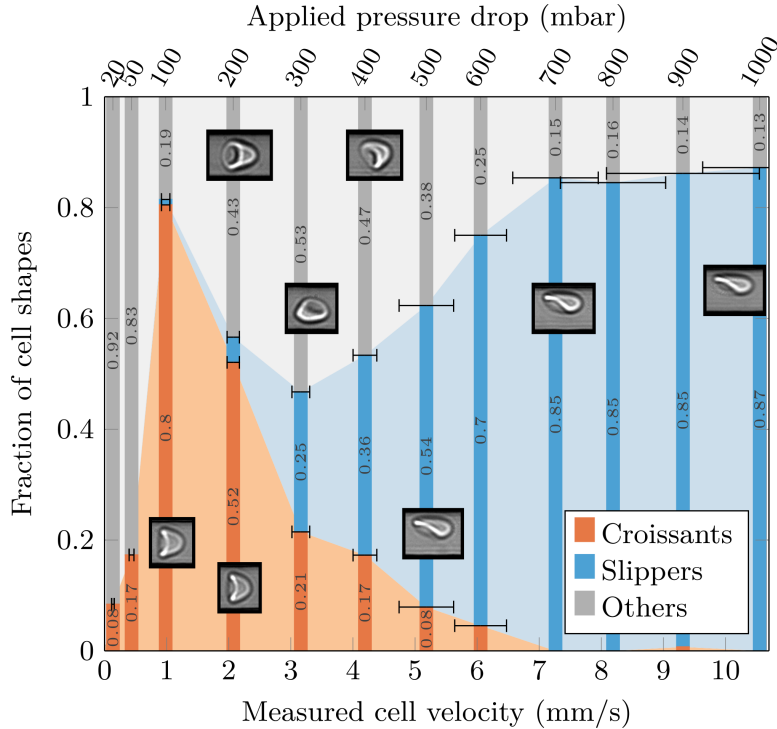


**Figure 3.4:** Shape phase diagram of the underlying microfluidic channel geometry. Horizontal error bars indicate the standard deviation  $\sigma_u$  of the mean cell velocity. Individual data points of each respective population are connected via straight lines as a guide for the eye. As such, the colored areas represent the fractions of croissants (reddish area), and slippers (blue area), respectively. The insets represent typical cell images for the three distinct categories. Image adapted from reference [147].

For each pressure drop, at least 100 cells have been classified, with a total number of 3090

RBCs. The error bars in the diagram specify the velocity error, given as the standard deviation  $\sigma_u$  of the velocity. At very low velocities the RBC shape is associated with tumbling discocytes, which are then classified as others according to our scheme. A peak of the croissant population is found for velocities  $1 \text{ mm s}^{-1} \lesssim u_{\text{RBC}} \lesssim 2 \text{ mm s}^{-1}$ . With increasing RBC velocity, the croissant fraction decreases, towards an increased slipper population, which is the most pronounced shape for the highest velocities, as can be seen in Fig. 3.4.

### 3.4.2 Axial distribution of RBCs in the microchannel

From the particle tracking results, we have detailed knowledge of the  $y$ -positions, i.e. the distributions of RBCs across the channel width are known (cf. section 2.4.2). To quantify the lateral position of the cells, given as the  $z$ -projection of the RBC, we employ the probability density distribution pdf( $y$ ) of the discrete position data for every imposed pressure drop. The best estimate of the pdf is given by a kernel density estimator using the optimal bin width. In particular, a gaussian kernel with a fixed support of  $[-6, 6] \mu\text{m}$ , according to the channel width, was used.

In Fig. 3.5, the probability densities are depicted at two distinct positions: In Fig. 3.5 (a), the initial RBC distribution at the channel entrance, i.e. at a position  $x = 0 \text{ mm}$ , is depicted. In contrast, Fig. 3.5 (b) shows the distribution at a position  $x = 10 \text{ mm}$  further downstream, where the cell shape evolution is supposed to have reached a steady state. In both cases, we

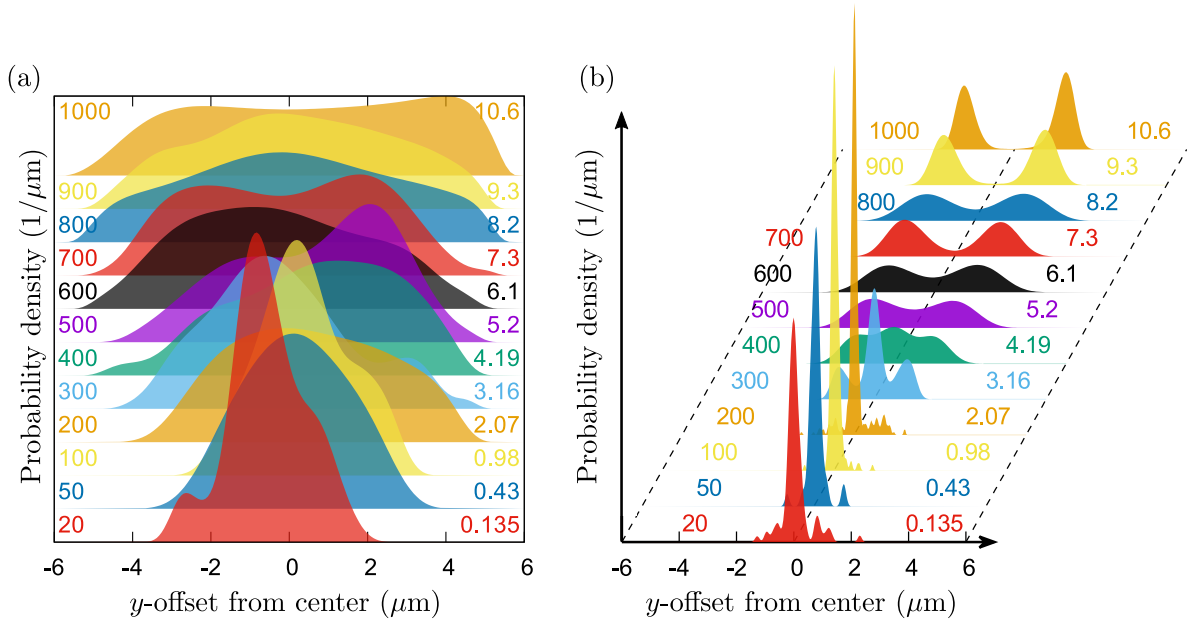


**Figure 3.5:** Radial distribution of RBCs along the channel width for two distinct positions: In (a), the estimated probability density of all RBCs at the entrance position of the channel, i.e., for  $x = 0 \text{ mm}$ , is depicted. Similarly, the estimated probability densities of the  $y$ -offset at a position  $x = 10 \text{ mm}$  further downstream is depicted in (b). In both subfigures, numbers adjusted to the left of the individual graphs indicate the applied pressure drop in matching colors in mbar. Numbers to the right of the graphs indicate the corresponding mean speed in mm/s. Graphs are subject to a vertical offset to enhance visibility. Image adapted from reference [147].

analyze the pooled distributions, i.e., independent of the individual cell shape for each applied pressure drop. In Fig. 3.5 (a), the  $y$ -offset from the center shows an initially centralized peak for low pressure drops, which subsequently broadens as the pressure drop increases. Further downstream, the RBC distributions also obey a pronounced central peak for low pressure drops  $\Delta p \lesssim 200$  mbar, as shown in Fig. 3.5 (b). As the RBC velocities increase, this central peak minimizes and the distribution broadens towards the channel walls. Finally, for pressure drops  $\Delta p \gtrsim 500$  mbar, a bimodal distribution is adopted.

Qualitatively, the origin of the distribution characteristics can be understood by considering the individual shape categories. As depicted in Fig. 3.6, the probability densities for each distinct shape category at a position of  $x = 10$  mm downstream of the channel entrance differ. Croissants obey a central peak around the channel center indicating a narrow distribution, while others mostly occur in the channel center for low pressure drops  $\Delta p \lesssim 200$  mbar. The

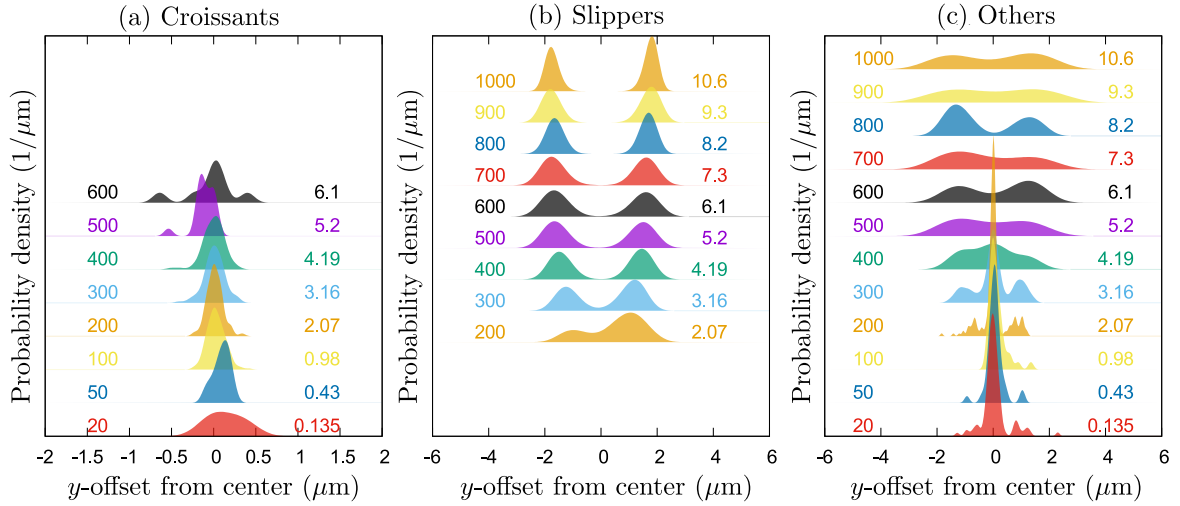


**Figure 3.6:** Radial distribution of RBCs along the channel width at a position  $x = 10$  mm downstream. (a) Distribution of cells classified as croissants. For pressure drops  $\Delta p \geq 600$  mbar, no croissants are detected. (b) Radial distribution of slipper shapes within the microfluidic constriction. Similar to the case in (a), no slipper shapes occur for  $\Delta p \leq 200$  mbar. (c) Distribution of all shapes categorized as others. In each panel, numbers adjusted to the left of the graphs indicate the applied pressure drop in matching colors. To the right of the graphs, the mean speed is denoted. Graphs are subject to a vertical offset to enhance visibility. Image adapted from reference [147].

distribution of others is consequently broadening for increasing pressure drops. In contrast, the slipper distribution shows a bimodal behavior, indicating the off-centered position of the detected cells. With increasing pressure drops both peaks are more pronounced and tend to migrate towards the channel walls. The joint estimates for all RBCs is presented in Fig. 3.5 (b). From the results one might deduct that velocity is the key parameter in determining the final shape of the RBC. However, a comparison of the RBC centroid positions at the entrance position, i.e., at  $x = 0$  mm, obeys an inhomogeneous distribution, as illustrated in Fig. 3.5 (a). For low pressure drops, the distribution is biased towards a centralized peak at the channel centerline. As the pressure drops increase, the distributions are successively broadening. These observations give rise to the initial distribution as a second important parameter, besides the RBC velocity, influencing the final shape. Our employed experimental setup limits the

possibility to affect the initial distribution, however, we stress that in principle the initial distribution can be altered, e.g. by the use of sophisticated optical tweezer setups.

### 3.5 Numerical results

According to the experimental setup, we investigate the properties and the behavior of single RBCs while flowing through rectangular channels. The flow velocity, as well as the radial offset  $r_{\text{init}}$  from the channel centerline, are varied to study their influence on the final RBC shape. However, this final shape is either obtained in the steady-state, i.e., after a sufficient elapsed time interval where the cell shape and the radial position remain constant. Alternatively, we find a periodic oscillation of the center of mass induced by oscillating contractions of the cellular shape, similar to previous findings in the case of slippers [55].

An exemplary temporal evolution from an initial discocyte towards a stable croissant shape is depicted in Fig. 3.7. As an intermediate state, a slipper is formed, yielding the previously described oscillatory motion of the centroid position due to the periodic contractions of the cell. This slipper then develops into a croissant state, located at the channel center. Yet, the croissant shape is not fully converged, as indicated by the peak, caused by minuscule membrane deformations. A final, i.e., fully converged croissant shape is obtained in this case after an elapsed time of ca. 14 s. In most cases, the cell shapes converge to either croissant

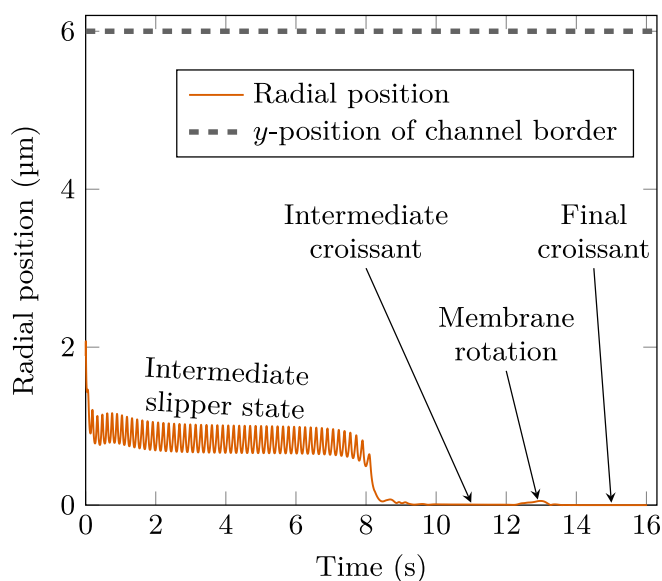


**Figure 3.7:** Temporal evolution of an initialized discocyte, whose symmetry axis is aligned with the channel centerline. Soon an intermediate slipper state is formed, leading to oscillatory shifts of the centroid position. At approx. 9 s, an intermediate croissant shape exists, which is characterized by the minor membrane deformations leading to a shift in the radial position. Finally, a stable croissant is formed, marking the steady state. An initial radial offset of approx.  $1.9 \mu\text{m}$  and a velocity of approx.  $2.8 \text{ mm s}^{-1}$  have been chosen to provoke this scenario. Image adapted from reference [147].

or slipper shapes in the steady-state. The former can be subdivided into two categories: The tank-treading (TT) and the non-tank-treading (non-TT) croissants. Taking into account the symmetry of the croissant shapes, the tank-treading behavior can only arise in the case of

asymmetrically formed croissants, which only emerge at high velocities, as will be discussed in the following sections.

Throughout the analysis, we perform a simulation for one set of parameters with one cell, and thus, the mean radial positions are given by a temporal average of the cell positions in the steady-state, with the extremal values indicating the error bars. Starting with an intermediate to high velocity of approx.  $6.5 \text{ mm s}^{-1}$  we observe a pronounced bistability of the final shape, as depicted in Fig. 3.8. In other words, we find a sharp transition line between the croissant and

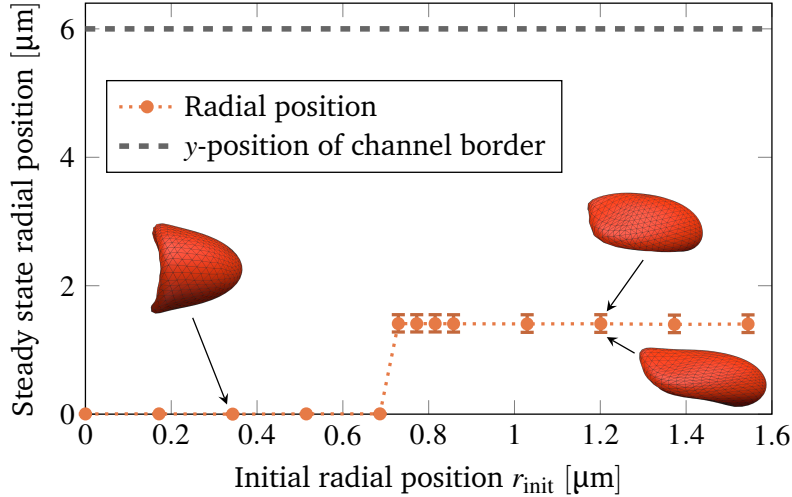


**Figure 3.8:** Scheme of the pronounced bistability found in the simulations. RBCs initialized as discocytes. At  $\approx 6.5 \text{ mm s}^{-1}$ , a sharp transition between croissant and slipper shape is observed, in conjunction with a sudden shift of the steady state radial position. Vertical error bars correspond to the minimal and maximal centroid positions, originating from periodic contractions of the slipper shapes (inset images show the respective shapes). Image adapted from reference [147].

the slipper shape as the initial radial offset approaches  $r_{\text{init}} \simeq 0.7 \mu\text{m}$ . Below this transition value, RBCs initialized as discocytes develop a croissant shape in the steady-state, contrary to slippers that develop for cells with an initial offset above this critical value. Interestingly, the slippers are mostly off-centered along the channel width, i.e. they are oriented as the slippers obtained in vitro. Along the channel height, only minor off-sets are seen.

Generally, the observation of bistability indicates the importance of the initial radial offset as a crucial parameter and we conjecture that the same holds for the initial shape, since the maximal radial offsets are determined also by the adapted shape. Hence, for a systematic investigation, we vary the velocity of the advecting cells gradually as in the experiment. Additionally, we impose three different initial shapes and screen a set of initial radial offsets. The resulting phase diagrams, where the previously described parameter spaces are exploited are presented in the following section.

### 3.5.1 Shape phase diagram of flowing RBCs

Similar to the experimental findings we seek to investigate the shapes of the RBCs in the final state. In contrast to the experimental approach, the in silico approach allows for manipulating the initial shape configuration. We therefore employ three initial configurations, as discocyte, croissant, or slipper, respectively. The discocyte is obtained directly from the standard initial

modeling according to the formula in Eq. (1.1). The two latter shapes are initialized by previous simulations yielding the respective final state.

The resulting three phase diagrams are presented in Fig. 3.9. We stress that these phase diagrams conceptually differ from the experimental phase diagram presented in section 3.4.1 due to the intricate parameter space. Therefore, the final states are not only presented as categorial fractions in dependence of their centroid velocity but rather the steady-state shapes of simulated RBCs are depicted for different cell velocities and varying initial radial offsets (cf. section 3.3 for detailed information).

In addition to the imposed cell velocities, we provide the bending capillary number  $Ca_B := \mu u_{RBC} R_{RBC}^2 / \kappa_B$  as a dimensionless measure of the relative flow strength in comparison to the intrinsic bending forces in Poiseuille flow profiles. This capillary number is often referred to in the context of the coupling of fluids and deformable objects in different geometries.

All three phase diagrams in Fig. 3.9 share a pronounced peak from  $2 \text{ mm s}^{-1} \lesssim u_{RBC} \lesssim 3 \text{ mm s}^{-1}$ , where only croissants emerge in the steady-state. Slippers, on the other hand, show

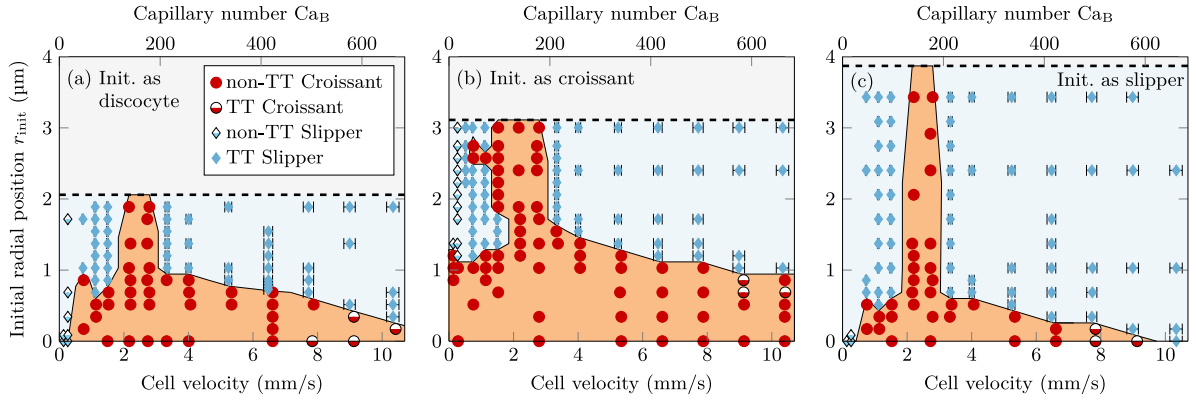


**Figure 3.9:** Cell shapes obtained in silico for varying offsets  $r_{\text{init}}$  and RBC velocities. In (a), cells are initialized as the typical discocyte, whereas in (b), croissant shapes, obtained by previous simulations, are employed as initial cell shapes. Similarly, slipper shapes formed the initial RBC shape in (c). In each subfigure, the dashed line corresponds to the maximal initial offset  $r_{\text{init}}^{\text{max}}$ . Each symbol in the subfigures indicates one distinct simulation, with the mean cell velocity in the steady-state by the abscissa value and horizontal error bars corresponding to the obtained extremal velocity values (invisible if the error margins are within the symbol size, e.g. for low velocities). The color shaded areas indicate the distinct shape phases of croissants (reddish area), and slippers (blue area). They are separated by a sharp transition line, drawn as a solid black intersection line. Image adapted from reference [147].

tank-treading behavior with the only exception at very low velocities  $u_{RBC} < 0.5 \text{ mm s}^{-1}$ , where non-TT slippers occur independently of the initial shapes. These non-TT slippers instead show a tumbling motion when advecting through the channel, i.e., the cellular shape is maintained while occasionally rotating around the  $z$ -axis. This tumbling movement has been observed previously in cylindrical channels by Fedosov *et al.* [55]; however, a change of the cellular shape was in effect [55]. Furthermore, the tumbling motion of the cells is also observed for very low velocities in the experimental approach, yet with cell shapes classified as others.

Similarly, we find atypical croissant shapes for high velocities  $\gtrsim 7 \text{ mm s}^{-1}$ , which obey a tank-treading movement. Henceforth, we will refer to these shapes as TT-croissants.

A comparison of the relative areas associated with croissants and slippers, respectively, reveals

the fact that croissants are favored in the final state when initialized as such. On the other hand, the final slipper state is privileged when slippers are initialized.

### 3.5.2 Axial distribution of RBCs in the microchannel

Besides the final shape, we are also interested in the final centroid position of the converged cell shapes. Of each converged simulated cell shape, the positions are then computed via a temporal average. This procedure then yields the mean cell positions by a simple arithmetic average of the individual cell positions. The resulting graphs of these final radial positions are given in Fig. 3.10 (a) for the three initial cell shape categories separately. A main finding is the

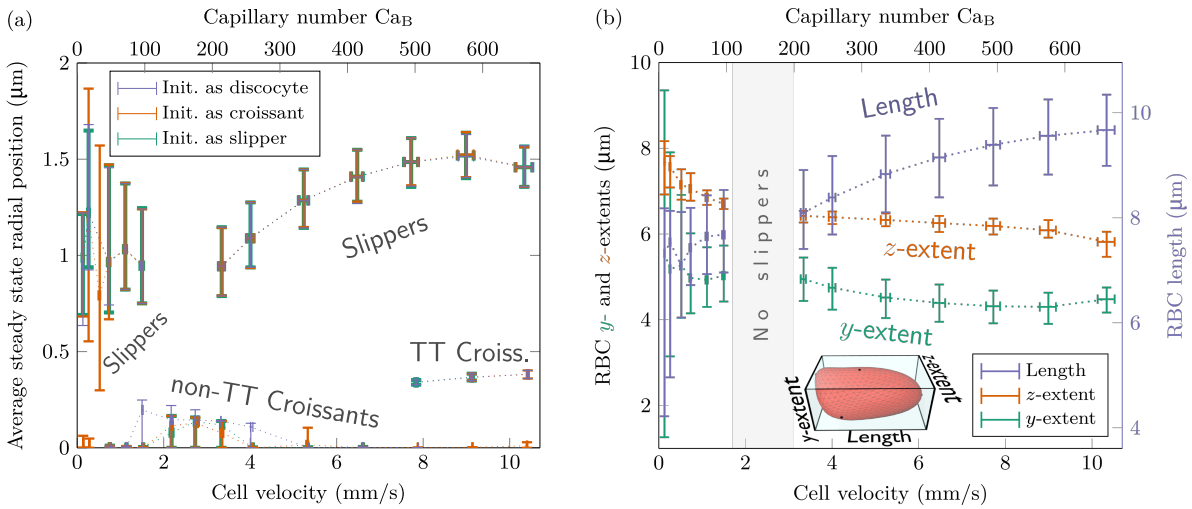


**Figure 3.10:** Simulation results of average steady state radial positions of RBC centroids (a) and cell extents (b). The individual initial shapes are plotted separately to observe the influence of this initial configuration on the final position. Horizontal error bars indicate the velocity margins of the simulation ensemble. Vertical error bars, on the other hand, indicate the minimal and maximal values. Image adapted from reference [147].

presumably logical fact that the final centroid position is independent of the initial cell shape. Consequently, the position of each individual cell shape in the final state is solely determined by the imposed flow velocity. As a consequence, the individual data points corresponding to the final slipper shapes overlap for the distinct initial configurations.

Non-TT croissants further appear in very close proximity to the channel centerline, with only minor deviations. These deviations mostly arise due to minor oscillations of the surrounding membrane. TT-croissants, on the other hand, appear only at high velocities  $\gtrsim 8 \text{ mm s}^{-1}$  at an off-centered position of approx.  $0.4 \mu\text{m}$ . Even though they are still classified as croissants, the tank-treading can only occur in non-symmetrical shapes, however, their slight asymmetry resembles the typical croissant shape.

A closer inspection of the final slipper shapes is presented in Fig. 3.10 (b), where we focus on the extents of the slippers. These extents are defined as the measured edge lengths of an associated bounding box containing the respective slipper shape. Interestingly, the  $y$ -extent and the  $z$ -extent show only minor changes with increasing velocity, in contrast to the slipper length ( $x$ -extent), which is increasing as the velocity increases.

## 3.6 Discussion of in vitro and in silico results

An accurate definition of the cell categories and the corresponding thresholds has proven to be a major problem. This fact explicitly holds for the case of croissants, which are defined as axially symmetric. In the simulation, detailed 3D information of the membranous sack is accessible, contrary to the experimental data, only providing projections of the cellular body in the  $z$ -plane.

Apart from the conceptual difference of these imaging techniques, we note that in the case of experimental images the true cell borders are blurred out due to diffraction occurring at the boundaries.

Additionally, the field of view is limited in the experimental setup, thus collision events of adjacent cells remain ambiguous. Such collisions may directly alter the shape and position of cells but also lead to transient cell shapes further on. To overcome this drawback, we analyzed the image sequences twice in order to minimize the subjective input. Nevertheless, a coherent distinction between the cell shapes is highly non-trivial and we therefore seek to find an optimized, objective classification tool, as presented in chapter 4.

### 3.6.1 Comparison of shape phase diagrams

Qualitatively, the experimentally obtained and the numerically obtained phase diagrams lead to identical implications: For very low velocities, the RBC shapes observed in the experiment merely consist of other shapes, which is mirrored in the simulation data, favoring non-TT slippers. An exception, however, is given for the cells initialized as croissants, which obviously favor croissants also at low velocities. We thus conjecture that these shapes are highly unlikely in the experimental distribution of cell shapes.

A second resemblance between these two phase diagrams is present at low velocities  $2 \text{ mm s}^{-1} \lesssim u_{\text{RBC}} \lesssim 3 \text{ mm s}^{-1}$ , where in the simulations a croissant-only peak occurs. Analogously, we observe a large proportion of croissant shapes, including the global peak of the croissant fraction in the experiment. Furthermore, the population of croissants decreases in favor of slippers as the velocity further increases.

For a direct quantitative comparison of the two methodologies, we need to translate the phase diagram of the numerical approach, relating the final state shape to the imposed cell velocity and the initial radial offset, to the experimental phase diagram, relating a true cell shape fraction on the cell velocity with unknown initial cell shape configuration, yet with known radial distribution at the channel entrance  $x = 0 \text{ mm}$ .

Therefore, we perform a convolution of the experimental distribution of cells at the initial position, as depicted in Fig. 3.5 (a) and the numerical phase diagram provided in Fig. 3.9 for all the distinct initial cell shapes (a)-(c).

Since the outcome of this method is highly affected by the choice of the transition line of slippers and croissants in the numerical phase diagram (cf. Fig. 3.9), we will discuss first the essential estimation of the transition line based on the underlying finite simulation dataset. We restrict the necessary steps that precede the estimation of this transition line to the case of an initialized discocyte shape and note that the performed steps can be generalized to obtain the transition lines of the remaining cases.

Starting with the discrete set of performed simulations yields the numerical phase diagram as depicted in Fig. 3.9 (a); however, with the data points only. Connecting each of the largest values of  $r_{\text{init}}$  which still yields croissants (red circles), and the lowest  $r_{\text{init}}$  yielding slippers

(blue diamonds), respectively, results in two lines, indicating the general uncertainty owed to the discretization pattern of the simulation parameters, such as velocity and initial offset. In Fig. 3.11, these two lines are represented by the violet line in the former case and the green line in the latter case. The line in between these upper and lower bounds, shown as a grey

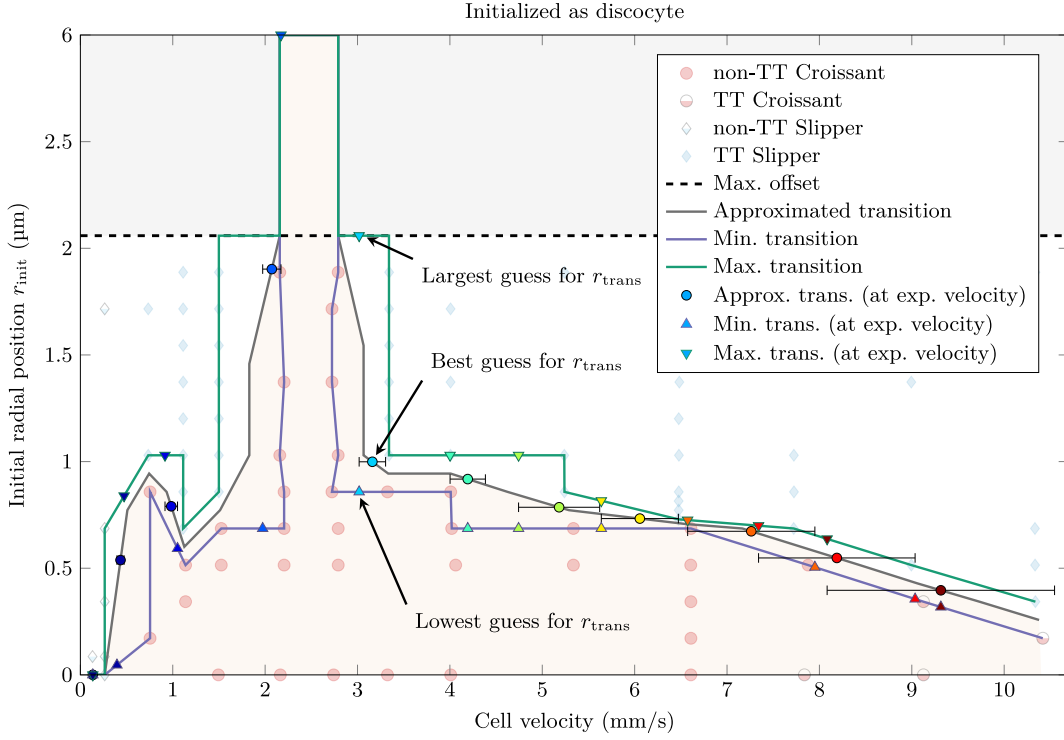


**Figure 3.11:** Scheme to determine the transition line between croissants and slippers and the corresponding uncertainties in the prediction. The underlying data points (shaded symbols) correspond to the ones in Fig. 3.9 (a), i.e., they are obtained with a discocyte as starting shape. The violet solid line indicates the minimum position according to the numerical data, for the transition value  $r_{\text{trans}}$ . Analogously, the grey and the green solid lines represent the average and the maximum value, respectively, for the transition threshold between the distinct shape categories of croissants and slippers. The non-shaded data points correspond to the mean experimental velocities  $u_{\text{RBC}}$  (circles), and the associated errors  $u_{\text{RBC}} + \sigma_u$ . Image adapted from reference [147].

line in the scheme, is obtained via the arithmetic mean of corresponding parameters from adjacent simulation symbols. This line then represents the estimated transition line  $r_{\text{trans}}$  of slippers and croissants.

In a further step, we evaluate the ordinate values on this line belonging to the measured experimental mean cell velocities  $u_{\text{RBC}}$ , resulting in the best guess for the transition value  $r_{\text{trans}}$ , denoted by the circular symbols in Fig. 3.11. Accordingly, the values of  $r_{\text{trans}}$  are evaluated for the lower and upper transition lines as an error estimation of  $r_{\text{trans}}$  at the measured mean cell velocity  $u_{\text{RBC}}$ .

Bearing in mind that the velocity of the RBCs exhibits a certain standard deviation  $\sigma_u$  around the mean value  $u_{\text{RBC}}$ , we analogously compute the values of  $r_{\text{trans}}$  for the values of  $u_{\text{RBC}} \pm \sigma_u$ . We thus compute the respective values of  $r_{\text{trans}}$  at these abscissa values, analogously to the previous case. Consequently, we obtain 9 values of  $r_{\text{trans}}$ .

We further consider the uncertainty of the experimental centroid positions, given as  $\pm s_p$  (cf.

section 2.4.2), which yield an uncertainty in the transition threshold of  $r_{\text{trans}} \pm s_p$ . For each of these two values, the aforementioned procedure is repeated, yielding a total of 27 predicted values of  $r_{\text{trans}}$ .

The entire set of values of  $r_{\text{trans}}$  is then simply converted into the corresponding values of the  $y$ -offset (cf. the definition of  $r_{\text{trans}}$  provided in section 3.3), yielding a transformation into values that exhibit an experimental equivalent.

Integrating the estimated probability densities of the experimental cell centroid positions at the entrance position in the limits of the obtained  $y$ -offsets finally yields the predicted fraction of croissants  $\phi$  of the numerical simulation:

$$\phi = \int_{-y_{\text{init}}}^{y_{\text{init}}} \text{pdf}(y|x = 0 \text{ mm}) dy. \quad (3.1)$$

Specifically, the mean value of  $\phi$  is obtained for the values of  $y_{\text{trans}}$  which are associated with the best guess for  $r_{\text{trans}}$ .

Of the remaining 26 values, we calculate accordingly the predicted fractions  $\phi$  and set the minimal value  $\phi_{\text{min}}$  as the lower bound for the corresponding error and the maximal value  $\phi_{\text{max}}$  as the upper bound for the error. These extremal results are indicated as triangles in Fig. 3.11, with down-pointing triangles denoting the largest estimate of  $r_{\text{trans}}$  and up-pointing triangles denoting the lowest estimate of  $r_{\text{trans}}$ .

A special case needs to be accounted for in this procedure at the croissant-only region of the numerical phase diagram. In the simulation setup, the maximal initial offset  $r_{\text{init}}^{\text{max}}$  is limited, depending in general on the initialized shape. As the entering RBCs in the experiment obey a manifold of shapes, this value of  $r_{\text{init}}^{\text{max}}$  is principally exceeded. To overcome this inconsistency, we set the value of the transition threshold as  $r_{\text{trans}} = 6$ , yielding correct outputs since the probability densities are normalized onto this interval, coinciding with the physical channel width.

As a major result, we thus obtain the predicted phase diagrams of the numerical approach for each imposed initial shape category. These predicted phase diagrams are depicted in Fig. 3.12. Overall, we find a good agreement between the predicted fraction of croissants from the simulations and the experimental counterpart. Interestingly, the employed slipper initial shape results in a very good agreement with the experimental data (cf. Fig. 3.12 (c)), and we therefore conclude that the initial shapes in the experiment are rather asymmetric, as is the slipper shape. Qualitatively, this holds with the observed starting cell shapes, mainly consisting of arbitrary, asymmetric others in the experiment.

The uncertainty in the prediction of  $\phi$ , indicated by the vertical error bars in Fig. 3.12, is relatively increased in the croissant-only region around  $2 \text{ mm s}^{-1} \lesssim u_{\text{RBC}} \lesssim 3 \text{ mm s}^{-1}$ , caused by the experimental velocities located in proximity to the sharp boundaries.

A comparison with existing studies on shape dynamics of RBCs in microcapillaries is possible, yet limited due to our specific geometries and flow parameters. However, the coexistence of croissants and others has been confirmed by Tomaiuolo *et al.* [57], by driving dilute blood suspension through a narrow cylindrical tube with a diameter of  $10 \mu\text{m}$ , resembling qualitatively our findings. Additionally, they observed coexisting regimes of croissants and slippers; however, for flow velocities triplicate our maximal imposed velocity. Although extrapolation of our phase diagrams seems plausible, we refrain from this approach, since the flow characteristics are generally differing due to a different Reynolds regime.

In non-circular channels, Chuitmans *et al.* [153] found coexisting croissants and others at

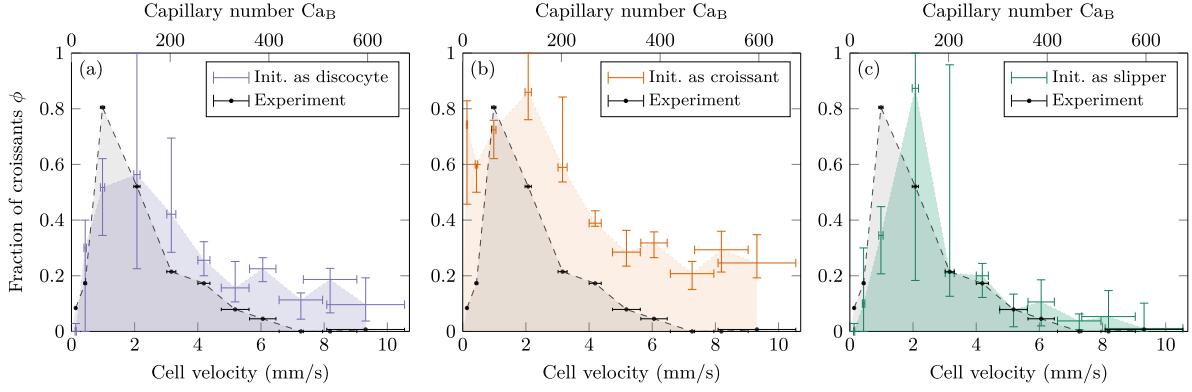


**Figure 3.12:** Overview of fractions of croissants  $\phi$  as predicted by the simulations and the experimental data. The initial configuration of the RBC shapes in the simulations varies among discocytes in (a), croissants in (b), and slippers in (c). The experimental data is represented by the dashed black line and the grey-shaded enclosed area, whereas the simulation data is indicated by the colored data points. The shaded areas and the connective lines serve as a guide to the eye. Horizontal error bars indicate the uncertainty of the obtained cell velocity and vertical error bars represent the uncertainty in the prediction, as described in the main text. Image adapted from reference [147].

low velocities ( $\lesssim 5 \text{ mm s}^{-1}$ ), as well as slippers for high velocities ( $\gtrsim 10 \text{ mm s}^{-1}$ ), albeit the cross-sections of their employed microchannels exhibit different aspect ratios with respect to our setup.

3D simulations carried out by Fedosov *et al.* [55] in cylindrical channels indicated a transition among the specified shapes, from slippers to parachutes (the equivalent of croissants in circular confinements). These findings match qualitatively with our established coexistence of TT-slippers and non-TT-croissants. In contrast to our simulation setup, they did not particularly focus on the initial condition.

Ultimately, Suzuki *et al.* [154] compared the deformation of RBCs in vitro and in vivo, leading to an in vivo phase diagram. For this purpose, vessels with different confinements and underlying flow velocities have been investigated, resulting in the observation that croissants dominate for low velocities and slippers for increased velocities and at smaller channel diameters. However, for low velocities, both croissants and slippers have been observed, matching our results. In addition, they find a croissant-only regime for  $1 \text{ mm s}^{-1} \lesssim u_{\text{RBC}} \lesssim 2 \text{ mm s}^{-1}$ , whose boundaries are almost identical to the ones obtained in our simulations.

Other studies mainly impose different viscosity ratios  $\lambda_{\text{visc}}$ , which makes them difficult to compare to our study, at least by quantitative means [17]. Nevertheless, they confirm qualitatively the emergence of slippers for high velocities and the dominance of croissants for low velocities.

Conceivably, a more detailed experimental approach is given by the method proposed in Quint *et al.* [155], using pre-stained RBCs flowing through inclined microchannels. Employing confocal microscopy, they can extract 3D information of the cell corpuscles. However, the pre-treatment and limited throughput in conjunction with the technical limitations in the resolvable RBC velocities render this approach as an ineligible basis for diagnostic tools.

### 3.6.2 Comparison of axial positions of RBCs

The extracted centroid positions from the simulation results reveal a centered position of croissant shapes, both in  $y$ -direction and in  $z$ -direction. Although we do not assess the  $z$ -information in the experiment, the centered distribution along the  $y$ -direction is mirrored, verified by the distribution of croissants as shown in Fig. 3.6 (a).

To achieve a quantitative comparison between the steady-state centroid positions in the experiment and the numerical approach, we analyze the peak positions of the final RBC distributions in the experiment, both for slippers and croissants. Due to the bimodal distribution of slippers, however, we consider the absolute value of the arithmetic mean  $|y_l - y_r|/2$  of both peaks. The resulting value thus corresponds to an equally-weighted average offset, accounting for the fact that both peaks are not necessarily equally pronounced due to the finite dataset. In Fig. 3.13, the radial offsets obtained via simulations and experiments are depicted, for both cell shape classes separately. Considering the average diameter of human RBCs,  $d_{\text{RBC}} \simeq 8 \mu\text{m}$ ,

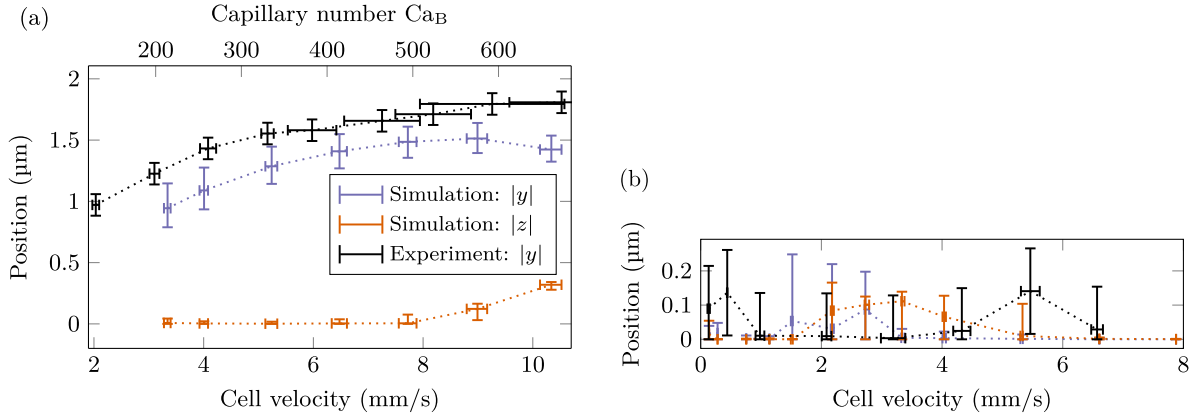


**Figure 3.13:** Comparison of final positions of converged RBC shapes obtained by simulations, and experiments, respectively. In (a), the slippers are depicted, whereas in (b), the offsets of uniquely croissants are shown. The mean absolute values in both cases are interconnected via the dotted lines as a guide for the eye. Horizontal error bars indicate the velocity error, given by the standard deviation  $\sigma_u$  of the cell velocities. Vertical error bars correspond to the general estimated uncertainty  $s_p = \pm 0.1 \mu\text{m}$  in detecting the centroid position for the experimental data, whereas it corresponds to the extremal values in the case of simulation data. Due to the experimental setup, no direct information about the  $z$ -offsets is provided. Image adapted from reference [147].

we find a systematic, yet minor deviation of  $y$ -offsets of ca.  $0.4 \mu\text{m}$ , or ca.  $0.05 d_{\text{RBC}}$  for slippers. We attribute this deviation to the fact that the cellular circumference is slightly out of focus to enhance visibility. Croissants, on the other hand, are positioned in the center, as is indicated by  $|z| \simeq 0 \simeq |y|$ .

A geometry with a mirrored aspect ratio and otherwise invariable setup can lead to encompassing investigations concerning the radial distribution of RBCs. Since the slippers tend to migrate towards the long edge of the cross-section, one can obtain not only additional images capturing the top-down view of these shapes, but rather determine the  $z$ -offset, which is inaccessible in the current setup. Further, the offset in both directions of croissants can be resolved statistically by this inversed channel aspect ratio.

### 3.7 Summary

The joint investigations of experimental and numerical RBC flow in microcapillaries reveal a rich shape phase diagram of two distinct shape categories, the off-centered slipper and the centered croissant shape. Whereas croissants mostly occur for low to intermediate velocities,  $u_{\text{RBC}} \lesssim 4 \text{ mm s}^{-1}$ , significant slipper populations emerge with higher velocities. The imposed flow velocities cover the entire range of velocities found in the microcirculation of human beings.

In the experiment, we record images displaying the projected cells and their centroid positions. The numerical approach, in contrast, yields detailed 3D information about the cell corpuscle. Additionally, the initial shape and position upon entering the microchannels can be altered in the latter case.

These initial shapes are varied among discocytes, croissants, and slippers. Apart from the temptingly logical fact that initially off-centered, asymmetrical slipper shapes favor slipper shapes as final states, and analogously, initialized croissants favor converged croissant shapes, we find pronounced bistability of the final shape.

Specifically, we find that the final RBC shape is bistable with respect to the initial position and imposed velocity for almost all velocities except a small region around approx.  $2 \text{ mm s}^{-1}$  where only croissants occur.

Albeit the technical restrictions regarding an initial focusing and shape determination, both methodologies show a very good congruence of the obtained experimental phase diagram and the predicted phase diagram from the numerical outcome. This is especially given for the predicted phase diagram with initialized asymmetric slippers.

Moreover, the final cell positions in both approaches show identical trends, with only minor systematic offsets in the case of slippers and negligible deviations in the case of croissants.

Our findings will help to elucidate the behavior of single RBCs in flow and can be easily generalized to more intricate structures due to the relative simplicity of the employed geometry. Furthermore, we prove that it is possible to hydrodynamically induce a certain cellular shape which will be useful for the development of cell sorting approaches, such as deterministic lateral displacement devices and in lab-on-a-chip structures in general.

We conjecture that deduced parameters of the phase diagrams are prone to subtle changes in the cells' mechanistic properties, especially the bending rigidity. Several diseases are linked to hemorheological alterations and thus, the presented methodologies might form the cornerstone of diagnostic tools, where precise knowledge of individual cellular parameters is inevitable.

Additionally, due to the employed physiological contrast ratio, we conjecture that our results can be generalized and mirrored by in vivo studies with concurrent geometries and flow parameters.

## Chapter 4

# Neural network approach for classification of RBC shapes

The following sections are intended to provide insight into the development of an artificial-intelligence-based classification technique of RBC shapes in microcapillary flow. The results have been subject to prior publication [156].

### 4.1 Introduction

In the preceding chapter 3, we presented a phase diagram of RBC shapes under microcapillary flow conditions. The classification of the RBC shapes has been carried out manually. Due to interindividual changes in size as well as cell-intrinsic physical parameters such as bending rigidity, the entirety of RBCs has some inherent variations in the exact cell shape, i.e., an individual croissant shape differs slightly from another one. By training, the human eye can adapt to this circumstance; however, it is highly non-trivial to decide when a cell is not any longer e.g. a croissant but “other”. Mathematically, one might think of measuring appropriate properties of cell images, such as circumference or axial symmetry, among others. In practice this task is time-consuming and it remains unclear what a reliable and robust parameter is to classify the observed shapes.

The manual classification is within its limitations so far the best choice, yet subjective. In terms of reproducible results, however, it cannot be guaranteed that manual classifications are free of erratic decisions, and thus form a subjective input.

To overcome these drawbacks, an artificial neural network (ANN) is developed, which is capable of detecting and classifying cell shapes into pre-defined categories. This ANN yields an unbiased classification of input images and provides a stable and highly efficient analysis once programmed and trained. Regarding the efficiency, we obtain a phase diagram predicted by the ANN in approx. 20s, which outmatches the manual approach by a factor of more than 100. Furthermore, no expertise knowledge is needed to apply the ANN algorithm on a recorded dataset. The training itself, however, is a crucial step in the development of ANNs and rather time-consuming. Accordingly, the gold standard is still the manual evaluation of cellular entities in blood smears, e.g. to determine the severity of sickle cell disease [157].

The features and results of the aforementioned ANN are at the focus of this chapter, which is structured as follows: First, an overview of the state-of-the-art in machine learning will be given, followed by a specific approach to classify biological cells with NNs. Compared to these, the used NN will be explained in detail and the output, i.e., the results will be shown to be in very good agreement with the manual classification.

## 4.2 Aspects of artificial neural networks

Throughout biological evolution, the ability of animals to adapt to their internal and external surrounding conditions is a key aspect of life. This task is fulfilled by the nervous system, which receives signals and compares these to the current state. By this action a change of the current state can be triggered, which is leading to better adaptations. The signals in the nervous system of pluricellular animals are propagated via cells specialized in saltatory conduction, the nerve cells, also termed neurons. Each neuron consists of a cell body, the soma, containing the nucleus as well as further organelles. From this soma, branched connectors to other cells emerge in a tree-like structure, the dendrites [158]. As soon as the cumulative signal received at the dendrites surpasses a certain threshold, the neuron gets activated.

Inspired by their biological counterpart, artificial neural networks (ANNs) are mimicking the processing of input arguments and obey the capability to adapt their internal parameters by a sophisticated training algorithm [159]. One of the conceptually simplest ANNs is the perceptron, as first proposed by Rosenblatt [160]. A schematic representation of this perceptron is presented in Fig. 4.1 together with a biological neuron and its main constituents. The perceptron receives an input vector  $\mathbf{x} = \{x_1, \dots, x_n\} \in \mathbb{R}^n$ ,  $n \in \mathbb{N}$  which is then multiplied by a vector  $\mathbf{w} = \{w_1, \dots, w_n\}$ ,  $n \in \mathbb{N}$ , and a bias term  $b \in \mathbb{R}$  is added.

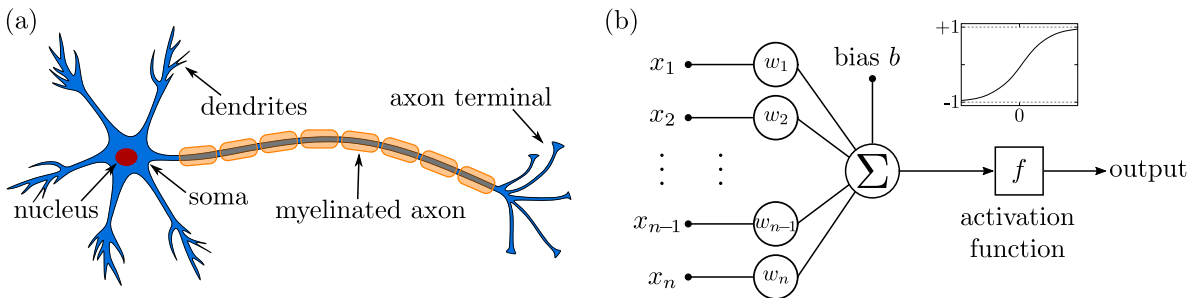


**Figure 4.1:** Comparison between biological neuron and artificial neuron. In (a), a biological neuron is sketched with its major functional components. Dendrites receive various signals via electrical stimuli. If the sum of these stimuli exceeds a certain threshold, a signal is propagated towards the axon terminal. (b) Schematic representation of an artificial neuron, receiving an input vector  $\mathbf{x} = \{x_1, \dots, x_n\}$ , which is adapted by a weight vector  $\mathbf{w} = \{w_1, \dots, w_n\}$  and an additive bias term  $b$  before being fed into a processing unit, the neuron. The resulting one-dimensional value is then passed onto an activation function  $f(\cdot)$ .

The result is forwarded to a non-linear activation function  $f(\cdot)$ , finally yielding the one-dimensional output value  $y \in \mathbb{R}$ :

$$y = f \left( \sum_{i=0}^n x_i w_i + b \right) = f \left( \mathbf{w}^\top \mathbf{x} + b \right). \quad (4.1)$$

Nowadays, one is tempted to employ activation functions such as e.g. the tan-sigmoid function  $f(x) = 1/(1 + \exp(-x))$  that can be approximated linearly close to the origin and rather quickly converge to the asymptote for distal input values to account both for mildly linear dependencies and ensure a saturation for extreme cases. Despite all the structural complexity of the perceptron, the mapping capability is limited. However, by iterative repetition of the process denoted by Eq. (4.1), i.e., feeding the output  $y$  of such a neuron to further neurons,

multi-layer perceptrons (MLPs) can be composed. The special case of only one layer, the single-layer perceptron, is used synonymously to the term perceptron. The arbitrarily deep structures of so-called hidden layers are composed of interconnected computation nodes, input nodes, and output nodes, with any input signal being transmitted layerwise through the MLP. The training procedure of the ANN can be subdivided into two categories. Historically and still very common has been the supervised learning algorithm, which is generically comprised of establishing the relationship between specified input-output data pairs. For this purpose, a cost function is defined that needs to be optimized, e.g. the mean-squared error of predicted values and assigned target values. Furthermore, the supervised learning algorithm can be subdivided into a mere processing step, where the predicted outputs of the respective inputs are calculated accordingly, forming the so-called forward pass. The gradient of the cost function with respect to the weights and biases is then back-propagated through the network structure. Based on this back-propagation, the parameters are adjusted with the aid of an optimization algorithm, typically gradient-based. The latter step can be regarded as the actual learning procedure, and the entirety of back-propagation and optimization is then repeated until the weights and biases ultimately converge.

However, the previous considerations are restricted to the class of supervised learning. In the case of unsupervised learning, one can use auto-associative data structures which are computationally intensive. Moreover, any modifications on the output range, etc. cannot be taken on by the user, such that the *black box* aspect of artificial neural networks is even aggravated, and therefore not discussed in this work.

## 4.3 State of the art in artificial intelligence

In recent decades, there has been steady progress in the development of neural networks, empowered by the growth in available computational power. The scope of applications in modern life ranges from content filtering [161] to speech recognition [162] up to object classification issues [163]. A typical process involved in the application and the design of neural networks is the so-called feature engineering. In the context of speech recognition, this feature engineering is based on a breakdown of language to single phonemes and syllables to a more coarse-grained word recognition.

### 4.3.1 Classification of biological cells

Albeit the tremendous capabilities of ANNs in object detection and classification tasks, the application in biological and life sciences is underrepresented. The origin of this scarce distribution of newly developed approaches is multifaceted, yet collapsing into two major arguments: On one hand, the sheer variability of biological specimen demands for an equally high number of individual diagnosis tools, each with a specialized training procedure to account for. On the other hand, the data storage and technical resolution limits have been restricting the automated analysis in the past. Even nowadays, the differential counting of leukocytes, one of the most frequently determined clinical laboratory parameters, is often assessed manually [164]. As such, the main analytic process remains unmodified since its emergence nearly a century ago [165]. Few studies address automated cell classification based on image data files. Restricting the plethora of various biological cells to the phenotypes of RBCs, recently developed ANNs are capable of discriminating sickle cells among discocytes [166], or used

bright-field microscopy images to classify upon their morphology in 2D [167]. Tripathy *et al.* [168] used the identical methodology to discriminate breast cancer cells among healthy cells. A joint approach of confocal imaging and ANNs has been proposed to use the intercellular information of actin filament structures as a future diagnostic marker for breast cancer cells and healthy cells [169].

Sophisticated approaches based on angular radial transformations of RBC shapes in flow have been proposed recently by Apostolopoulos *et al.* [170], and in addition to self-organizing maps, by Kriegel *et al.* [171]. Similarly, Simionato *et al.* [172] developed a neural network-based diagnostic approach to discriminate RBC shapes under healthy and pathological conditions, based on spherical harmonics spectra. Albeit the success in classification and detecting the RBCs in the aforementioned works, they involve time-intensive data acquisition techniques, such as staining protocols, sophisticated microscopy tools, and the transfer of huge data structures. In general, there is a trade-off between high-throughput devices and the resolution limits of the imaging technique. For the development of diagnostic tools, it is evident that the processing time needs to be minimized.

## 4.4 Architecture of the neural network

The design principles of NNs are governed by the assigned task they are supposed to resolve. In the case of classification issues, the most prominent NN type is the so-called convolutional neural network (CNN). In fact, the advantage of this network type is the translation invariance, i.e., the outcome of the CNN approach is unaffected by the position of the objects in the input image, which is a direct mathematical consequence originating from the convolution operation.

In the case of RBC shapes in flow, we observe two distinct shapes, the croissant and the slipper, respectively, and a third category of merely unknown shapes with arbitrary morphologies. In the latter case, one might be able to define subcategories of cell shapes, such as e.g. multilobed RBCs [150] or cells resembling slippers that are tilted by  $\pi/2$  versus the optical axis. Yet, these subcategories do not form a quantifiable population when analyzed manually, and thus, we identify them as others. Conclusively, training a CNN for others is highly non-trivial given the sheer diversity of individual shapes.

A typical classification network is characterized by the assignment of labels to input objects, thus providing a binary output. Yet, in order to account for these others, we construct a regression-based neural network rather than a default classification network by assigning quantitative outputs to the input data. Subsequently, we will define thresholds for the individual RBC populations, as outlined in section 4.4.5.

The final, i.e., the optimized architecture of the employed CNN consists of three convolutional layers, with a schematic representation provided in Fig. 4.2. At the initial stage, an arbitrary input image is fed into the first layer of convolution kernels, consisting of 25 individual matrices of dimensions  $21 \times 21$ . The convolution of the input image exhibiting the dimension  $90 \text{ px} \times 90 \text{ px}$  with these matrices results in 25 intermediate images, or subimages, each of dimension  $70 \text{ px} \times 70 \text{ px}$ . This operation is sketched in Fig. 4.3, showing an image montage of the entire set of convolution kernels as well as the intermediate croissant and slipper images, respectively, after the convolution operation. For the sake of visibility, a false color mapping has been applied to the individual images in Fig. 4.3.

These intermediate images then undergo rectifying linear units (ReLU), which is an essential

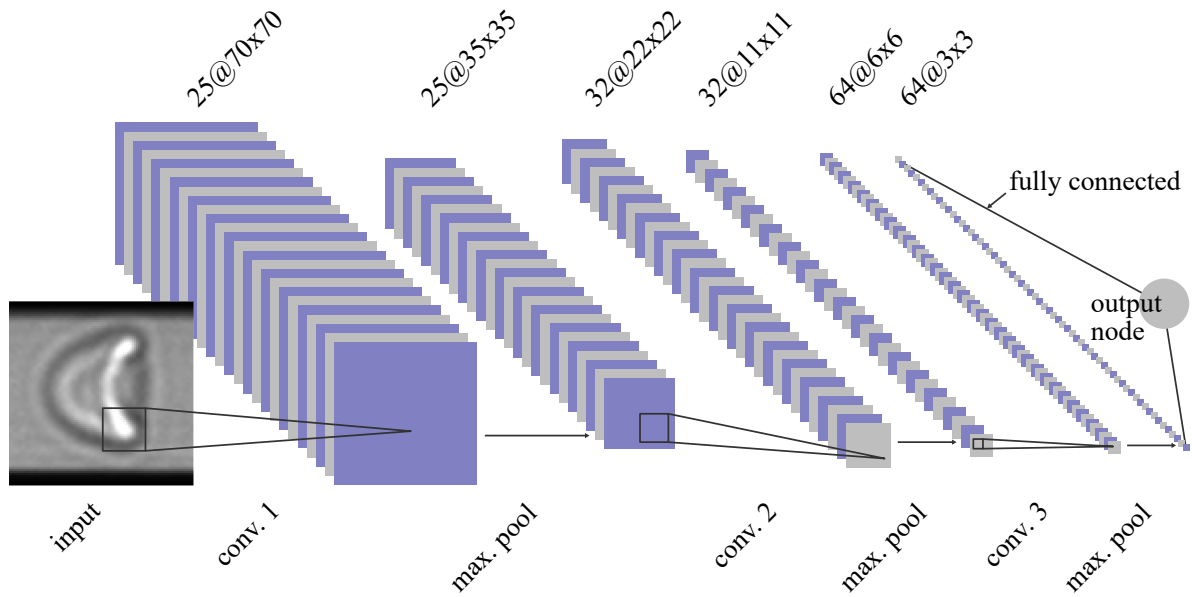


**Figure 4.2:** Schematic representation of the various CNN layers. As input arguments, cell images with a dimension of  $90 \text{ px} \times 90 \text{ px}$  are accepted. These images are preprocessed to suppress the influence of border effects and maintain a uniform image background. Therefore, the initial image pixels are weighted by a Tukey window with  $\alpha = 0.25$ , as given in Eq. (4.2), leading to a gradual fade out towards the upper and lower edges. The first processing stage of the images consists of a convolution with 25 convolution kernels, each with a size of  $21 \times 21$ , yielding 25 intermediate images with sizes  $70 \text{ px} \times 70 \text{ px}$  each. In the next processing step, a non-linear transformation function (ReLU) is applied. Consequently, these resulting intermediate images are down-sampled by a factor of 2 in each dimension via a max pooling operation. The entire group of operations, convolution, ReLU, and max pooling are repeated twice, yet with diverse convolution kernels. Finally, the output neuron interconnects all kernel elements of the last processing stage, mapping them onto an output range via a linear transfer function. All individual kernels and the input image obey properly scaled dimensions. Image adapted from reference [156].

step for the stability of the CNN. These stepwise linear functions map the individual kernel elements  $z$  onto  $z = \max(z, 0)$ , thus providing a nonlinear element in the entire process of convolutions. Since the convolution stages can be decomposed into linear transformations, the CNN without ReLU layers would collapse into piecewise linear functions and thus lack the capability to learn higher-order dependencies among the parameters. Additionally, the application of ReLUs is known to suppress the problem of vanishing gradients as encountered in training approaches of ANNs with many layers. This effect refers to small error gradient metrics, which do not affect training performance when back-propagated through the layer structure up to the input layer. As a result, the final ANN remains in a poorly trained state [173].

Maximum pooling, henceforth abbreviated as max pooling, is then applied to down-sample the feature maps. Here, the max pooling algorithm obeys a fixed stride value of 2, allocating the maximal value of each  $2 \times 2$ -sized patch in every kernel while omitting the remaining three values. Eventually, the kernel dimensions are halved in each dimension, yielding an increase in computational performance due to the reduced amounts of data being processed. Furthermore, this operation ensures a robust convergence, since only the most prominent features remain in subsequent iteration steps instead of an average feature map, which is prone to

encode adverse spatial information [174]. Pooling operations are inspired by the hierarchical composition of image features, where objects are composed of parts, which in turn are a combination of motifs and edges. By subsequently condensing these similar image patches that are passed from previous layers into one, a pooling operation ensures an invariance against shifts and atypical distortions and accentuates qualitative characteristics of objects.

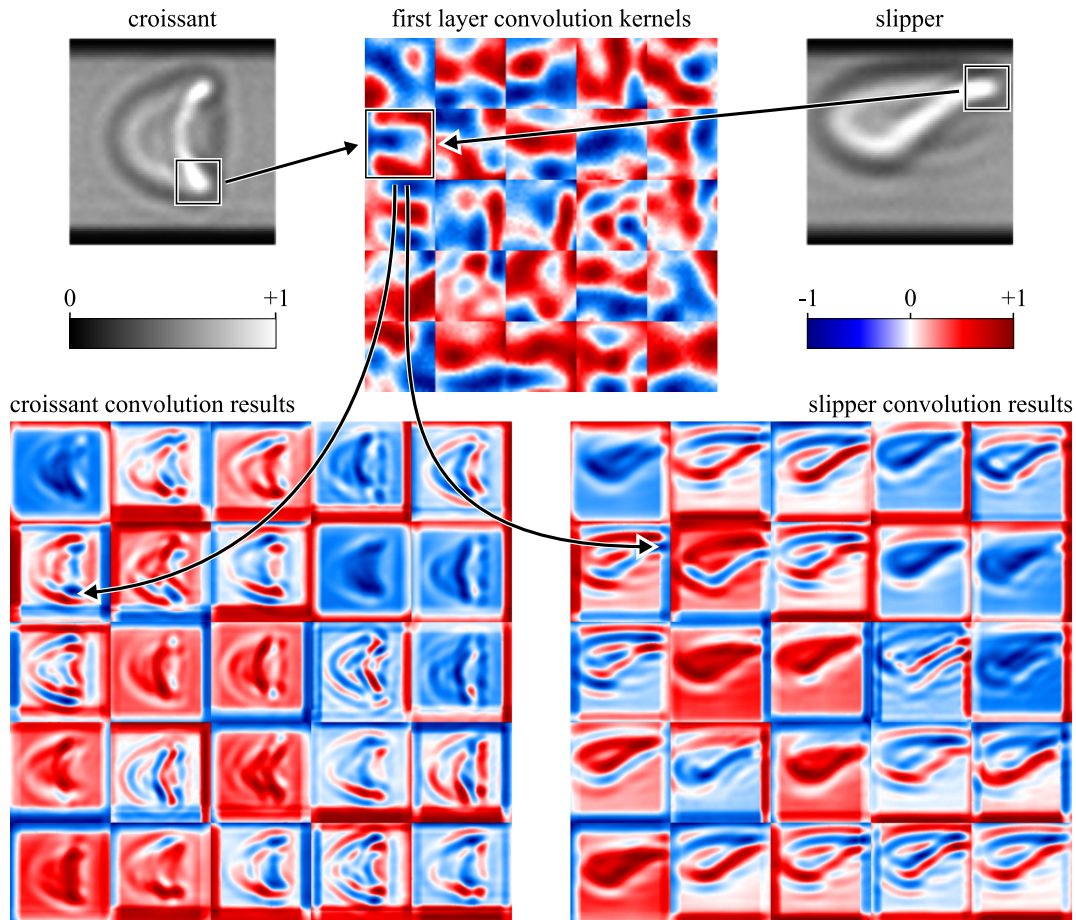


**Figure 4.3:** Outcome of the first convolution stage in the trained CNN. The input image (croissant and slipper, respectively) is therefore convoluted with 25 individual kernels of size  $21 \times 21$ , resulting in 25 intermediate images (as montage) of size  $70 \text{ px} \times 70 \text{ px}$  each. Distinctive features of the respective RBC shapes in the input images are marked by a circumscribing black square. Ensuing transformations are marked following the black arrows, finally culminating in enhanced features. Both for the convolution kernels as well as for the final image montage a false-color mapping is utilized to improve visibility. Image adapted from reference [156].

Consecutive processing steps consist of the application of further convolution kernels and subsequently, reLU layers and max pooling, yet with different dimensions of convolution kernels. In total, the employed CNN consists of three convolution layers and an equal amount of max pooling layers and reLUs, respectively. The entire structure is depicted in Fig. 4.2 and an overview of the individual kernel sizes and resulting subimage sizes is provided in Tab. 4.1. Lastly, the output node interconnects all kernel elements of the last processing step and maps them onto a linear range, enabling them to be processed further.

**Table 4.1:** Overview of the architectural details of the used CNN. In the leftmost column, the descriptors of all layers are given, corresponding kernel sizes are presented in the middle column. In the rightmost column, the resulting subimage sizes are given, which are obtained after application of the respective layer.

layer	kernel size	subimage size (px <sup>2</sup> )
input layer	-	90 × 90
convolution layer 1	21 × 21	70 × 70
reLU layer	-	70 × 70
max pooling layer	2 × 2, stride 2	35 × 35
convolution layer 2	14 × 14	22 × 22
reLU layer	-	22 × 22
max pooling layer	2 × 2, stride 2	11 × 11
convolution layer 3	6 × 6	6 × 6
reLU layer	-	6 × 6
max pooling layer	2 × 2, stride 2	3 × 3
output layer (regression type)	-	1 × 1

#### 4.4.1 Image preprocessing

As outlined in section 2.4.2, we obtain cropped images of flowing RBCs in microchannels with the aid of tracking data from datafiles obtained by brightfield microscopy. Furthermore, non-isolated cells are sorted out, i.e. trains or clusters of cells whose intercellular distance is too small such that hydrodynamic interactions are not negligible any longer. The installed optical setup leads to typical maximal cell dimensions of 80 px in the final footage. Cellular positions are computed by their two-dimensional center of mass, which can shift laterally for some pixels due to the binarizing threshold. To account for this issue as well as for minor physiological variations in cell size, a cropping window of 90 px × 90 px has been chosen.

In total, we obtain 3,090 images from three individual healthy donors and therefore, the lighting conditions and the contrast in the final footage are inconsistent, albeit the deviations are relatively small. However, to disregard the influence of the contrast on the output of the CNN, we apply a histogram matching approach onto the entire image set, leading to uniform contrast distributions.

Subsequently, the full image space has been exploited by mapping the pixel values to the entire 8-bit range with the lowest and the highest 1% of all pixel values being saturated. As a consequence, the image pixels exhibit increased signal dynamics and we achieve robustness of the following CNN approach towards marginal illumination discrepancies.

The post-processing is then comprised of applying a window function, yielding a fade-out towards the upper and lower channel edges. This routine accounts for equal image boundaries,

since the channel walls obey inaccuracies which may lead to malclassified cell images. As window function, a so called Tukey window function  $w(y)$  is employed:

$$w(y) = \begin{cases} \frac{1}{2} [1 + \cos(\frac{2\pi}{\alpha}(y - \frac{\alpha}{2}))], & 0 \leq y < \frac{\alpha}{2}, \\ 1, & \frac{\alpha}{2} \leq y < 1 - \frac{\alpha}{2}, \\ \frac{1}{2} [1 + \cos(\frac{2\pi}{\alpha}(y - 1 + \frac{\alpha}{2}))], & 1 - \frac{\alpha}{2} \leq y \leq 1, \end{cases} \quad (4.2)$$

where  $y$  denotes the normalized vertical pixel position ( $0 \leq y \leq 1$ ) of any individual image.

#### 4.4.2 Prerequisites and limitations

The basic architecture and the design principles are chosen to fit the specific needs in our employed setup. Adaptations in the various steps in image-preprocessing routines contribute to a uniform dataset with the constraint of optimizing the performance. To guarantee these potentially sensitive optimality principles, we stress that any alterations in the optical setup, as well as the experimental setup, need to be neglected. Specifically, the usage of a different light source, e.g. blue light, might affect the classification of RBC shapes. Similarly, upscaling or downscaling, respectively, of cropped images can influence the outcome of the CNN approach. Most importantly, the classification algorithm is outlier tolerant, yet, with respect to the entirety of RBC shapes. Other cell types, such as e.g. WBCs, have not been considered in the training approach and thus cannot be discriminated by the CNN. Hence, features reminiscent of the RBC characteristics might lead to misclassified images. In its current form, the CNN cannot be adapted towards more cell types but rather has to be retrained with a tailored set of training data including the additional cell class.

#### 4.4.3 Implementation details

As a prerequisite of the CNN to perform a classification, we have to train the network on a dedicated training dataset. A crucial feature of the training dataset to ensure a robust training procedure is the mutual exclusivity from the actual dataset. Based on the neuron's output of this training data the randomly initialized convolution kernels are updated. The establishment of a suitable training dataset is one of the key aspects of the training procedure. In principle, this training procedure is an optimization problem, comprising of the minimization of a predefined error function. Thus, the finding of an appropriate optimization strategy and an eligible error function form two remaining issues to train the CNN.

As the error function to characterize the actual training step, we choose the root-mean-square-error function (RMSE), given as

$$\text{RMSE} = \left[ \frac{1}{N} \sum_{n=0}^{N-1} (o_n - t_n)^2 \right]^{1/2}, \quad (4.3)$$

with the momentary output value of the  $n$ -th input image  $o_n$  and the corresponding target value  $t_n$ . For regression networks, the RMSE is a standard loss function; however, we specifically choose this function to penalize large deviations from the target value to guarantee a disentanglement between the output values of the distinct cell shape categories.

To minimize the error function specified in Eq. (4.3), we apply a gradient descent algorithm.

For this purpose, we condense the entirety of kernels, representing the weights in the employed CNN, in the vector  $\theta \in \mathbb{R}^p$ , with  $p$  being the cumulated pixels of all kernels. Consequently, the vector  $\theta$  is updated to minimize the cost function, abbreviated as  $E(\theta)$ :

$$\theta_{k+1} = \theta_k - \lambda \nabla E(\theta_k), \quad (4.4)$$

with  $\lambda$  being the learning rate, specifying the step towards the negative gradient to update the kernels and the iteration steps  $k$ , and  $k + 1$ , respectively. Adding a fraction of the previous update vector to the current update vector ensures circumventing local minima and a suppression of oscillating training curves and hence achieving a faster convergence towards the global minimum [175, 176]. Eq. (4.4) thus transforms to

$$\theta_{k+1} = \theta_k - \lambda \nabla E(\theta_k) + \gamma (\theta_k - \theta_{k-1}). \quad (4.5)$$

Due to the structural analogy with the equations of motion for solid bodies, this additive fraction of past update vectors resembles the momentum. Hence, Eq. (4.5) is referred to as a stochastic gradient descent algorithm with momentum and  $\gamma = 0.9$  has been set as the momentum parameter.

Iteratively, a value of  $\lambda = 0.001$  has proven to be the optimum choice in the current setup, since higher values tend to overtrain the neural network, as can be seen from increasing oscillations during the training approach [177]. Lower values, on the other hand, drastically increase the computation time without any gain in performance.

As a common practice to increase convergence, the iterative training process is only performed on a subset of the whole training dataset [178–180]. We therefore define so-called mini-batches, each consisting of 128 training images. Although the optimal mini-batch size is still under debate, from preferably low-dimensional [181] to high-dimensional [182], the current value of 128 yields a robust training convergence in conjunction with a fast training process. The temporal evolution of the training approach is depicted in Fig. 4.4. Starting with randomly initialized weights, the training state is depicted for each pass of a mini-batch. The outcome will then be used as the starting point for the subsequent training iteration with a second randomly chosen mini-batch. To evaluate the sensitivity of the training procedure, we additionally calculate the loss function of a dedicated validation dataset, consisting of a subdivision of 5% of the whole training dataset, whereas the true training data constitutes the remaining 95% of the entire image dataset (cf. section 4.4.4). Most importantly, both validation data and true training data form disjoint datasets, such that any interference can be neglected. Moreover, both datasets are shuffled randomly in order not to maintain any intrinsic labeling scheme as a potential feature to train for.

The validation loss is calculated after every complete processing cycle composed of 50 mini-batches. Once the entire training dataset has been iterated, a so-called epoch is finalized. Preventing an overtraining of the CNN, which is indicated by a diverging evolution of training and validation, we implement certain termination criteria for the training approach. For instance, a total number of ten training epochs is fixed, noticing that an increase of this number does not lead to a substantial gain in performance. Additionally, the training will be terminated after a successive quintuply increase of the validation loss.

Among all hyperparameters that need to be optimized, the mini-batch size is tuned first, followed by the learning rate. With their optimum values, the remaining hyperparameters are tuned, such as the learning rate and the momentum parameter, respectively.

All training approaches can be performed either on a CPU or a GPU. In this work, a high-

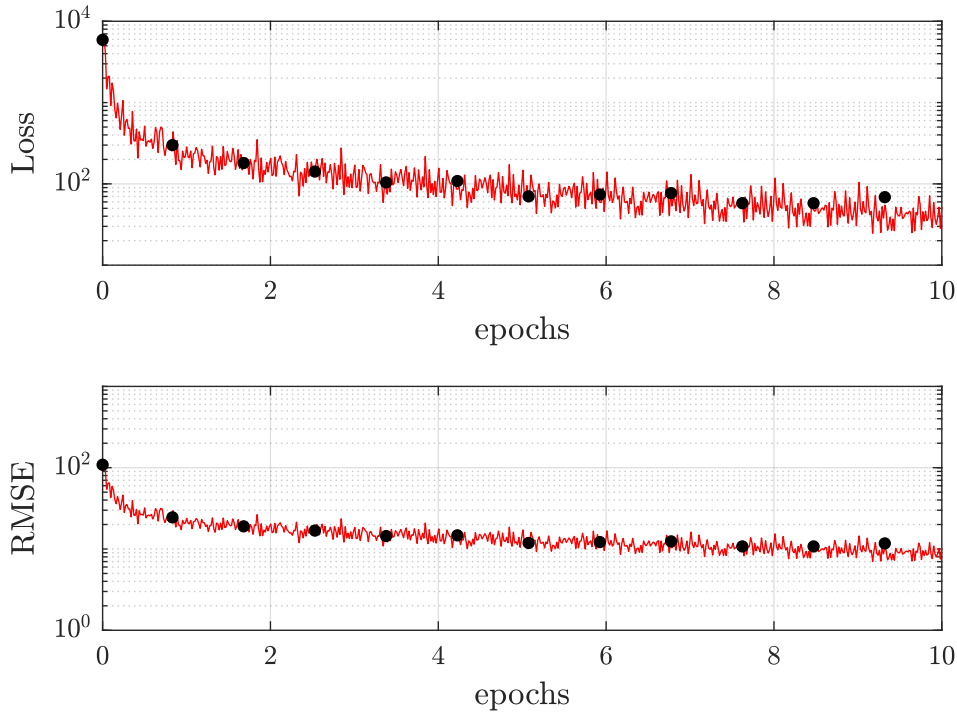


**Figure 4.4:** Evolution of (a) RMSE and (b) loss with an increasing number of training epochs. The red curve indicates the interconnection of subsequent mini-batch iteration steps, the black circles correspond to the validation, each being evaluated after processing 50 mini-batches. A limit of ten training epochs has been implemented as a termination criterion to inhibit overtraining. Image adapted from reference [156].

performance graphics card (Intel GeForce GTX 1080 Ti) has been used to minimize the elapsed time.

#### 4.4.4 Acquisition and characteristics of training data

To perform a robust training of the CNN, we record a set of training images containing RBCs in flow under identical conditions as the latter input data. In particular, 1,500 slippers and 1,500 croissants are obtained, where in both cases the final number is doubled by horizontal mirroring of the respective images and exploiting the systemic geometry. Every cell image has been classified manually and labeled uniquely, i.e., no image has been used more than once for training purposes.

Although the total number of these training images has proven to be sufficient a posteriori, first training approaches could not validate a mutually exclusive classification of croissants and others. We conjecture that others form a subcategory of so-called sheared croissants, i.e., RBCs obeying similar characteristics as croissants, yet with an elongated and partially asymmetric “tail” (cf. cell images in Fig. 4.5).

Based on these observations of insufficiently trained CNNs, we additionally recorded training images of sheared croissants to account for this subclass. We stress the fact that these sheared croissants are not mirrored as a subcategory in the phase diagram but only contribute to the count of others. In this sense, the sheared croissants are only an auxiliary category of cell shapes.

Due to the relatively less occurring sheared croissants with respect to the remaining shape categories in a typical experimental dataset, a total number of 2,000 sheared croissant images is used for the training procedure, originating from 1,000 recorded images by horizontal mirroring as for the formerly described shape classes.

To inhibit a biased training towards distinct pressure drops we recorded the corresponding training images arbitrarily at a pressure regime where they form the predominant shape category, yielding a profound variability among the individual cell shapes within the respective shape categories. Specifically, croissant training images are recorded from 100 mbar – 200 mbar, slippers from 700 mbar – 1,000 mbar, and sheared croissants from 300 mbar – 500 mbar.

Albeit the lighting conditions during the conducted experiments are manually controlled and adjusted to ensure a constant final footage, slight variations may occur. To render our training approach invariant against these minor changes in the illumination, we randomly alter the intensity of the microscopy light source in a range of 50 % – 80 % with respect to the available maximum intensity for each subset of the training data and a subsequent contrast adjustment, identical to the one described in section 4.4.1.

Lastly, we intentionally include images of defocused RBCs in the training data, accounting for optical misalignments and inherent minor curvatures of the microfluidic chip in the flow direction. These defocused cell images are obtained via recording RBCs in flow at different positions in an inclined microfluidic chip.

In sum, the above principles yield a robust training algorithm, which is capable of an unbiased analysis of input data.

#### 4.4.5 CNN output and benchmark

Once the training algorithm is successfully converged, the accuracy of the CNN output has to be validated. This benchmarking is typically realized by opposing the CNN output to the respective manual classification. However, since the specific design of our CNN yields decimal values, no direct comparison is possible. Instead, a spectral representation of the individual output values is chosen, as depicted in Fig. 4.5. Since the individual cell images of the distinct cell shape classes are uniform for the human eye, we assume their corresponding CNN output values to be narrowly distributed. The output values clearly obey this narrow distribution, as indicated by the peaks in Fig. 4.5. The peak associated with slippers is situated at an output value of  $\approx -117$ , although the target value of the slipper class has been set to  $-127$  in the training process. We attribute this deviation to variations in the optical imaging resulting from focal shifts and lighting conditions. Furthermore we assume that slipper shapes indeed obey variations in the exact morphology, leading to an exploitation of the full target interval and thus to a shift of the lateral peak position.

Similarly, the peaks of the CNN output values of croissants and sheared cells are relocated with respect to the initial target values, towards  $\approx 115$  in the case of croissants (target value 127) and  $\approx 40$  in the case of sheared croissants (target value 64). However, these lateral shifts do not affect the following analysis of cell shape classes since their thresholds are based on standard deviations rather than mean values, i.e., positions.

To define the intervals of the respective predefined classes, we apply a fit with four Gaussians to the spectral distribution of the output values, with one Gaussian each being associated to the individual classes (croissants, slippers, sheared croissants), and one Gaussian to account for the background noise emanating from indistinguishable shapes.

In a first attempt, we heuristically set the threshold of each shape category to a value of  $1\sigma$

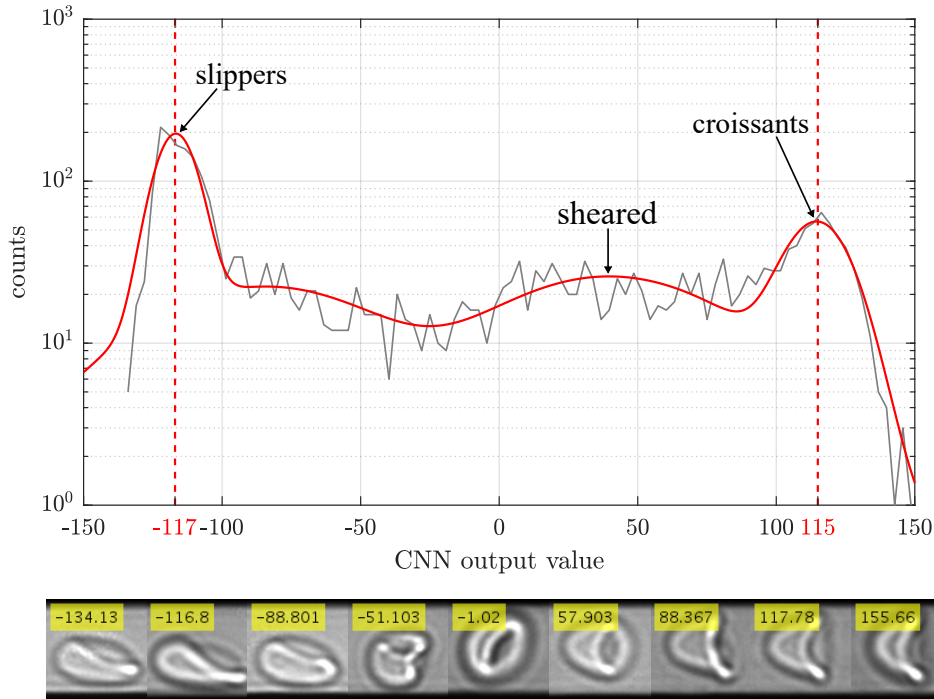


**Figure 4.5:** Spectral representation of cell counts for the entire interval of CNN output values. The individual counts are represented by the grey line, which is then fitted by four independent Gaussians, indicated by a solid red line. Three of the peaks are associated with the distinct cell shape classes, namely, the slippers, the croissants, and the auxiliary class of sheared shapes, as denoted in the graph. In the lower panel, typical snapshots of flowing RBCs with their corresponding CNN output values in the yellow-colored box are depicted. The images are ordered by increasing CNN output values, starting from slippers (subimage 1-3) via ambiguous others (subimages 4, 5) to sheared shapes (subimages 6, 7) through to croissants (subimages 8, 9). Image adapted from reference [156].

of the corresponding Gaussian fit function of croissants ( $\sigma_{cr}$ ), and slippers ( $\sigma_{sl}$ ), respectively. Thus, all cells obeying output values outside these regions contribute to the class of others. In Fig. 4.6 (a), the CNN output of the entire dataset is depicted, with the colored areas corresponding to the respective standard deviation. To benchmark this threshold, we now compare the resulting predicted phase diagram to the manually obtained one. From Fig. 4.6 (b), we observe a drastic underestimation of croissants for the first case with respect to the latter. Similarly, slippers remain underrepresented throughout the applied pressure drops; however, the qualitative characteristic of the phase diagram is reproduced.

An increase of the interval length of each population to a value of  $2\sigma_{cr}$ , and  $2\sigma_{sl}$ , respectively, enhances the conformity with the reference phase diagram, as shown in Fig. 4.6 (c, d). Yet, slipper populations are still systematically underestimated with respect to the manually obtained phase diagram, yielding especially a wrong transition point of equal fractions of both populations, which is assumed to be a distinctive feature of RBCs under healthy and pathological conditions.

Instead of considering the standard deviation as the unique determinant of the assigned populations, we develop an adapted threshold range of each shape class. Therefore, we define a cost function, consisting of the sum of all misclassified cells.

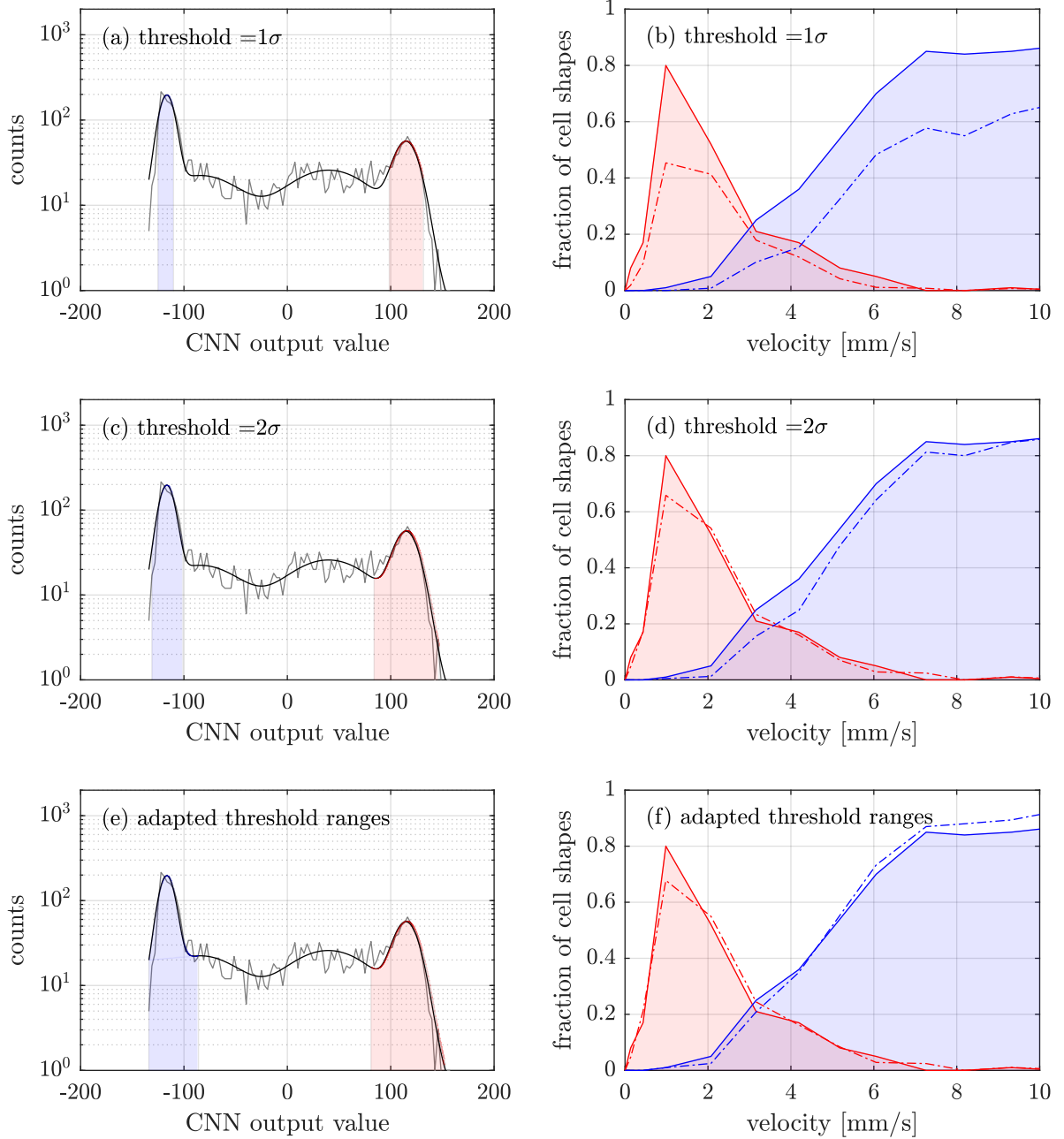


**Figure 4.6:** Comparison of predicted phase diagrams by the CNN and the manual phase diagram. The left column depicts the CNN output spectrum of the entire recorded dataset (grey line). Four Gaussians have been fitted to the data points, indicated by the solid black line. These Gaussians represent the contribution of the three distinct classes and the background as the sum of indistinguishable cell shapes. Thresholds have been chosen as (a)  $\sigma$ , (c)  $2\sigma$ , (e) adapted thresholds, to define the respective corresponding cell shape intervals, indicated as blue shaded (slippers) and red shaded (croissants) areas. The corresponding predicted phase diagrams are presented in the right column (b, d, f), alongside the manually classified one. The former are indicated by the dash-dotted lines with identical color codes as in the left column, whereas the latter are represented by the solid lines and their enclosed shaded areas. In all phase diagrams, the lines consist of straight line segments between the discrete set of data points to guide the eye. Image adapted from reference [156].

In particular, we find false positive croissants and slippers, respectively, as well as false negative croissants and slippers, respectively. The term false positive hereby refers to cell shapes being assigned to a distinct shape class according to the CNN output value, in contradistinction to the manual reference class. Accordingly, manually assigned categories that are not reproduced by the CNN outcome yield false negative cell shapes.

Consequently, we iterate for each population the corresponding thresholds by minimizing the sum of falsely classified cell shapes around the respective peak position. These optimized thresholds are found to be  $116.8 \pm 35.5$  in the case of croissants, and  $-116.6 \pm 28.5$  in the case of slippers and yield a very good prediction of the phase diagram with respect to the reference phase diagram, as indicated in Fig. 4.6 (e, f).

An image montage of this minimal set of falsely classified slippers is presented in Fig. 4.7, and analogously, the minimal set of misclassified croissants is depicted in Fig. 4.8.

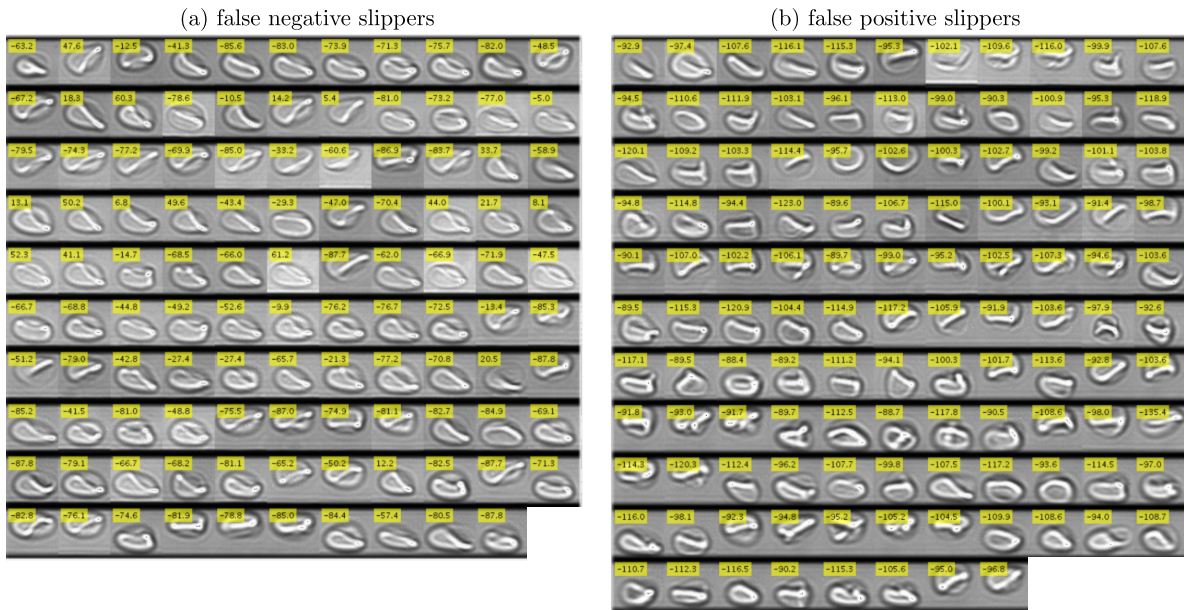


**Figure 4.7:** Overview of falsely classified slippers. (a) Image montage of all RBCs not classified as slippers by the CNN, contrary to the manual classification (false negative slippers). (b) Image montage of all false positive slippers, i.e., RBCs being classified as slippers according to the CNN, but not by manual evaluation. Numbers in yellow boxes correspond to the respective CNN output values of the cell image. Image adapted from reference [156].

The final result of the CNN-based prediction is constituted in the confusion matrix in Tab. 4.2, relating the predicted shape categories to the reference shape categories. Although the absolute numbers of the falsely classified slippers and croissants are almost identical, we stress that the relative deviation of the results is lower in the case of slippers due to the increased number of corresponding images in the dataset. The final error of the classification is governed by these misclassified cell images, and since the adapted threshold ranges are directly influenced by the subjective classification, the actual rate of misclassified cell shapes might be lower than the present one if a revision of the manual classification is considered. Intriguingly, the CNN outputs of slippers and croissants are mutually exclusive, i.e. we achieve a true disentanglement of the two shape categories.

In addition to relative errors in Tab. 4.2, we take into account further metrics to evaluate the performance of the CNN. For brevity, we denote the false positive number by  $FP_i$ , with

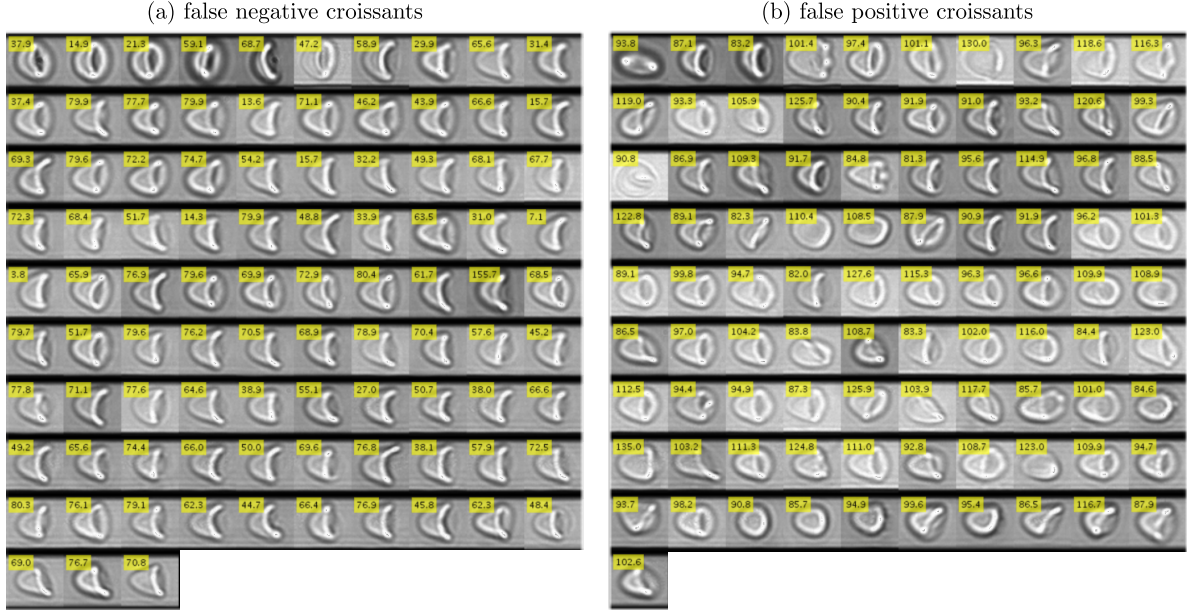


**Figure 4.8:** Image montage of all misclassified croissants. (a) Randomly ordered collection of actual croissant images that have been classified as others by the CNN (false negative croissants). (b) Assortment of all false positive croissant shapes, i.e., designated croissant shapes according to the CNN output, contrasting the actual shape class. Image adapted from reference [156].

**Table 4.2:** Overview of all false positive and false negative identified cells. Additionally, the correctly classified cells are shown on the main diagonal axis. This so-called confusion matrix serves as a benchmark for the performance of the trained CNN. The relative numbers with respect to the sum of the absolute column values are given as a percentage, followed by the respective absolute number in parentheses.

predicted class	actual class		
	croissant	slipper	other
croissant	85.6 % (551)	0.0 % (0)	8.2 % (91)
slipper	0.0 % (0)	91.8 % (1227)	10.6 % (118)
other	14.4 % (93)	8.2 % (109)	81.2 % (901)

$i \in \{\text{sl}, \text{cr}\}$ , denoting the croissant or slipper shapes, and analogously,  $FN_i$ ,  $TP_i$ , and  $TN_i$ , for the false negative, the true positive, and true negative numbers, respectively. The exactness of our CNN approach can then be quantified by calculating the precision, given as the fraction  $TP_i/(TP_i + FP_i)$  of true positive and the sum of both true positive, and false positive values, separately for each shape category. Accordingly, the sensitivity is considered, as a measure of the completeness of the classification. This sensitivity is hereby defined as the proportion of correctly labeled positive shapes,  $TP_i/(TP_i + FN_i)$ . The specificity, on the other hand, is defined as the proportion of true negatives,  $TN_i/(FP_i + TN_i)$ . Calculated values of these metrics for both slippers, and croissants, are displayed in Tab.4.3. Essentially, the slipper classification is more robust in terms of precision and sensitivity compared to croissants. We

**Table 4.3:** Standardized metrics of the trained CNN for each predefined cell shape category.

actual class	metric		
	precision	sensitivity	specificity
croissant	85.8 %	85.6 %	96.5 %
slipper	91.2 %	91.8 %	94.0 %

attribute this circumstance to the fact that croissant shapes are located in proximity to the auxiliary class of sheared croissants, exhibiting a large mutual similarity. Therefore, the lower bound of the confidence interval in the case of adapted thresholds, distinguishing croissants from others, captures a noticeably high fraction of sheared croissants. This fraction then manifests as an increased amount of false positives, finally decreasing the precision for the croissant population. Similarly, the false negative count is relatively increased by indifferent croissants subject to human input. However, we note a high specificity of our CNN-based classification for both populations, implying a high outlier tolerance.

According to these metrics, the presented CNN exhibits an outstanding performance compared to the manual classification tasks of RBCs. Besides unbiased classification, the deployed CNN is several orders of magnitude faster than any human being, yielding a complete phase diagram in few seconds, compared to several hours in the latter case. We customized the architecture of the presented CNN to fit the specific needs of our classification. As a benefit, the structural principles of the neural network are relatively simple compared to typical libraries of NNs, such as e.g. AlexNet [183]. In fact, they tend to be overengineered regarding our binary classification scheme of RBC shapes, such that enormous amounts of training data need to be recorded and provided to reliably train the CNN for the feature extraction.

We stress that the presented classification approach is not exclusive with respect to the underlying ANN type. However, the advantage of the CNN lies in the automated feature extraction, which does not require any understanding of abstract features in image sets. Instead, invariant features are generated from raw data and passed onto subsequent layers, where the entire process is iterated until eventually, the CNN output has converged.

## 4.5 Summary

Artificial-intelligence-aided classification of biological specimens is a growing field of interest. Empowered by the manifold of applications, the individual choice of the underlying algorithms is a crucial, yet intricate task. The feature engineering of input data structures in this task is an inherent problem that needs to be solved. Existing neural network structures typically involve many layers, demanding enormous training datasets. Furthermore, we seek to distinguish distinct croissant and slipper cell shapes from a group of miscellaneous shapes, the class of others. However, the diversity of the latter category increases the complexity of a training approach. To overcome these drawbacks, we designed a CNN to classify the input data according to our manually predefined ternary classification. Our approach employs a regression-based CNN rather than a typical classification-based CNN to define output values and yielding the opportunity to declare outliers.

In the context of predicting a shape phase diagram of RBCs, we therefore trained a CNN capable of mapping individual RBC shapes onto a linear output scale. Applying an iterative thresholding sequence onto these output values by minimizing a customized cost function produces a phase diagram in very good accordance with the reference phase diagram.

Thus, we conjecture that this approach renders the basis of future investigations towards the automatized analysis of cellular images in general, and RBC images in particular. Besides an unbiased classification, the application of CNNs yields an enormous gain in performance and inevitably forms the cornerstone in the development of cost-efficient point-of-care devices relying on image data and without pretreatment of biological specimens such as the application of biomarkers.

In contrast to conservative methods predominantly involving the human analysis of cellular compounds in stasis, the parameter space is enhanced by the dynamic properties of RBCs. Presumably, inherent features of the shape phase diagrams are linked to the health state due to the influence of elastic parameters and therefore need to be exploited for certain hematological diseases.



# Chapter 5

## Lingering dynamics of red blood cells in vivo

This chapter provides a profound quantitative analysis of the dynamics of lingering events in vivo. The results presented in the following have been published in reference [184].

### 5.1 Introduction

The microvascular network in the body of vertebrates is responsible for the nutrient and gas exchange towards the tissues and, due to its tremendous amount and size of individual vessels, is the largest dissipation site of cardiac energy [185]. Any alterations in the microvascular flow patterns lead to a deterioration of the physiological performance and are linked to many pathological states, including obesity [186] and cardiac ischemic disease [187, 188], among others.

Most macroscopic observables obeying a homogeneous distribution in the macrovasculature show spatial and temporal heterogeneity in microvascular networks. This hallmark of the microcirculation arises from the bi-phasic nature of blood. An example of this temporal heterogeneity is given in Fig. 5.1, where the temporal evolution of the hematocrit is depicted in a capillary of a living hamster. This influence on the dynamics of individual RBCs implies

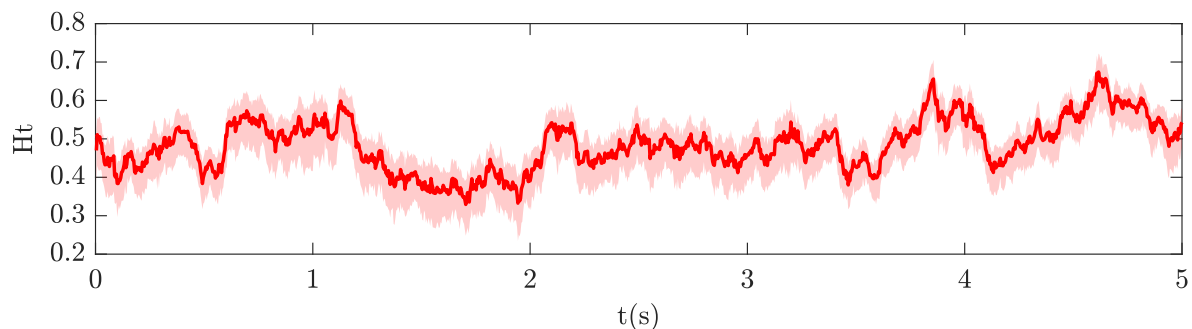


**Figure 5.1:** Measured hematocrit in the capillary of a living hamster. The red solid line corresponds to the calculated value, the shaded area indicates the error due to experimental restrictions. In contrast to a homogeneous hematocrit value in the macrovasculature, the hematocrit in the microvasculature is highly heterogeneous.

the need for fine-grained models to predict hemodynamic quantities reliably in silico. Due to this complex modeling, detailed knowledge of the dynamics on a cellular scale is sparse. However, over the past years, there has been significant progress in the modeling of the microvasculature. The topology of the employed microvascular architectures ranges from

symmetrical bifurcations [78, 189] to the mimicking of an anatomically exact in vivo network comprising an interconnected mesh-like structure with bifurcating and merging vessels [75, 190–192]. Balogh *et al.* [75] investigated such complex networks on a scale permitting, on the one hand, dense suspensions of RBCs, and on the other hand yields information about every individual RBC in the suspension. As a result of this fine-grained approach, they analyzed the temporal evolution of the deformation characteristics of RBCs in the vicinity of bifurcations. They particularly focused on so-called lingering events, the phenomenon of resting RBCs at the bifurcation apex of branching vessels, as illustrated in Fig. 5.2. Although this phenomenon is well known in physiology, no previously conducted studies addressed this subject in a qualitative or a quantitative manner.

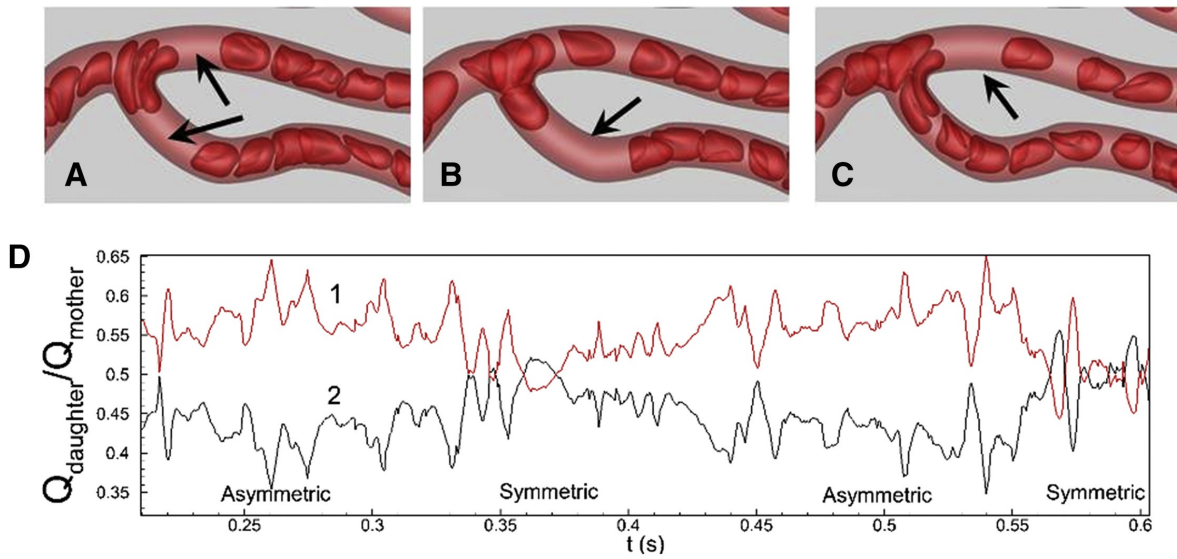


**Figure 5.2:** Overview of two different lingering scenarios. (A) Symmetric lingering in a branching vessel, leading to symmetric flow rates in both daughter vessels. (B, C) Asymmetric lingering in one of both daughter vessels yields an asymmetric partitioning of RBCs in both daughter vessels. Black arrows indicate the voids that emerge from the lingering RBCs further upstream. (D) Comparison of the flow rates for symmetric and asymmetric blockage of the daughter vessels caused by a lingering event. The respective flow rates in both daughter vessels are normalized by the flow rate in the mother vessel. Image adapted from reference [75].

Recent advances in intravital microscopy techniques improved the level of details for microvascular blood flow and thus enable to match the findings in silico. This chapter is dedicated to the fundamental dynamics of the aforementioned lingering events in vivo utilizing intravital fluorescence microscopy in hamsters. Therefore, we have developed algorithms allowing us to separate the effect of lingering on the flow of subsequent RBCs from non-lingering events. Our findings show the severe impact lingering RBCs have on the partitioning of RBCs downstream the bifurcation and the break-up of trains of RBCs.

We first give an introduction to the architecture and physical properties of microvascular beds and the blood flow therein. Subsequently, we describe the experimental setup, comprising the animal preparation as well as the microscopy setup and image acquisition. The following sections are intended to provide the detailed results of all analyzed geometries, whose implications are discussed in a subsequent section. A summary is provided at the very end of the chapter.

## 5.2 Architecture of microvascular beds

The microvasculature in the body of mammals is a complex plumbing network consisting of vessels with varying lengths and diameters. To ensure an optimal perfusion of tissues and organs with oxygen and a steady supply of metabolites, a convective motion of blood needs to be achieved. Whereas for unicellular living beings, this perfusion can be achieved solely by diffusive processes, active transport processes are necessary to reliably perfuse the body of pluricellular living beings. In the latter case, a pressure drop between the aorta and vena cava, i.e., the main feeding and the main draining vessel, respectively, is providing the active perfusion [185]. This pressure drop results from the synchronized contractions of cardiac muscles and the vasoconstriction of blood vessels, performed by vascular smooth muscles [193].

The entirety of arteries and veins is commonly referred to as macrocirculation, whereas all smaller vessels are referred to as microcirculation. An overview of typical sizes and mean speeds of the blood in various vessel types and different geometrical constraints are given in Tab. 1.1. In between the macrovascular vessels, the microcirculation is located, consisting of arterioles, capillaries, and venules. Since the diameters of these vessels are comparable to the equilibrium diameter of RBCs, the particulate nature of blood is well pronounced.

Given the overall length of the constituting vessels in combination with the dimensions of each individual vessel, the microvascular bed forms the largest hydrodynamic resistance and hence the largest dissipation site of cardiac energy [194–196]. The ability of the microvasculature and its constituent vessels to adapt to the systemic and local needs of the organism is crucial. To ensure this adaptation of the microvasculature, accommodations both on a long-term scale as well as on a short-term scale exist. Short-term adaptations comprise vasodilation and vasoconstriction, i.e., the increase and the decrease of the vessel diameters, respectively. On a long-term scale, a remodeling of parts of the microvascular network occurs, also termed angioadaptation.

### 5.2.1 Constituent vessels in the microcirculation and Murray's law

The inner cavity of healthy vessels, the lumen, is enclosed by a lining of endothelial cells. Attached towards the outside are smooth muscle fibers, whose layer thickness may vary considerably depending on the vessel type [197]. These muscle fibers are responsible for the contractile movements of the vessel walls, the vasoconstriction. In dilated vessels, the cross-sections have been found circular, whereas, in a contracted state, the cross-section can adopt irregular, star-like patterns. Regulatory mechanisms of vasoconstriction and vasodilation are manifold, and comprise e.g. neural [198], metabolic [199], and mechanic stimuli [200]. Among all vessel types in the microvascular bed, arterioles are responsible for most of the diameter changes, and thus for the largest pressure drop within the microvascular flow.

Murray assumed in his seminal work that universal optimality principles are governing any convectively driven transport network [201]. This optimality principle has been proved e.g. for the xylem of plants [202] and consists of the minimization of a cost function, equal to the sum of dissipated energy due to viscosity and the energy required to maintain the transported volume. One consequence of Murray's law is the cubic relationship between the lumen diameters of mother vessel and daughter vessels. Even though this decrease in radii of subsequent vessel generations could be proven to suffice Murray's law in some peculiar cases, deviations and also contrasting analyses on experimental data have been carried out. One major assumption

leading to this deviation is the constant wall shear stress, which in reality is correlated with blood pressure and thus decreases along the vessel segments [203].

Even though the connection of vessel diameters according to Murray's law cannot be confirmed in all investigated geometries, there have been numerous studies indicating a qualitative power-law behavior of connective vessel diameters. Implications arising from these findings are a fractal-like hierarchical geometry and self-similarity of microvascular beds [204]. The determinants of the final topology of microvascular beds are given by a complex interplay of apparently opposite demands. Whereas mesh-like geometries can provide uniform diffusion distances of oxygen towards the tissues, their hydrodynamic resistance is enlarged with respect to tree-like patterns. Depending on specialized needs of organs and tissues, the topology of microvascular beds can range from rather planar structures, as e.g. in the mesentery or the retina [205], respectively, to structures in the cardiac muscle, where capillaries extending throughout the entire tissue form three-dimensional networks [206]. Exemplary topological structures of the aforementioned cases are depicted in Fig. 5.3.

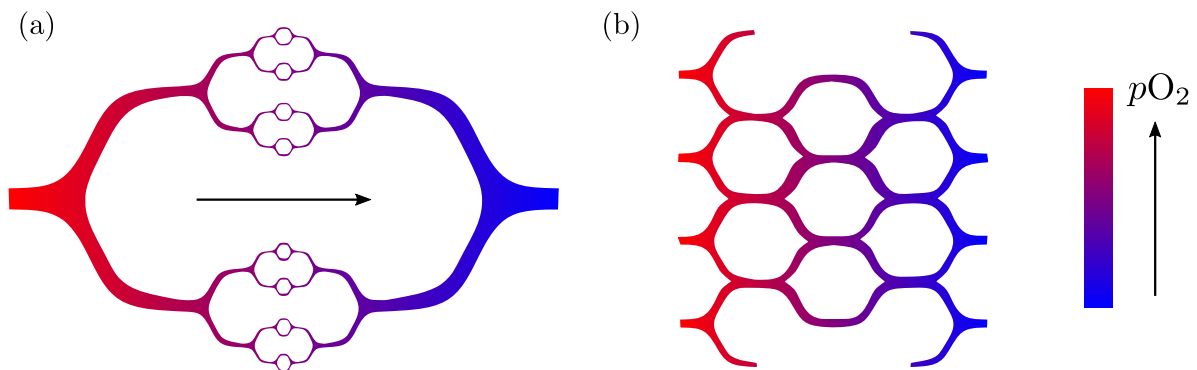


**Figure 5.3:** Sketch of two possible topologies of microvascular beds. In (a), a hierarchical structure is formed by the vessels, whereas in (b), an arcade-like topology is depicted. The blood flow is indicated by the arrow and delivering oxygen-rich blood (red) towards the arterioles. Venues carry carbon dioxide-rich blood (blue), i.e., oxygen-poor blood towards the veins.

## 5.2.2 Angiogenesis

While genetic factors determine the principal pattern and arrangement of vessels in the human body, the development of microvascular beds is governed by random sprouting and the regression of vessels [207]. This stochastic process tends to oversaturate tissues with vessels; however, due to pruning mechanisms, a functionalized microvascular bed is established. This creation of new vessels, or angiogenesis, is altered by factors such as pregnancy [208], sports [209, 210], and wound healing [211]. If the oxygen supply of tissue regions is insufficient, metabolic substances such as the vascular endothelial growth factor (VEGF) are generated, triggering angiogenesis. However, in several pathological states, angiogenic protein concentrations are altered, leading to non-functional microvascular networks, e.g. in tumor growth [212]. Therefore, the investigation of angiogenesis has become an important diagnostic tool. The abnormal states range from poor vascularization to oversaturated beds, and even the intrinsic topology varies. These intrinsic variations e.g. comprise the formation of shunts, i.e. bypassing vessels interconnecting two distinct branches. Besides the metabolically driven

angiogenesis, there is evidence that mechanical stimuli, such as an increased wall shear stress acting on the endothelial layer of capillaries, trigger the formation of new vessels as well [213], which highlights the importance of a detailed understanding of dynamics on a cellular scale in microvascular networks.

## 5.3 Experimental setup for in vivo measurements

*The animal preparation, as well as the recording of the in vivo blood flow, have been carried out at the Institute for Clinical and Experimental Surgery situated at the Saarland University Hospital. All the conducted experiments were approved by the local government animal protection committee (permission number: 25/2018) and were performed in accordance with the German Legislation on the Protection of Animals and the NIH Guidelines for the Care and Use of Laboratory Animals.*

To investigate the capillary blood flow in the hamster models, two different objectives are used. On the one hand, a water immersion objective is used (Plan-Apochromat 63 $\times$ , Zeiss), yielding an improved RBC tracking and analysis of individual RBC characteristics, e.g. the evolution of the deformation while advecting through bifurcation sites and merging vessels. As a drawback, this objective is restricted to shallow tissue layers due to the optimal working distance. On the other hand, an air objective (Plan-Apochromat 50 $\times$ , Zeiss), equipped with a relatively increased working distance and an enlarged field of view is employed to capture the blood flow in vessels of bigger dimensions or embedded in deeper tissue layers. The footage is recorded as single video files, which are split into image series, containing up to 6,000 single images each. The exact amount of single images being extracted depends on the frame rate of the camera (ORCA-Flash4.0 V3, Hamamatsu) and the recorded time interval, generally covering 4 s – 20 s.

### 5.3.1 Animal preparation

Although a variety of imaging techniques in clinical diagnostics are established, only a few work on a cellular scale and are easy to implement. To gain insights into the microvasculature of macroscopical living beings such as mammals, one subtle tool has been used predominantly over the last decades. Originally designed to study angiogenesis and the biocompatibility of implanted engineered tissues with the host tissue of the animal, the dorsal skinfold chamber provides detailed knowledge of flowing RBCs in vivo [214].

In this section, the necessary steps in the animal preparation protocol are summarized briefly. These descriptive steps are based on reference [215], where a profound explanation is given. A dorsal skinfold chamber, consisting of two symmetrical titanium frames with a total mass of approx. 4 g is implanted in the back of Syrian golden hamsters (*Mesocricetus auratus*) with a body mass of 60 g – 80 g, as depicted in Fig. 5.4. For this purpose, the animals are anesthetized and from their depilated and disinfected back, the outer skin layer is disconnected generously from deeper skin layers. Subsequent layers consisting of the subcutis and the panniculus carnosus muscle and both layers of the retractor muscle are entirely removed within the circular observation window of the skinfold chamber (cf. Fig. 5.4). After the chamber has been implanted, the animal is allowed to recover for at least two days from the surgical trauma to ensure physiological conditions in the blood circulation. In order to avoid any interindividual



**Figure 5.4:** Syrian golden hamster equipped with dorsal skinfold chamber. In the upper center of the titanium frame, the circular observation window is located, containing visible blood vessels of the microvasculature.

effects and also to focus on different phenomena in various microvascular geometries, a total number of five hamsters were analyzed. Besides hamsters, also other rodents such as rats and mice are common models to study biomaterials in the dorsal skinfold chamber, however, due to anatomic reasons, the signal-to-noise ratio has proven to be the best in hamsters.

Prior to fixing the hamster on the microscopy stage, the animal is anesthetized by an intraperitoneal injection of  $100 \text{ mg kg}^{-1}$  ketamine and  $10 \text{ mg kg}^{-1}$  xylazine. Additionally,  $0.1 \text{ ml}$  of 5% fluorescein isothiocyanate (FITC)-labeled dextran (150 kDa, Sigma-Aldrich) is injected into the retrobulbar venous plexus to stain the blood plasma. Eventually, the animal is fixed onto the microscopy stage of an upright microscope, allowing for lateral positioning of the desired field of view, as described in reference [216].

## 5.4 Image analysis and data acquisition

### 5.4.1 Image processing

To reliably detect RBCs in the microvasculature and to ensure uniform image quality, the recorded image files have to be post-processed. In the first step, every image series has been cropped to the desired geometry. This cropping results in faster image processing by subsequent algorithms but also helps to avoid unnecessarily big data structures. However, a proper adjustment of the cropping region is crucial since all feeding and draining vessels, respectively, of the analyzed geometry should remain in the final images. We then apply a correction for lateral shifts caused by abundant breathing movements of the animal by crosscorrelation of subsequent images. However, also shifts perpendicular to the focal plane occur, resulting in defocusing of a subset of images. In this case, the image series is split up into subseries of images where no defocusing of the vessels exists. We stress that, due to vessels exploiting a complex three-dimensional topology, not all segments are necessarily in focus and we restrict our analysis only to those segments that are in focus.

Due to the staining of the plasma, as described in section 5.3.1, in combination with the heterogeneous distribution of cells (cf. section 5.1), the concentration of fluorescent dye is highly time-dependent. This time-dependent distribution of dye leads to flickering in the raw footage

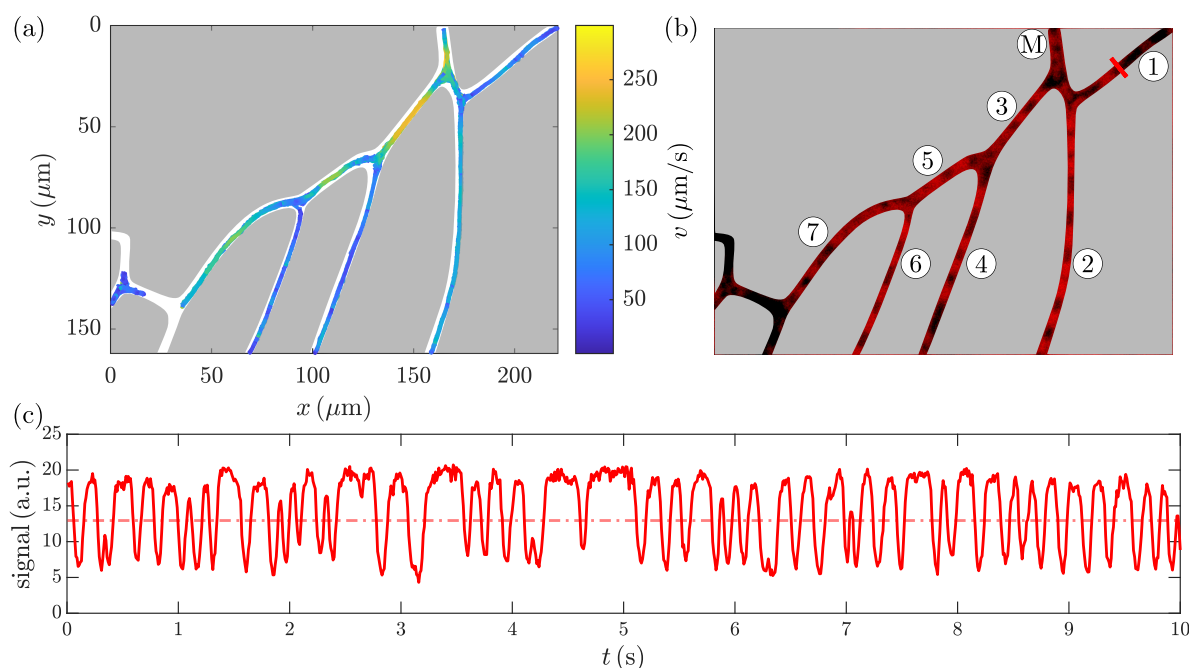


**Figure 5.5:** (a) Results of RBC tracking in the specified geometry. The feeding, or mother vessel (“M” in figure (b)) in the top right part delivers the blood flow, which then exits in the draining or daughter branches. The color bar indicates the magnitude of the tracked velocities. A ubiquitous subset of 500 tracks is drawn in the masked geometry. (b) Snapshot of the geometry with flowing RBCs (red) in false color representation to enhance the visibility. From the top right to the bottom left the daughter branches are labeled numerically in ascending order. (c) Distribution of voids and RBCs within a distinct branch (1) of a bifurcation. The graph indicates the integrated intensity along a line segment perpendicular to the flow direction (red line segment in the branch (1) in (b)). The mean value (red dash-dotted line) serves as a threshold to discriminate voids from RBCs. The void durations are then defined as the time interval of consecutive intensity values above this threshold, whereas advection times of RBCs are specified by the time interval of consecutive intensity values below the mean value. Voids have an average duration of ca 100 ms however, due to partial blockage of vessels caused by lingering RBCs, voids exceeding multiple times the average void duration are formed. The formation of such a long void with a duration of 350 ms manifests at  $t \approx 4.7$  s. Image adapted from reference [184].

since the white balance of the camera is adapted automatically during the image acquisition. If not corrected for this flickering, the evaluation of intensity signals will be impaired. To achieve a uniform white balance throughout the recorded images, a histogram matching algorithm has been applied. This step is crucial since for the data analysis, the integrated signal for a line of pixels, and thus, the brightness is calculated to discriminate void areas from RBCs. To despeckle and smooth the images, a Gaussian blur is applied. Afterwards, the image series is convoluted with a manually obtained binary mask. This operation ensures a contrast enhancement of the images by disregarding the background with the associated noise, caused e.g. by staining artifacts. To obtain these masks, a subset of the images is averaged. Eventually, the traced resulting image yields the vessel geometry. However, the diameter of the vessels in the respective masks is larger than their real diameter. In Fig. (5.5), an exemplary mask is depicted alongside the original underlying *in vivo* geometry. A custom-tailored MATLAB<sup>®</sup> script is adapted to perform a particle tracking out of the im-

age series. These adaptations comprise specific corrections for the binarization threshold and classification filters for the detected objects regarding the size and contour and are generally based on the identical script as described in section 2.4.2. Due to heterogeneous tissue thickness and the fact that the vessels are exploiting a three-dimensional topology, the focal plane will only be adjusted correctly for a certain part of the geometry within the field of view. Thus, an entirely automatized analysis of all datasets is merely impossible except for some peculiar cases. Consequently, manual adjustments are necessary to reliably track the flowing RBCs in all scenarios.

The staining agent yields a fluorescent plasma staining, implying that advecting RBCs yield lower intensity signals than the surrounding plasma-rich zones, i.e., advecting voids. Based on this observation we, therefore, define the occurrence of voids and RBCs from the corresponding temporal intensity or brightness distributions. To guarantee an unbiased and uniform identification of the aforementioned events, we binarize the integrated intensity signal with respect to the arithmetic mean. In conjunction with the previous considerations, intensity values above the respective mean value are thus defined as voids, whereas intensity values below the threshold are considered as traversing RBCs. Yet, due to the variation of the flow velocities in the respective vessels, the absolute void durations are an inadequate measure to characterize the effect of lingering. Instead, we determine the mean advection time of RBCs in each vessel and denote this value by  $\tau_{\text{RBC}}$ . The rescaled void durations are then given by  $\tau_{\text{RBC}}$ , corresponding to normalization by the flow rate.

### 5.4.2 Parameter estimation using the maximum-likelihood approach

These normalized void durations  $\tau/\tau_{\text{RBC}}$  are then sorted in ascending order to obtain the empirical cumulative distribution function  $\text{ecdf}(\tau_n/\tau_{\text{RBC}})$ . Since the values of the normalized void durations are strictly non-negative, independent random variables, we assume that their cumulative distribution function  $\text{cdf}(\tau_n/\tau_{\text{RBC}})$  is represented by a log-normal distribution function. In addition, we observe a high variance in the data along with low means of void durations, which additionally leads to the assumption of a log-normal distribution [217]. The likelihood function  $\mathcal{L}(\mu, \sigma|X)$  of the log-normal distribution for a series of  $N$  independent observables  $x_n, n \in \{1, \dots, N\}, \mu \in \mathbb{R}, \sigma \in \mathbb{R}^+$  is given as the product of all individual probability density functions of each  $x_n$ ,

$$\begin{aligned} \mathcal{L}(\mu, \sigma|x_n) &= \prod_{n=1}^N f(x_n|\mu, \sigma) \\ &= (2\pi\sigma^2)^{-N/2} \prod_{n=1}^N \left( x_n^{-1} \exp \left[ -\frac{(\log(x_n) - \mu)^2}{2\sigma^2} \right] \right). \end{aligned} \quad (5.1)$$

To find the parameters maximizing the likelihood function, we take the derivative of Eq. (5.1) with respect to  $\mu$ ,

$$\frac{\partial \mathcal{L}}{\partial \mu} = (2\pi\sigma^2)^{-N/2} \prod_{n=1}^N \left( x_n^{-1} \exp \left[ -\frac{(\log(x_n) - \mu)^2}{2\sigma^2} \right] \right) \cdot \left( \sum_{k=1}^N \frac{(\log(x_k) - \mu)}{\sigma^2} \right). \quad (5.2)$$

Eq. (5.2) can only vanish if

$$\begin{aligned} 0 &= \sum_{k=1}^N \frac{(\log(x_k) - \mu)}{\sigma^2} \\ \Leftrightarrow \mu &= \frac{1}{N} \sum_{k=1}^N \log(x_k). \end{aligned} \quad (5.3)$$

Similarly, we find by derivation of Eq. (5.1) with respect to  $\sigma$  and equating it to zero,

$$\sigma^2 = \frac{1}{N} \sum_{k=1}^N (\log(x_k) - \mu)^2. \quad (5.4)$$

To prove that Eqs. (5.3) and (5.4) indeed maximize the likelihood function Eq. (5.1), one can show that the corresponding Hessian is negative definite, and thus indicates a local maximum. Moreover, one finds  $\lim_{\mu \rightarrow \pm\infty} \mathcal{L}(\mu, \sigma | x_n) = -\infty$ , and  $\lim_{\sigma \rightarrow 0, \infty} \mathcal{L}(\mu, \sigma | x_n) = -\infty$ , and hence Eqs. (5.3) and (5.4) indicate a global maximum.

The cumulative distribution function of the normalized void durations then reads

$$\text{cdf} \left( \frac{\tau_n}{\tau_{\text{RBC}}} \right) = \frac{1}{2} \left[ 1 + \text{erf} \left( \frac{\log \left( \frac{\tau_n}{\tau_{\text{RBC}}} \right) - \hat{\mu}}{\sqrt{2}\hat{\sigma}} \right) \right], \quad (5.5)$$

with the error function  $\text{erf}(\cdot)$ . Here, the standard notation for the parameters  $\hat{\mu}$ , and  $\hat{\sigma}$  is used to indicate that they originate from estimation, with

$$\begin{aligned} \hat{\mu} &= \frac{1}{N} \sum_{n=1}^N \log \left( \frac{\tau_n}{\tau_{\text{RBC}}} \right), \\ \hat{\sigma}^2 &= \frac{1}{N} \sum_{n=1}^N \left( \log \left( \frac{\tau_n}{\tau_{\text{RBC}}} \right) - \hat{\mu} \right)^2. \end{aligned} \quad (5.6)$$

Differentiating the cumulative distribution function in Eq. (5.5), we obtain the associated probability density distribution of the constituting normalized void durations. The a priori postulation of the void durations being log-normally distributed is verified a posteriori by a Kolmogorov-Smirnov (KS) test. This test evaluates the supremum of all individual differences from the empirical cumulative distribution function and the cumulative distribution function based on the estimated parameters:

$$s = \|\text{cdf}(\tau_n/\tau_{\text{RBC}}) - \text{ecdf}(\tau_n/\tau_{\text{RBC}})\|_{\text{sup}}. \quad (5.7)$$

## 5.5 Results

We analyze the flow of RBCs in the vicinity of bifurcating vessels with varying diameter and bifurcating angles. Analogous to recent observations *in silico*, we find lingering events, i.e., RBCs resting at the bifurcation apex. Such a lingering RBC in an arteriolar bifurcation is depicted in Fig. 5.6 at different timesteps. From the conducted experiments, we obtain various

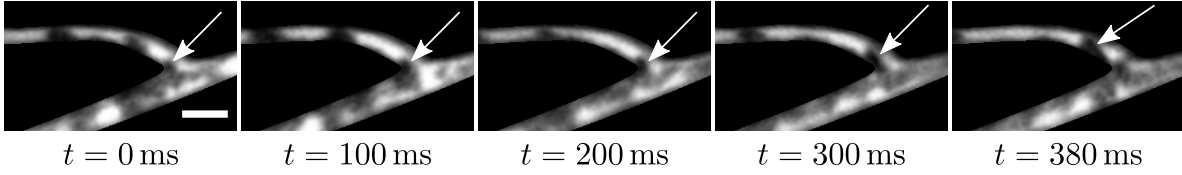


**Figure 5.6:** Snapshots of a lingering RBC at an arterial bifurcation for a time interval of  $t = 380$  ms. At  $t = 0$  ms, an RBC is touching the apex of the bifurcation. Subsequently, the RBC starts to deform and linger around this apex, leading to a partial blockage with decreased flow rate as can be seen in the upper daughter vessel for the entire image series. At  $t = 380$  ms, the cell is detaching from the apex. The white arrows are pointing towards the lingering RBC. The scale bar is  $10 \mu\text{m}$  in width. Image adapted from reference [184].

unique branching geometries which are analyzed in section 5.5.3. Yet, to describe the entire procedure of the analysis in detail, we restrict this section in the following to the most complex vessel topology with a total number of four bifurcation apices and seven interconnected daughter vessels, organized hierarchically.

Based on the geometry depicted in Fig. 5.5, we obtain the integrated intensity signal along a perpendicular line with respect to the flow direction. This method yields information about the general distribution of RBCs and cell-depleted areas; however, no information about lingering is yet taken into account. We rather implement this technique since the particle tracking results do not yield trajectories that do not cover a sufficiently large distance due to the fact that not all parts of the recorded vessel geometry are in focus. The bifurcation apex is in the focal plane for all the discussed geometries and hence the particle-tracking algorithm can be applied to this region. We thus combine the results of both implemented techniques to provide a holistic view on the lingering of RBCs and their dynamics.

According to the detailed remarks in section 2.4.2, we obtain trajectories of individual RBCs, whereas, in contrast to the parameter settings for the in vitro experiments, we do not neglect trains of cells for the current in vivo experiments. From the precise individual position data of flowing RBCs, we calculate the RBC velocities for each frame. Specifically, we focused on the velocities in a small circular region around each bifurcation apex due to the definition of a lingering event in silico as an RBC resting at the bifurcation apex. Due to peculiarities of intravital microscopical imaging and the resulting image noise level, the center of mass of the detected RBC is fluctuating slightly in consecutive images. We, therefore, adjust the definition of a lingering event as in reference [75] to a specific threshold of  $v_{\text{RBC}} < 30 \mu\text{m s}^{-1}$ , such that RBCs in the specified annulus around the apex displaying a velocity below this value are classified as lingering cells. The threshold value is determined heuristically by the precision of the tracked center of mass of resting RBCs in the current setup, which is approx.  $200 \text{ nm} - 300 \text{ nm}$  due to minor lateral shifts resulting from breathing movements and alterations in the illumination. Together with the time interval between consecutive images of approx.  $10 \text{ ms}$ , the velocity profile exhibits a minimal value of  $v_{\text{RBC}} \simeq 20 \mu\text{m s}^{-1} - 30 \mu\text{m s}^{-1}$  for resting RBCs. We remark that this threshold value is significantly lower than typical velocity regimes in the microvasculature (cf. Tab. 1.1) and that this adaptation is not contradictory to the original definition but solely due to intrinsic experimental limitations.

### 5.5.1 Void durations: The impact of lingering

Since vessels are exploiting a three-dimensional topology, not all parts of a given geometry are in the focal plane. To account for this circumstance, we intentionally evaluate the integrated brightness signals at vessel segments in focus. The resulting spatio-temporal shift of the lingering RBC and the instantaneous impact on the flow field thereof at the position of the signal evaluation downstream is corrected for by the average RBC velocity in the intermediate vessel segment. In fact, this approach enables us to relate the influence of lingering events on void formation at arbitrary suited positions in the branching vessels.

Using the maximum-likelihood approach, we first estimated the parameters of our empirical cumulative distribution of void durations, as described in section 5.4.2. Here, all void durations are taken into account, i.e., independent if they are associated with lingering events or not. In Fig. 5.7, the good agreement between the analytical distribution function and the data is shown, as one can see by the deviations of datapoints and analytical curves. Additionally, we perform the Kolmogorov-Smirnov test as an indica-

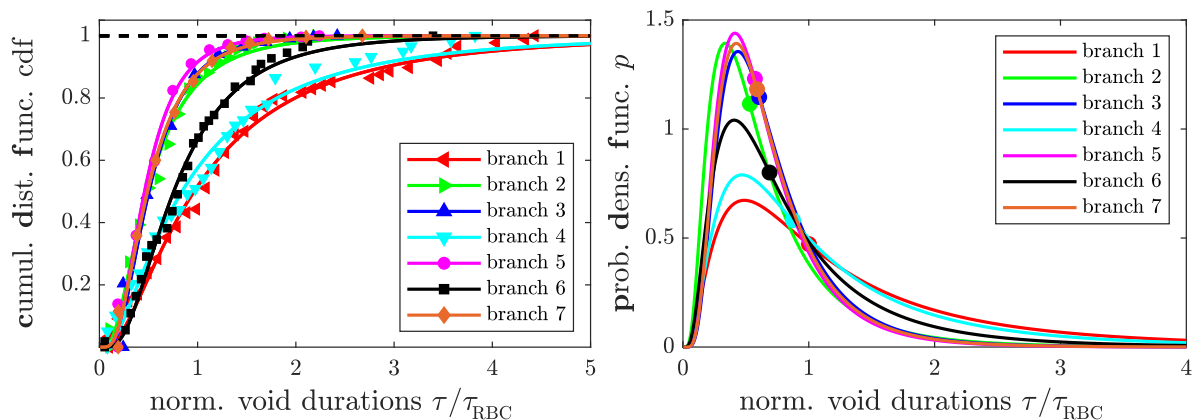


**Figure 5.7:** (left) Cumulative distribution functions of normalized void durations  $\tau/\tau_{\text{RBC}}$  for all branches of the geometry in Fig. 5.5. The temporal length of the voids is hereby rescaled for each branch by the average time of a RBC to pass,  $\tau_{\text{RBC}}$ . The data points correspond to measured void durations, whereas the solid line corresponds to the respective analytical log-normal distributions with estimated parameters  $\hat{\mu}$  and  $\hat{\sigma}$ , as in Eq. (5.5). (right) Probability density functions of all measured void durations for each branch of the analyzed geometry, normalized by the passage time of RBCs. The individual graphs are given by derivation of the corresponding cumulative distribution function. Image adapted from reference [184].

tor to verify the assumption of log-normally distributed void durations. We find that  $s_i = \{0.11, 0.10, 0.07, 0.07, 0.09, 0.08, 0.06\}$ ,  $i \in \{1, \dots, 7\}$ , where  $i$  denotes the branch identifier according to Fig. 5.5.

Due to this very good agreement between the predicted analytical distribution function and the empirical distribution function, the log-normal distribution of void durations is justified a posteriori. All other analyzed geometries confirm this assumption due to similar results of the KS test. In all cases we find  $s < 0.13$ . The corresponding probability density functions of all void durations are furthermore provided alongside the cumulative distribution function in Fig. 5.7. Filtering the whole dataset of voids by the events of lingering RBCs at the preceding bifurcation apex, we obtain the cumulative distribution functions and the probability density functions, similarly to the previous considerations. However, we restrict all further analysis to these probability density functions. The result of the separation of

lingering and non-lingering events, respectively, is shown in Fig. 5.8. Whereas the left graph

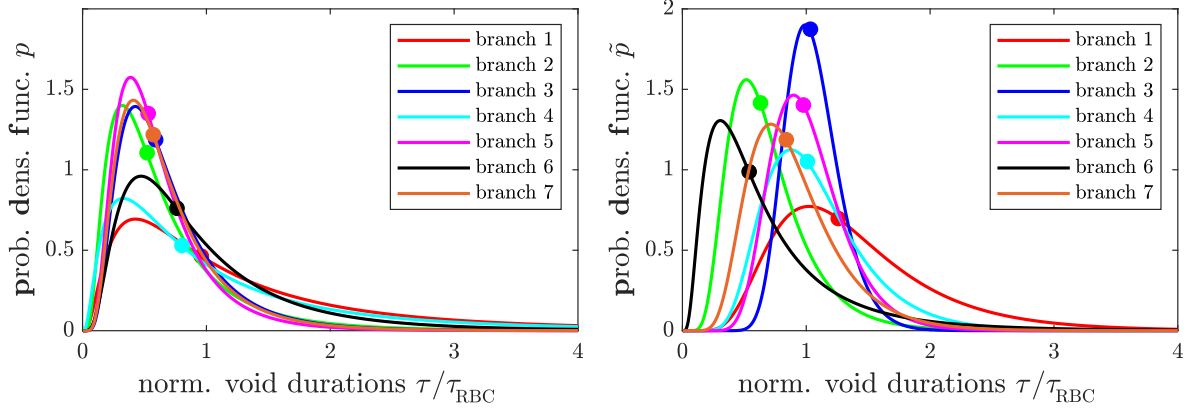


**Figure 5.8:** (left) Probability density functions of void durations for all branches as in Fig. 5.7 in the case of non-lingering events. The temporal length of the voids is scaled for each branch by the average time of a RBC to pass,  $\tau_{\text{RBC}}$ . (right) Probability density functions of normalized void durations exclusively associated to lingering events for all branches. We define a lingering event to occur if the speed of an RBC is lower than  $v_{\text{RBC}} \leq 30 \mu\text{m s}^{-1}$  in the vicinity of a bifurcation apex. The numerical ordering of the labels is identical to the one in Fig. 5.7. Filled circles in matching colors indicate median values of normalized void durations, obtained from estimated parameters as in Eq. (5.6). Image adapted from reference [184].

in Fig. 5.8 depicts the void durations associated to non-lingering events, the right graph shows the distribution of void durations exclusively associated to lingering RBCs. In the former case, the median void durations are narrowly distributed, contrasting the observation in the latter case, where the median values are shifted towards higher void durations for all daughter vessels except for branch 6. Additionally we notice a suppression of short void durations  $\tau/\tau_{\text{RBC}} < 0.5$  in the case of lingering associated voids, which in turn contributes to the mentioned median shift. We therefore quantify the probabilities to obtain void durations of less than  $0.5 \tau_{\text{RBC}}$ . In the case of non-lingering, numerical integration of the respective probability densities yields the probabilities  $P_i(\tau_{\text{void}} < 0.5 \tau_{\text{RBC}}) = \{0.23, 0.47, 0.38, 0.31, 0.45, 0.27, 0.40\}$ ,  $i \in \{1, \dots, 7\}$ , where  $i$  denotes the branch identifier according to Fig. 5.5. Similarly, we obtain  $\tilde{P}_i(\tau_{\text{void}} < 0.5 \tau_{\text{RBC}}) = \{0.02, 0.30, 0.00, 0.03, 0.01, 0.46, 0.10\}$ ,  $i \in \{1, \dots, 7\}$  with the probabilities  $\tilde{P}_i$  in the case of lingering. From these considerations, the drastic diminution of void durations of less than or equal to  $0.5 \tau_{\text{RBC}}$  in all cases except for  $i = 6$  is evident. Similar results are obtained for the additional vessel geometries, which will be presented in section 5.5.3.

### 5.5.2 Lingering frequency

Apart from the impact of individual lingering events on the overall RBC distribution in the network, we seek to quantify the number of voids in a distinct daughter branch associated with lingering events and the total number of voids in that branch. This so-called lingering frequency, denoted by  $n_{\text{linger}}$ , is depicted in Fig. 5.9 for the entire set of suitable geometries presented in section 5.5.3. We evaluate these lingering frequencies in relation to the respective normalized mean flow rates in the daughter branches of adjacent vessels. Due to the incompressibility of the fluid, the mean flow rate of the feeding vessel equals the sum of the flow

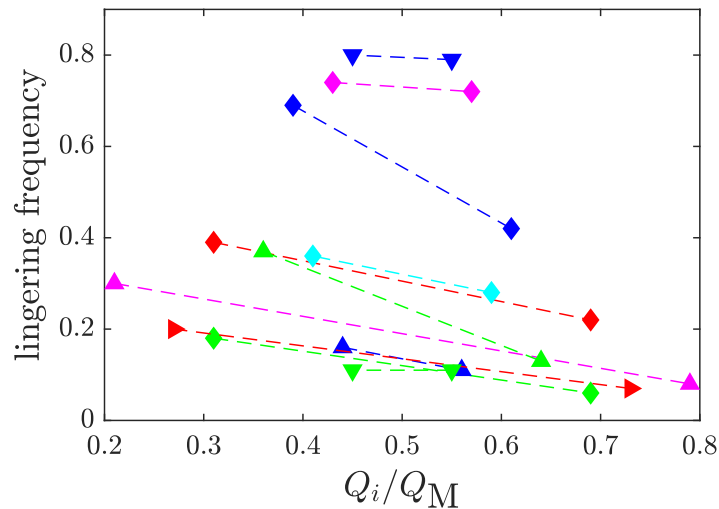


**Figure 5.9:** Lingering frequencies of the detected voids in relation to the normalized mean flow rate in a distinct vessel. The lingering frequency is defined as the fraction of the void count associated with a lingering event and the total void count in the vessel. Moreover, we define the normalized mean flow rate as a fraction of the flow rate in a daughter vessel  $Q_i, i \in \{1, 2\}$ , and the mother vessel  $Q_M$ . Identical color codes belong to pairs of vessels branching from the same apex; the dashed lines connect the data points of vessels. Image adapted from reference [184].

rates of all draining vessels within one generation of a hierarchical bifurcation cascade. Hence, the suitable geometries comprise the subset where the normalization factor of the flow rates is accessible. Since the apparent vessel diameters are smaller than the equilibrium size of RBCs, they are highly deformed while advecting through them. We therefore conjecture that their mean velocity may serve as a good approximation of the mean velocity of the plasma phase, the so-called plug flow. Hence, the time-averaged flow rate  $Q$  simplifies to

$$Q = \frac{\Delta V}{\Delta t} = A v_{\text{fluid}} \simeq A \frac{l_{\text{RBC}}}{\tau_{\text{RBC}}}, \quad (5.8)$$

with the finite volume element  $\Delta V$  advecting in the time interval  $\Delta t$ , the cross-sectional area  $A$ , the mean velocity of the plasma  $v_{\text{fluid}}$ , the length of the major axis of the circumscribing ellipse of RBCs  $l_{\text{RBC}}$  and the average RBC advection time  $\tau_{\text{RBC}}$ , as introduced in the previous paragraphs. The presented data in Fig. 5.9 shows a clear qualitative trend that among adjacent daughter vessels, the lingering frequency is relatively increased in the vessel exhibiting the lower flow rate.

Lastly, we remark that the analysis of void durations is not obvious in the context of blood flow in general and especially in microvascular networks. Admittedly, a more intuitive observable in the field of hemodynamics is given by the hematocrit. However, since we do have access to microscopic observables such as the individual RBC and void distributions throughout the network, a subtle investigation of intercellular distances provides a fine-grained picture of the influence of lingering, in contrast to the mesoscopic hematocrit picture. Nevertheless, the tube hematocrit in a vessel segment  $H_T$  is accessible via the mapping

$$H_T = \frac{V_{\text{RBC}}}{V_{\text{RBC}} + V_{\text{void}}} = \frac{1}{1 + \frac{\tau}{\tau_{\text{RBC}}}}, \quad (5.9)$$

with the volume fractions  $V_{\text{RBC}}$  of RBCs and  $V_{\text{void}}$  of voids, respectively.

In the derivation of the above expression, we explicitly used the assumption of plug flow, as denoted in Eq. (5.8). Via Taylor expansion, the obtained expression for  $H_{\text{T}}$  can be approximated as  $H_{\text{T}} \approx 1 - \frac{\tau}{\tau_{\text{RBC}}}$  in the case of short void durations  $\tau < \tau_{\text{RBC}}$ , and  $H_{\text{T}} \approx \frac{\tau_{\text{RBC}}}{\tau}$  for  $\tau > \tau_{\text{RBC}}$ , respectively.

### 5.5.3 Additional bifurcation geometries

Besides statistical reasons to cover further geometrical and topological varieties, additional analyses on various geometries in the hamster models have been conducted to neglect any effects originating from individual pathological particularities of the animal. The probability density functions along with the binarized mask indicating the geometry are depicted in the following figures in this section. The findings for the void durations corroborate the precedent findings qualitatively in most cases. Namely, the suppression of short void durations as well as the median increase of the void durations. In Figs. 5.10-5.14, we find for the majority of scenarios a qualitative coincidence to the previous analysis of the void durations in section 5.5.1. However, we also find the contrasting state, and geometries where only one vessel is suited for the analysis of voids.

Ideally, both bifurcating vessels are suitable for the application of our algorithm. Nevertheless, exceptions are given mainly due to the fact that one vessel is not in focus, resulting in an unreliable signal evaluation. Second, in some peculiar cases, the diameter of one daughter vessel is in a range that no file-like movement of RBCs is any longer present but rather a bulk flow of cells, making them indistinguishable in the available optical resolution limit. Examples of this circumstance are given in Fig. 5.10 (b, d), Fig. 5.12 (d), and Fig. 5.14 (b, d), where only temporal void distributions of a subset of bifurcating vessels are given. In these cases, the normalized flow rates cannot be established, since the normalization factor is inaccessible.

Among all investigated geometries, only the one depicted in Fig. 5.12 (e) does not obey any lingering events. Similarly, the geometry shown in Fig. 5.14 (c) exhibits only two lingering events and thus, no probability density functions are presented. Detailed descriptions will be given in the respective figure captions for all scenarios. In general, we restrict the abscissa to a limit of  $\tau/\tau_{\text{RBC}} = 4$ , since we are interested especially in the regions of short void durations in the order of the cell passage time and further, the probability densities for longer void durations are significantly low. Only in rare cases where long tails of the probability density functions arise, we restrict the abscissa to values up to  $\tau/\tau_{\text{RBC}} = 5$ .

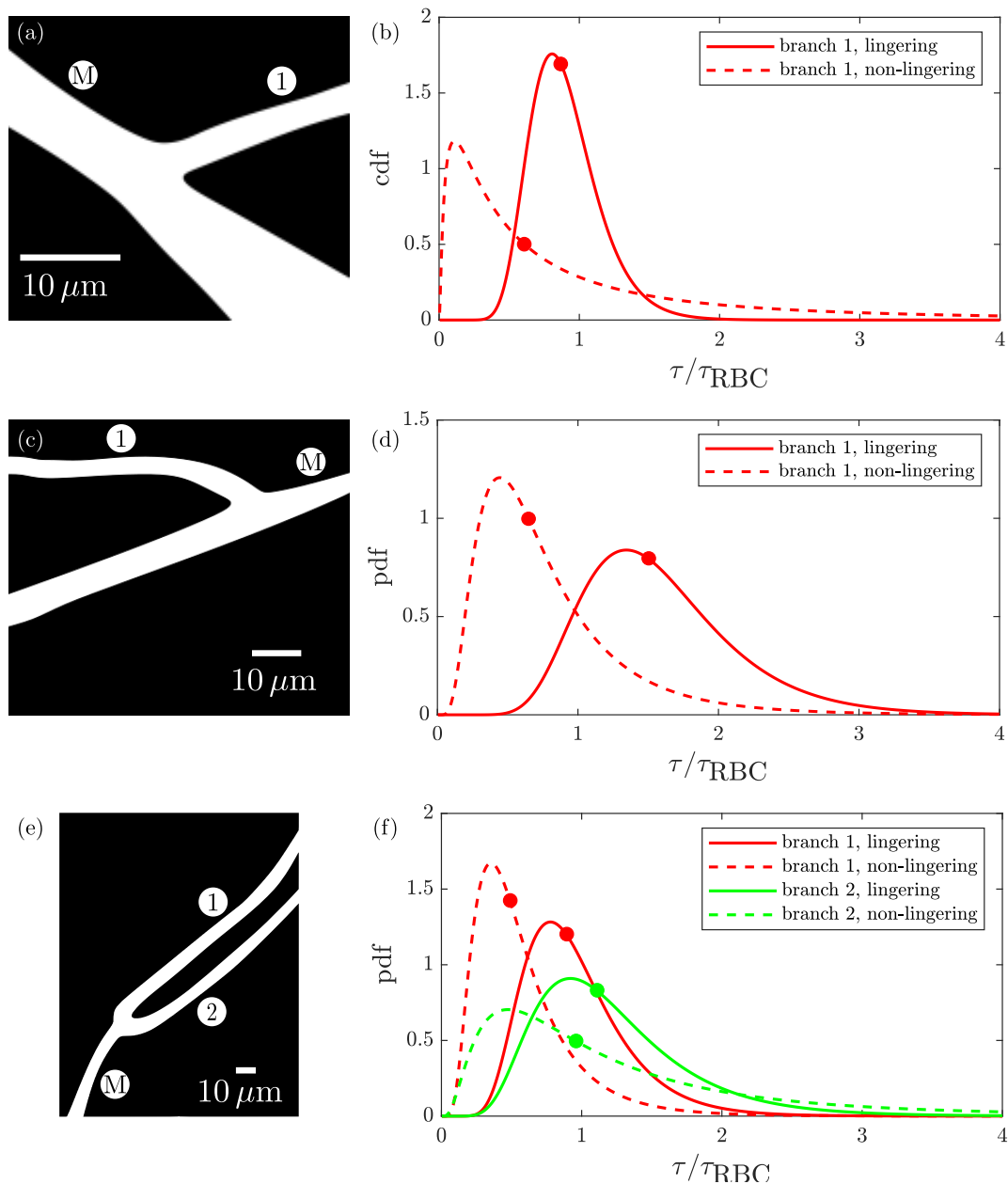


**Figure 5.10:** (a, c, e) Three different sections of the microvascular network are depicted. The blood flow in each geometry is coming from the mother vessel (M) and exits in the numerically labeled daughter branches. For a better visualization, only the binarized mask of each geometry is depicted. (b, d, f) Probability densities of the corresponding geometry on the left panel in the case of lingering-associated void formations (solid lines) and non-lingering associated voids (dashed lines). The abscissa values of the filled circles in the graphs depict the median void durations. With the notation as in section 5.5.1, we find for the dimensions and the probabilities  $P$ , and  $\tilde{P}$ : (b)  $P_1(\tau < 0.5 \tau_{\text{RBC}}) = 0.44$ ,  $\tilde{P}_1(\tau < 0.5 \tau_{\text{RBC}}) = 0.02$ ,  $n_{1,\text{linger}} = 0.13$ , and  $d_1 = 2.9 \mu\text{m}$  at the position of the intensity signal evaluation. (d)  $P_1(\tau < 0.5 \tau_{\text{RBC}}) = 0.33$ ,  $\tilde{P}_1(\tau < 0.5 \tau_{\text{RBC}}) = 0.00$ ,  $d_1 = 2.8 \mu\text{m}$ , (e)  $P_{1,2}(\tau < 0.5 \tau_{\text{RBC}}) = \{0.51, 0.22\}$ ,  $\tilde{P}_{1,2}(\tau < 0.5 \tau_{\text{RBC}}) = \{0.06, 0.03\}$ , the vessel diameters yield  $d_{1,2} = \{4.1, 3.5\} \mu\text{m}$ , with corresponding normalized flow rates  $q_{1,2} = Q_{1,2}/Q_M = \{0.73, 0.27\}$ , and lingering frequencies  $n_{1,2,\text{linger}} = \{0.07, 0.20\}$ . This geometry is linked to the unique identifier “ $\blacktriangleright$ ” in Fig. 5.9. Image adapted from reference [184].

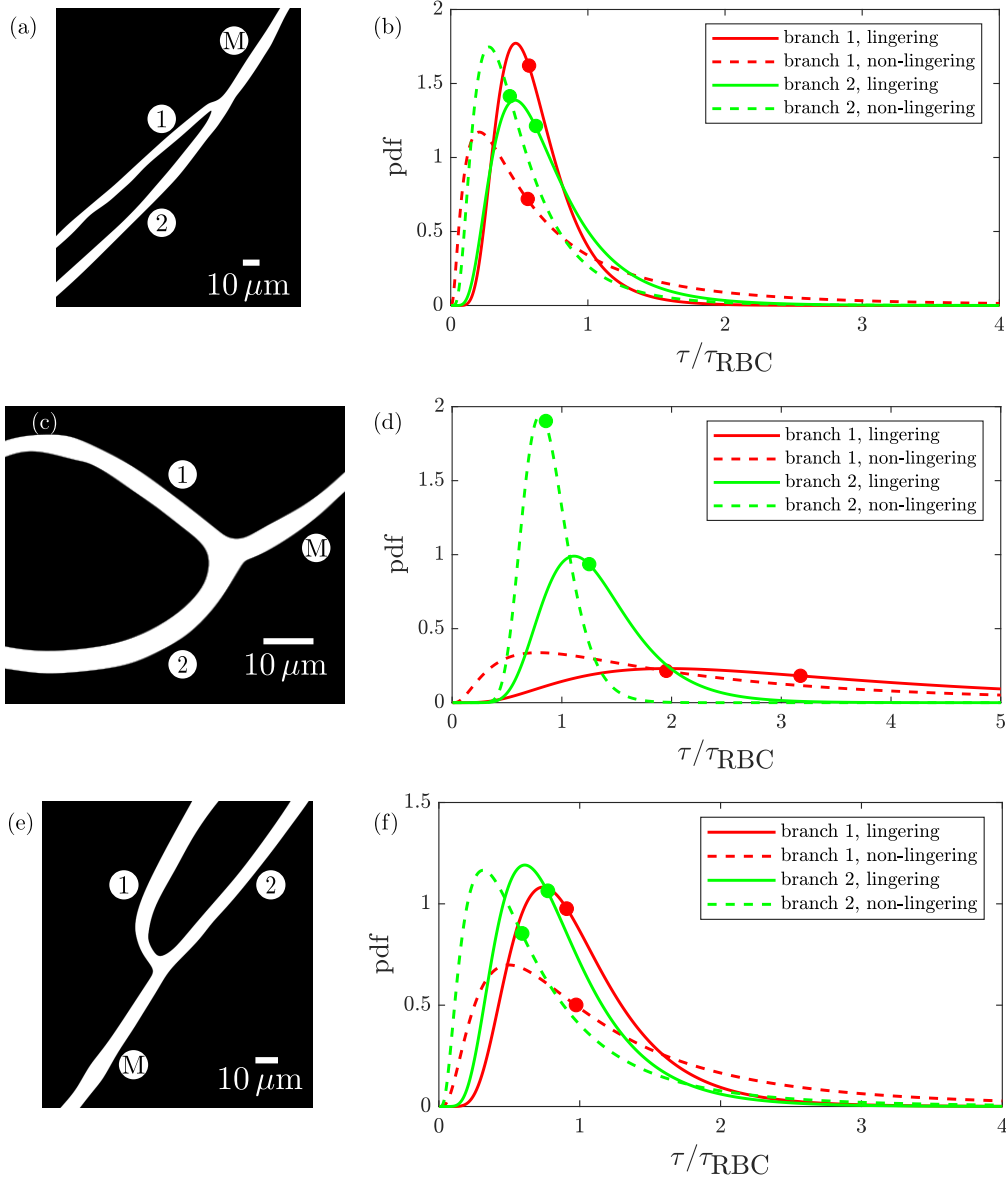


**Figure 5.11:** (a, c, e) Three different bifurcation geometries are depicted, with the blood flow coming from the mother vessel (M) and draining in the numerically labeled daughter branches. These geometries are linked to the unique identifiers “♦” (a), “◆” (c), and “♦” (e) in Fig. 5.9. (b, d, f) Probability densities of lingering-associated void durations (solid lines) and non-lingering associated void durations (dashed lines) for the geometries on the left panel. The filled circles in the graphs indicate the median void durations. The dimensions and lingering frequencies are as follows: (b)  $P_{1,2}(\tau < 0.5 \tau_{\text{RBC}}) = \{0.45, 0.59\}$ ,  $\tilde{P}_{1,2}(\tau < 0.5 \tau_{\text{RBC}}) = \{0.37, 0.34\}$ ,  $n_{1,2,\text{linger}} = \{0.69, 0.42\}$ , with the corresponding measured vessel diameters  $d_{1,2} = \{3.1, 3.6\} \mu\text{m}$  at the position of the signal evaluation. Corresponding average flow rates are determined as  $q_{1,2} = Q_{1,2}/Q_M = \{0.39, 0.61\}$ . (d)  $P_{1,2}(\tau < 0.5 \tau_{\text{RBC}}) = \{0.08, 0.01\}$ ,  $\tilde{P}_{1,2}(\tau < 0.5 \tau_{\text{RBC}}) = \{0.00, 0.00\}$ ,  $n_{1,2,\text{linger}} = \{0.18, 0.06\}$ , with the corresponding measured vessel diameters  $d_{1,2} = \{3.9, 4.2\} \mu\text{m}$ , and normalized flow rates  $q_{1,2} = \{0.31, 0.69\}$ . (f)  $P_{1,2}(\tau < 0.5 \tau_{\text{RBC}}) = \{0.21, 0.41\}$ ,  $\tilde{P}_{1,2}(\tau < 0.5 \tau_{\text{RBC}}) = \{0.09, 0.18\}$ ,  $n_{1,2,\text{linger}} = \{0.39, 0.22\}$ ,  $d_{1,2} = \{2.9, 3.3\} \mu\text{m}$ , with normalized flow rates  $q_{1,2} = \{0.31, 0.69\}$ . Image adapted from reference [184].

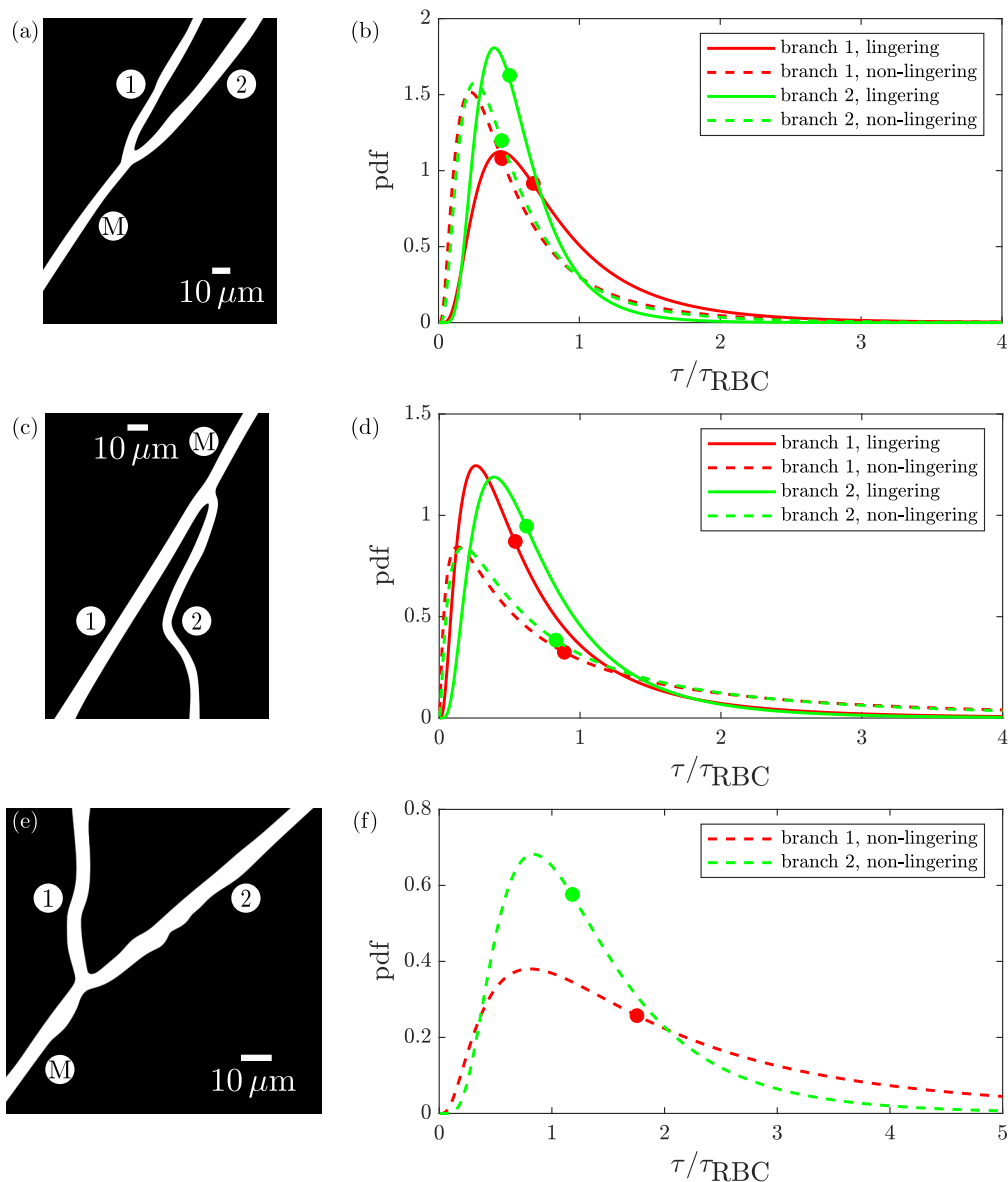


**Figure 5.12:** (a, c, e) Three different bifurcation geometries are depicted, with the blood flow coming from the mother vessel (M) and draining in the numerically labeled daughter branches. These geometries are linked to the unique identifiers “♦” (a), and “◆” (c) in Fig. 5.9. (b, d, f) Probability densities of lingering-associated void durations (solid lines) and non-lingering associated void durations (dashed lines) for the geometries on the left panel. The filled circles in the graphs indicate the median void durations. The dimensions and lingering frequencies are as follows: (b)  $P_{1,2}(\tau < 0.5 \tau_{RBC}) = \{0.55, 0.55\}$ ,  $\tilde{P}_{1,2}(\tau < 0.5 \tau_{RBC}) = \{0.32, 0.49\}$ ,  $n_{1,2,linger} = \{0.28, 0.36\}$ , with the corresponding measured vessel diameters  $d_{1,2} = \{3.1, 2.9\} \mu\text{m}$  at the position of the signal evaluation. Corresponding average flow rates are determined as  $q_{1,2} = \{0.59, 0.41\}$ . (d)  $P_{1,2}(\tau < 0.5 \tau_{RBC}) = \{0.34, 0.34\}$ ,  $\tilde{P}_{1,2}(\tau < 0.5 \tau_{RBC}) = \{0.46, 0.37\}$ ,  $n_{1,2,linger} = \{0.74, 0.72\}$ , with the corresponding measured vessel diameters  $d_{1,2} = \{3.3, 2.9\} \mu\text{m}$ , and normalized flow rates  $q_{1,2} = \{0.43, 0.57\}$ . (f) We do not observe a single lingering event of a RBC, and hence  $n_{1,2,linger} = \{0, 0\}$ . This special case is found to be the only one which does not obey any lingering events among all analyzed geometries. Image adapted from reference [184].

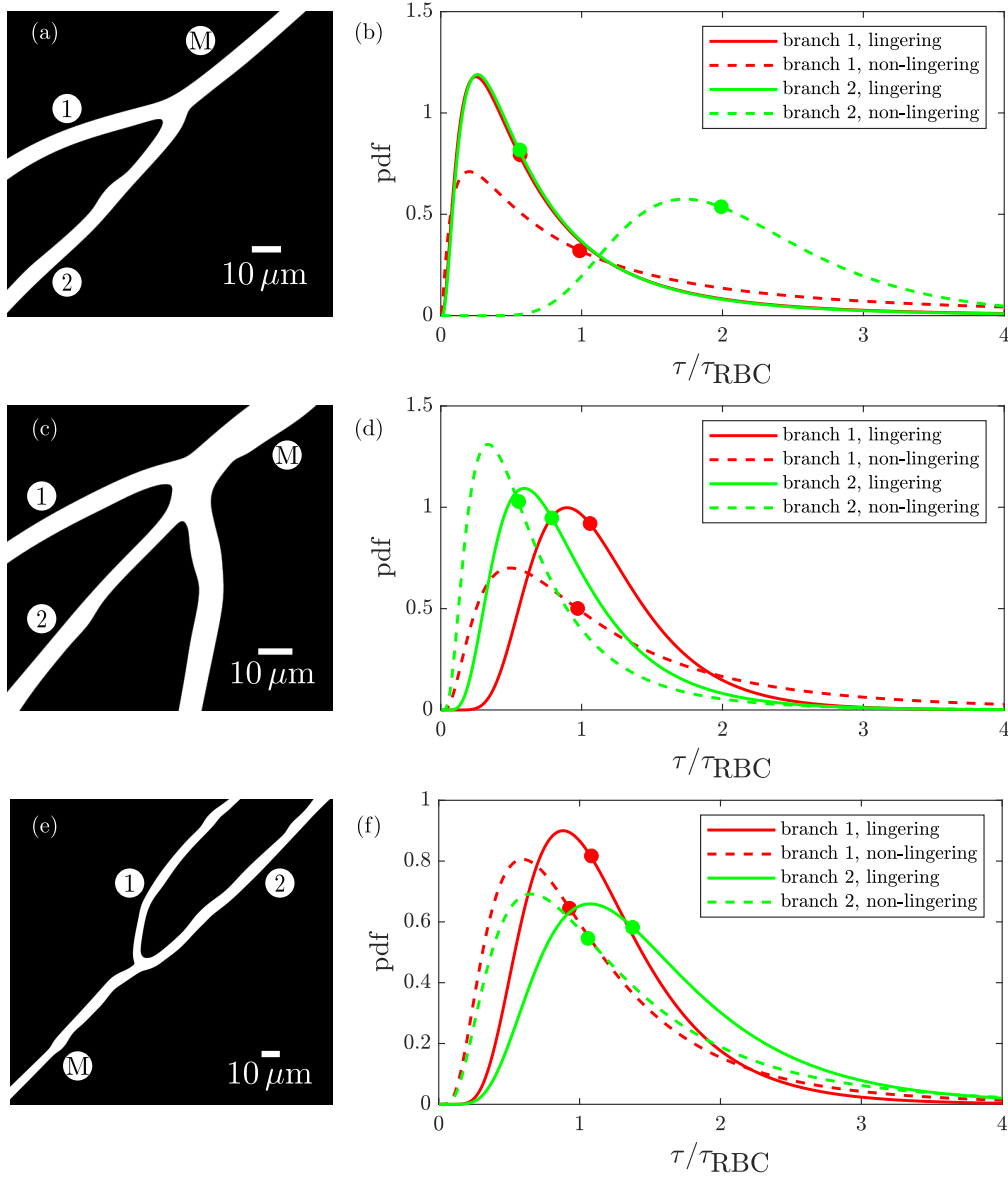


**Figure 5.13:** (a, c, e) Three different bifurcation geometries are depicted, with the blood flow coming from the mother vessel (M) and draining in the numerically labeled daughter branches. These geometries are linked to the unique identifiers “ $\blacktriangledown$ ” (a), and “ $\blacktriangledown$ ” (e) in Fig. 5.9. (b, d, f) Probability densities of lingering-associated void durations (solid lines) and non-lingering associated void durations (dashed lines) for the geometries on the left panel. The filled circles in the graphs indicate the median void durations. The dimensions and lingering frequencies are as follows: (b)  $P_{1,2}(\tau < 0.5 \tau_{\text{RBC}}) = \{0.29, 0.00\}$ ,  $\tilde{P}_{1,2}(\tau < 0.5 \tau_{\text{RBC}}) = \{0.44, 0.44\}$ ,  $n_{1,2,\text{linger}} = \{0.79, 0.80\}$ , with the corresponding measured vessel diameters  $d_{1,2} = \{4.6, 3.4\} \mu\text{m}$  at the position of the signal evaluation. Corresponding average flow rates are determined as  $q_{1,2} = \{0.55, 0.45\}$ . (d)  $P_{1,2}(\tau < 0.5 \tau_{\text{RBC}}) = \{0.21, 0.44\}$ ,  $\tilde{P}_{1,2}(\tau < 0.5 \tau_{\text{RBC}}) = \{0.03, 0.19\}$ ,  $n_{1,2,\text{linger}} = \{0.44, 0.37\}$ , with the corresponding measured vessel diameters  $d_{1,2} = \{3.6, 2.8\} \mu\text{m}$ , and normalized flow rates  $q_{1,2} = \{0.52, 0.48\}$ . (f)  $P_{1,2}(\tau < 0.5 \tau_{\text{RBC}}) = \{0.17, 0.14\}$ ,  $\tilde{P}_{1,2}(\tau < 0.5 \tau_{\text{RBC}}) = \{0.04, 0.02\}$ ,  $n_{1,2,\text{linger}} = \{0.11, 0.11\}$ , with the corresponding measured vessel diameters  $d_{1,2} = \{2.9, 2.3\} \mu\text{m}$ , and normalized flow rates  $q_{1,2} = \{0.55, 0.45\}$ . Image adapted from reference [184].

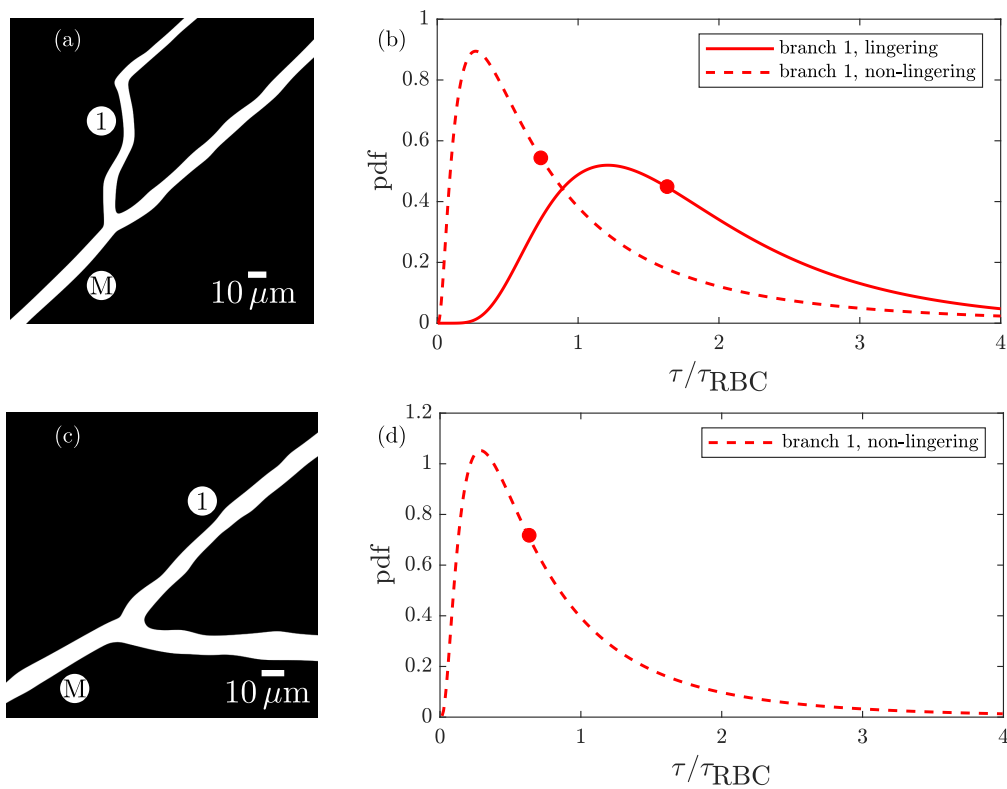


**Figure 5.14:** (a, c) Two bifurcation geometries are depicted, with the blood flow coming from the mother vessel (M) and draining in both respective daughter branches. However, in both cases, one of the daughter branches is not in the focal plane and thus not suitable for analysis. (b, d) Probability densities of lingering-associated void durations (solid lines), and non-lingering associated void durations (dashed lines) for the geometries on the left panel. The filled circles in the graphs indicate the median void durations. (b) Analogously to previous analyses, we find  $P_1(\tau < 0.5 \tau_{\text{RBC}}) = 0.35$ ,  $\tilde{P}_1(\tau < 0.5 \tau_{\text{RBC}}) = 0.01$ ,  $n_{1,\text{linger}} = 0.04$ , with the corresponding measured vessel diameter  $d_1 = 2.7 \mu\text{m}$  at the position of the signal evaluation. Since only one daughter vessel is prone to a quantitative analysis, we do not provide normalized flow rates. (d) We find  $P_1(\tau < 0.5 \tau_{\text{RBC}}) = 0.04$ , and the vessel diameter yields  $d_1 = 3.4 \mu\text{m}$ . Only two lingering events are detected throughout all passing cells, and hence  $n_{1,\text{linger}} = 0.00$ . Probability densities are not provided for these single events. Image adapted from reference [184].

#### 5.5.4 Deformation of RBCs in the vicinity of bifurcations

Since the deformability of RBCs is crucial to obey lingering events, we also analyzed the detailed deformation of RBCs in the vicinity of branches, i.e. bifurcation and confluence apices. However, lingering is caused by hardcore interaction between the surface of the RBC and the endothelium of the bifurcation apex, the sole presence of these apices already induces shape changes of RBCs which are approaching or distancing, respectively.

To assess the deformation of RBCs, we restrict the analysis to geometries that provide a reliable outcome from the particle tracking algorithm along the whole path of individual cells, yielding the eccentricity of detected cells. The geometry presented in Fig. 5.15 is the only suitable geometry prone to these preliminaries, exhibiting both a confluence and a bifurcation. However, we only derive a qualitative description of the deformation of RBCs, whose general

properties are similar in other geometries, and thus, our findings can easily be generalized to other bifurcation scenarios. To characterize this deformation behavior of flowing RBCs,

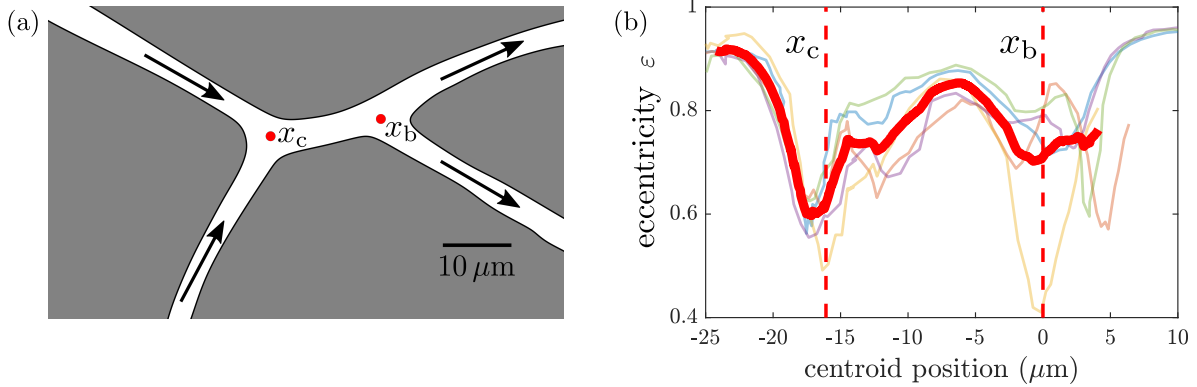


**Figure 5.15:** (a) Analyzed geometry to investigate the deformation behavior of flowing RBCs in a confluence-bifurcation scenario. The flow direction in each vessel is indicated by arrows, whereas the apex positions are indicated by  $x_b$ , and  $x_c$ , respectively, for a bifurcation and a confluence. (b) Eccentricity  $\varepsilon$  of RBCs, obtained by particle tracking, as a function of centroid position within the geometry in (a). The eccentricity is hereby calculated as the ratio of the distance between the two foci and the length of its major axis of an ellipse with the identical second moments for each individual RBC for all consecutive images. The thick red solid line represents the average of all individual graphs, represented by the thin shaded curves. For the analysis, only single cells are taken into account, i.e. trains of consecutive cells are rejected. The offset of the centroid position is chosen such that the bifurcation apex  $x_b$  is at position zero. Image adapted from reference [184].

we calculated the ellipse obeying the same second moments as each individual flowing RBC. From the parametrization of this ellipse, we obtain both the centroid position as well as the eccentricity  $\varepsilon$ , given as the ratio of the distance between the two foci and the length of its major axis. The spatio-temporal evolution of the eccentricity is shown in Fig. 5.15, both for each individual RBC as well as an average curve.

From the average curve, one can deduce the transition the cell shapes undergo while flowing through the vessels. While the RBCs are flowing in one of the daughter branches, they remain in an elongated shape due to the constriction of the narrow vessels. As they approach the confluence apex  $x_c$ , the eccentricity reaches the global minimum, indicating the most spherical shape. As the RBCs flow towards the bifurcation apex through the intermediate vessel, they elongate again, indicated by the local maximum at  $x \approx -7 \mu\text{m}$ . At the position of the bifurcation apex,  $x_b$ , the elongated RBC is expanding in a more spherical shape again, as is indicated by the local minimum of  $\varepsilon$ . Finally, when entering one of the two branching vessels, the elongation increases again. As a main difference to the lingering phenomenon, the cell speed is adapted to the individual flow rates in the daughter branches of the geometry. In the lingering case, however, the reduction of the speed is significantly below the mean speed of the bulk flow.

## 5.6 Discussion

In section 5.5.1, we showed evidence of an apparent increase in median void durations for the majority of investigated geometries. Since we analyzed the formations of voids downstream the bifurcation apex in the given geometry, this increase originates out of two distinct contributions. In reference [75], lingering events are characterized by the type of blockage they cause. In the case of a symmetrical lingering, the reduction of flow rates in every daughter vessel is reduced equally. In contrast, asymmetrically lingering RBCs lead to a nonuniform constriction of both daughter vessels, leading to an imbalanced partition of the respective flow rates (cf. Fig. 5.2). They show furthermore, that these asymmetric lingering events occur periodically in the sense that the flow rates in both daughter vessels fluctuate periodically for subsequent lingering events. We conjecture this unequal reduction of flow rates to be one cause of the increased void durations in our experimental data. A redistribution of consecutive RBCs further upstream of the lingering RBC is the manifestation of this effect, leading to an increased median void duration.

A second contribution of the aforementioned increase on the temporal void duration is yielded by the break up of clusters of flowing RBCs, induced by a lingering cell. We refer to the term cluster as trains of moving RBCs, where the intercellular distance is in the order of the cellular size, where hydrodynamic interactions are ubiquitous [22, 30]. The partial obstruction caused by a lingering RBC leads to an alteration of the flow rate in one or both daughter vessels. However, this decreased flow rate is related to a change in void speed in the affected vessel, which in turn implies that the distance between consecutive RBCs and hence the spatial void length sustains in the prevalent Reynolds regime. Yet, we do not observe this in our data. Although deviations of individual cell speeds from the mean speed are present, the variance of these is smaller than the mean speed itself, i.e.,  $\text{var}(\tau_{i,\text{RBC}})/\langle\tau_{i,\text{RBC}}\rangle < 0.5$ . In addition, deviations from the mean speed are arbitrarily distributed, independent of lingering events, but rather governed by the temporal flow heterogeneity of the whole microvascular network. We use this observation a posteriori as a justification to consider the mean RBC passage time as a normalization factor for the void durations since the variation of each individual RBC passage time is negligible within the experimental limits.

In Fig. 5.16, intensity signals of all investigated branches of the geometry in Fig. 5.5 are depicted, where the flow characteristics of RBCs and voids can be qualitatively inferred. From these findings, we conjecture that temporal void durations and spatial void lengths are highly correlated, and this implies a breakup of clusters of RBCs while approaching a lingering RBC at a bifurcation apex. Similarly, the considerations above explain the suppression of short void durations.

The spatio-temporal heterogeneity of cell distributions leads furthermore to the rather long-tailed probability densities of void durations provided in sections 5.5.1 and 5.5.3. These long tails emerge from the inherent flow properties of the microvascular network itself, rather than as a direct consequence of a lingering event. Depending on the actual geometrical parameters of the bifurcation and its feeding and draining vessels, we observe cell-depleted sequences and regions, up to an entirely plasmatic flow in extreme cases and thus long void durations in absence of lingering events.

So far, effects arising from individual lingering events on the blood flow in the constituent vessels of the bifurcation have been elucidated. When it comes to the impact on the blood flow, the number of lingering events among all traversing RBCs, in other words, the lingering frequency, is of high importance. Despite the fact that most parameters allegedly influenc-

ing this quantity are inaccessible in our experimental setup, we restrict our analysis to the dependence of lingering frequency on the flow rates in both daughter vessels. From Fig. 5.9, we find a decreased frequency in the vessel with a higher flow rate with respect to its counterpart among all investigated adjacent vessel pairs. RBCs merely follow the streamlines of the surrounding plasma [65], hence fewer cells are flowing in the vessel with a lower flow rate. Despite this observation, the interplay of RBCs with the endothelium is highly complex [133], and thus it is non-intuitive to obey this relationship also for lingering cells. Even more remarkable is the circumstance that we find the aforementioned correlation for all analyzed geometries, independent of the cutting angles between feeding vessels and daughter vessels.

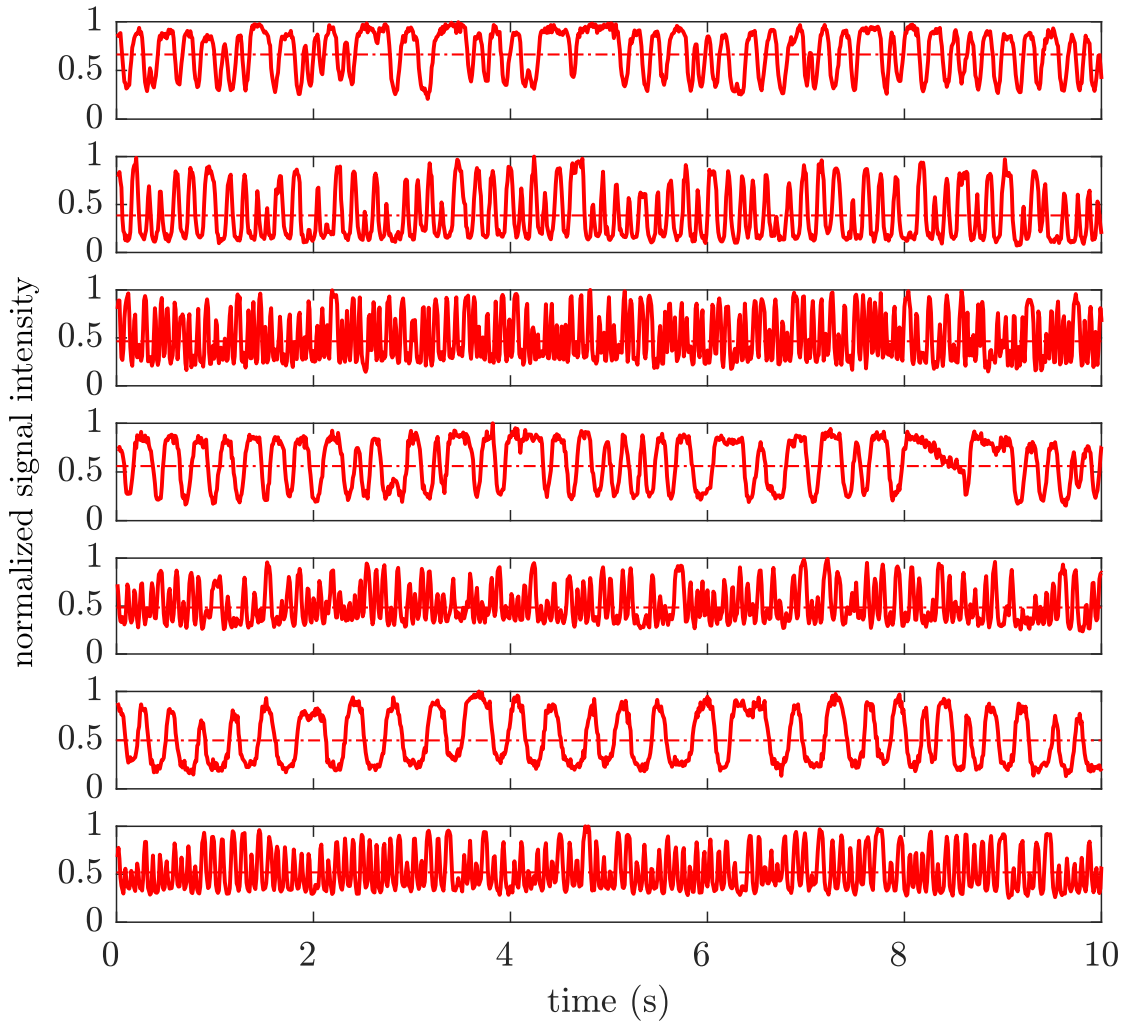


**Figure 5.16:** Integrated intensity signals for all branches of the geometry depicted in Fig. 5.5 in ascending order. In each subplot, the red dash-dotted line represents the mean value of the integrated intensity. These mean values of the integrated intensity serve as a threshold to binarize the signals and thus to define voids and RBCs, respectively. For a better comparison, the integrated intensities are normalized in each branch. From the local minima and the width of the binarized peaks, one can see that the passage time of RBCs is narrowly distributed in every respective branch.

Furthermore, the difference in lingering frequencies of associated adjacent vessels vanishes as

the flow rates approach an equal partition, i.e., close to  $0.5 \times Q_M$ . Yet, we find no evidence that the overall magnitude of the lingering frequency is affected by relative flow rates but rather influenced by the cutting angle between the feeding and the draining vessels, such that smaller angles exhibit higher lingering frequencies in most cases.

The observed increase of the median void durations in conjunction with the suppression of void durations  $\tau < 0.5 \tau_{\text{RBC}}$  leads to a decreased fraction of RBCs in the daughter vessels in the case of lingering, and thus, to a reduction in the hematocrit. This hematocrit reduction downstream the bifurcation in the presence of lingering events is also observed in the study of Balogh *et al.* [75], modeling a realistic microvascular network in silico. They further report the lingering to be causing a hematocrit reduction upstream the bifurcation. Due to the fact that the feeding vessel in our investigated geometries typically provides a bulk flow of RBCs, we can not assess the density of flowing RBCs and hence the hematocrit in that vessel. For future experiments, this limitation could be improved by an enlarged field of view and improved image acquisition with the aid of high-speed cameras capable of recording at a higher framerate. However, we conjecture that the aforementioned trains of RBCs approaching a bifurcation apex in peculiar cases result from this hematocrit reduction upstream of the investigated bifurcation.

The very good qualitative agreement between our experimental results and their observations in silico is remarkable given the sheer complexity of the overall microvascular network in the used hamster model and the experimental drawbacks, such as limited knowledge of the overall geometry due to a limited insight, contrasting the well-defined boundary conditions implemented in the numerical modeling. Furthermore, we observe in all but one geometry lingering events, which are also matched in silico, where all investigated bifurcations embodied lingering cells, yet the most pronounced in capillaries.

By combining the observation of the imbalanced lingering frequency and the median increase of void durations, we conjecture that the *classical* partitioning behavior of RBCs according to the Zweifach-Fung effect even underestimates the hematocrit reduction due to lingering scenarios. We attribute this deviation to the fact that lingering has not been taken into account in the existing in vivo studies and therefore, the complex interaction of the RBC structure with the endothelium is not mirrored [133]. In fact, these interactions and the finite size effects of RBCs are identified as the major contributions to the underestimation of the cell partitioning in silico [76].

Even though we assess the impact of lingering cells at bifurcations on the distribution of subsequently flowing RBCs, detailed knowledge of the exact flow profiles and pressure distributions in the local vessels is lacking. However, these parameters are crucial to provide a holistic view on the lingering events, especially since Balogh *et al.* [75] showed evidence that lingering RBCs are responsible for a negative pressure-flow correlation, which is absent in the case of non-lingering cells and contradicts the positive pressure-flow correlation deduced from Poiseuille's law. In future experiments, a more detailed knowledge of flow profiles can be obtained by the injection of fluorescent tracer particles, which have already been employed to confirm margination and antimargination behavior in recent studies [189]. Endowed with the knowledge of flow profiles within the bifurcation geometry, we would further be able to estimate the wall shear stress, which has also been found to increase drastically in the lingering scenario, and which is linked to triggering angiogenesis and angioadaptation (cf. sections 5.2 - 5.2.2).

We focused so far on the impact of lingering events on the characteristics and dynamics of hematological parameters. However, the origin and prerequisites to facilitate lingering have not been discussed yet. The inner network of spectrin fibers plays an important role since it

provides the crucial deformation ability of RBCs, allowing them to squeeze through constrictions much smaller than their equilibrium size [218, 219]. We investigated this deformability in the vicinity of branching and confluent vessels, and find a characteristic deformation pattern for RBCs approaching a bifurcation apex and distancing a confluence apex, respectively, as depicted in Fig. 5.15. These characteristic deformations match the findings of recent simulations addressing the deformation for a various number of RBCs approaching a bifurcation [78]. We stress that this shape deformation depends on the confinement of the underlying geometry and this strong coupling with the plasma results in the observed lingering phenomenon. Parameters such as opening angles or curvatures of the endothelium at the apex are essential determinants of lingering behavior since they in turn have an impact on the position of RBCs and their trajectory. The bending rigidity of RBCs is also known to be altered by various diseases, and therefore we conjecture that the impact of lingering on the overall health state may also vary with other pathological states.

## 5.7 Summary

Using state-of-the-art intravital microscopy, we are able to extract image sequences of the blood flow in living Syrian golden hamsters. In addition to a joint application of a customized particle tracking algorithm and sophisticated signal processing within a vessel segment, we analyzed the distribution of RBCs and cell-free areas, the voids, inside a given microvascular geometry. Motivated by recent *in silico* studies addressing effects arising from the particulate nature of blood suspensions, we focus in the data analysis on the influence of RBCs resting at a bifurcation apex, the so-called lingering phenomenon. More precisely, we aimed to separate voids that are linked to these lingering RBCs from voids that are not in direct connection to any lingering RBC.

We show that in the case of lingering-associated voids the median void duration is in the majority of investigated geometries increased with respect to non-lingering associated voids. In some extreme cases, we observed that the median void durations in the case of lingering exceeded 1.5 times the median void durations in the non-lingering case. Additionally, we note a suppression of very short void durations in the lingering case, which is not mirrored in the latter case. Both, the suppression of short void durations and the shift of median void durations towards higher values are associated with a reduction of the hematocrit downstream the bifurcation. This observation is in very good qualitative agreement with the *in silico* results presented in reference [75]. We conjecture that this decreased hematocrit is caused by a break-up of clusters of RBCs approaching a lingering RBC, and furthermore, a redistribution of subsequent cells into the adjacent daughter vessel. Even though these effects seem to be rather fine-grained, the impact on the whole organism may be severe, given the importance of microvascular blood flow to the health state. Indeed, lingering is found to contribute to peaks in the local wall shear stress, which in turn is known to be an important trigger for the pruning of new vessels, the angiogenesis. The lingering phenomenon itself is governed by the topology of the bifurcation apex and its constituent vessels; however, the cellular deformability plays a key role. Considering the fraction of lingering cells and the total count of passing cells, the lingering frequency, we find a significant amount of cells to linger at a bifurcation. We thus conclude that the lingering phenomenon is one important factor among others, influencing the development of microvascular beds and their topology. It has a tremendous impact on the flow characteristics of the subsequent bloodstream and may be altered significantly by

pathological states influencing the rigidity of RBCs.

Our findings may further serve as a benchmark for the accuracy and the performance of in silico models, addressing microvascular blood flow.



## General Conclusion and Perspectives

In this work, we present two research projects illustrating the importance of the intrinsic deformability of red blood cells (RBCs) in microcapillary flow regimes. Structurally, the work is divided into two parts, with the first one dedicated to *in vitro* experiments of driven dilute RBC suspensions in straight capillaries and the phenomenological characterization of their hydrodynamically induced shapes. The second part investigates the dynamics of RBCs *in vivo* upon approaching bifurcation apices *in vivo* and the consequences of this so-called lingering behavior on the distribution of the subsequent RBC flux.

In the first part, we evaluated the hydrodynamically induced shapes of RBCs and constructed a shape phase diagram based on a binary classification into axisymmetric shapes, termed croissants, and asymmetric shapes oriented towards the channel walls, called slippers. The findings of the conducted *in vitro* experiments are backed up by sophisticated 3D simulations to mimic the flow of isolated RBCs in a channel segment of identical dimensions as in the former case. Both methodologies show a very good congruence for all implied flow velocities, ranging from  $0.1 \text{ mm s}^{-1}$  –  $10 \text{ mm s}^{-1}$  and thus covering the entire regime of flow conditions prevalent in the microvasculature of the human body. Moreover, the simulations employed different initial shape configurations to investigate the impact of this initial configuration on the terminal state.

Compared to previous studies addressing the hydrodynamically induced shapes, the simulations, as well as the experiment, used physiological viscosity ratios of  $\lambda_{\text{visc}} \approx 5$ , which is known to be a crucial parameter for the steady-state shape.

The evaluation of the RBC shapes obtained *in vitro* has been carried out manually, which is potentially biased due to the subjective human classification and the lack of suitable parameters associated with distinct shape categories. To overcome these drawbacks, we designed a state-of-the-art convolutional neural network (CNN), trained to classify the input images according to our binary classification scheme. However, standard CNN approaches for object recognition and pattern detection provide an unsatisfactory environment since the dataset comprised of all recorded RBC images flowing in the microfluidic channel additionally consists of indistinguishable shapes, referred to as others, besides croissants and slippers. Therefore, the employed CNN is a regression-type network, yielding a continuous output number to which, in a subsequent step, thresholds are adjusted to minimize a predefined cost function. Overall, this procedure reproduces the manually obtained phase diagram of RBC shapes, yet with an unbiased output and highly time-efficient. This automatized classification thus forms the basis for future developments of cost-inexpensive, label-free tools prevalent in lab-on-a-chip devices.

The building blocks this research is resting on can easily be extended to consolidate the current findings. Starting with the microfluidic chip design, we are confident to investigate cross-sections with further aspect ratios in particular and different geometries in general. Albeit the flow regimes and typical dimensions are covered in the body of mammals, the use of rectangular ducts can only serve as an approximation of the actual findings *in vivo*. Unfortunately, the experimental setup is limited to projections of the RBC, which reduces the

information and hence increases the complexity of the shape evaluation. We are confident to resolve this limiting factor in future studies by in situ hardening of flowing RBCs with the aid of externally triggered activation of the crosslinker glutaraldehyde and ensuing characterization of the obtained cell shapes via high-resolution microscopy techniques. Hence, more characteristic details can be resolved, achieving an easier comparison with RBC shapes obtained via 3D simulations. In particular, the 3D information of the RBC shapes in vitro might elucidate the occurrence of others, which we attribute partially due to a lack of multiple view angles. Similarly, others may form subpopulations of shapes that can be accounted for with additional morphological information, since e.g. the auxiliary class of sheared croissants resembles inverted slippers, but contributes to the population of others. In the context of automated analysis of RBC shapes, we are currently limited by data acquisition and storage. To promote the diagnostic usefulness of the CNN technique, a reduction of the data transfer is crucial, especially concerning an on-the-fly analysis of cell shapes. Recent, yet preliminary developments comprise the modulation of the cell images with specialized binary masks and the recording of the resulting one-dimensional signal, allowing for high throughputs and instantaneous cell recognition.

Analogously, we have to benchmark the sensitivity of the CNN approach by the characterization of blood diseases associated with a change in morphology or the RBC deformability. Preliminary experiments with drug-induced alterations of the RBC rigidity lead to shifts in the transition velocity of slippers and croissants, where both shape fractions are equally likely to observe. Additionally, the overall populations are reduced in both cases. Nevertheless, systematic studies characterizing RBC disorders and their implications in the phase diagram are inevitable.

Secondly, we investigated the lingering phenomenon at bifurcation apices, defined as RBCs resting at an apex which in silico has been found to evoke a piling up of subsequent RBCs. To characterize the lingering events we analyzed multiple bifurcating vessels in the microvasculature of five living Syrian golden hamsters in total. Subsequently, the intercellular distances between a lingering RBC and the closest preceding RBC downstream in each daughter vessel, the void durations, have been monitored with the aid of a sophisticated combination of RBC tracking and signal intensity correlations. This approach allowed us to separate the influence of lingering RBCs from the non-lingering RBCs. In most observed geometries, the lingering of RBCs leads to an increase of the temporal void durations with respect to non-lingering associated void durations, and thus, a temporarily decreased hematocrit.

Recent in silico studies indicate a correlation between the lingering events of RBCs at microvascular bifurcation apices, and the distribution of wall shear stress and local pressure gradients, which in turn are identified as an important factor of angiogenesis. To correlate lingering events with wall shear stress in vivo and thus confirm the findings in silico, a precise knowledge of the local flow profiles is necessary. For this purpose, we plan to inject tracer particles into the hamster models, such that we can retrieve detailed information about the plasma flow rates, in contrast to the flux of RBCs which we can extract so far. Additionally, in vitro studies of bifurcating geometries exhibiting various angles and dimensions need to be designed, where the flow rates can be adjusted precisely. Besides the injection of tracer particles, the insertion of a fraction of RBCs exhibiting a decreased deformability into the bloodstream can be associated with pathological states affecting the deformability of RBCs and their influence on lingering characteristics, which in turn affects the partitioning of RBCs and ultimately, the supply of oxygen in the tissues. This oxygen supply is potentially altered directly by redistribution of the RBCs as oxygen carriers, but also indirectly by the induced

vascular growth and angiogenesis resulting from locally increased wall shear stress. Furthermore, the influence of the topological structure of the network can be analyzed, which is limited *in vivo* by the field of view and more importantly, by the non-planar structure of the microvascular bed. Moreover, the investigation of additional bifurcation sites will increase the statistical relevance and eventually allow to predict the occurrence of lingering events or even the severity of lingering upon retrieving a distinct scenario in the microvasculature. Currently, we cannot reliably relate parameters such as cutting angles of both daughter vessels, flow rates, or diameter ratios to the impact of lingering events, although the influence of these parameters has been found to impact the partitioning of hematocrits at microvascular bifurcations in general, both *in vivo* and *in silico*.



## Bibliography

- [1] G. Danker, T. Biben, et al. “Dynamics and Rheology of a Dilute Suspension of Vesicles: Higher-Order Theory”. *Phys. Rev. E* 76 (4) (2007), p. 041905.
- [2] V. Vitkova, M.-A. Mader, et al. “Micro-Macro Link in Rheology of Erythrocyte and Vesicle Suspensions”. *Biophysical Journal* 95 (6) (2008), pp. L33–L35.
- [3] D. Katanov, G. Gompper, and D. A. Fedosov. “Microvascular Blood Flow Resistance: Role of Red Blood Cell Migration and Dispersion”. *Microvasc. Res.* 99 (2015), pp. 57–66.
- [4] M. Thiébaud, Z. Shen, et al. “Prediction of Anomalous Blood Viscosity in Confined Shear Flow”. *Physical Review Letters* 112 (23) (2014), p. 238304.
- [5] *Global Health Estimates 2016: Deaths by Cause, Age, Sex, by Country and by Region, 2000-2016*. 2018.
- [6] S. Chien, S. Usami, et al. “Effects of Hematocrit and Plasma Proteins on Human Blood Rheology at Low Shear Rates.” *J. Appl. Physiol.* 21 (1) (1966), pp. 81–87.
- [7] R. Skalak, S. R. Keller, and T. W. Secomb. “ASME Centennial Historical Perspective Paper: Mechanics of Blood Flow”. *Journal of Biomechanical Engineering* 103 (2) (1981), pp. 102–115.
- [8] R. E. Wells and E. W. Merrill. “Shear Rate Dependence of the Viscosity of Whole Blood and Plasma”. *Science* 133 (3455) (1961), pp. 763–764.
- [9] M. M. Kay. “Mechanism of removal of senescent cells by human macrophages in situ.” *Proceedings of the National Academy of Sciences* 72 (9) (1975), pp. 3521–3525.
- [10] O. Linderkamp and H. J. Meiselman. “Geometric, osmotic, and membrane mechanical properties of density-separated human red cells”. *Blood* 59 (6) (1982), pp. 1121–1127.
- [11] Y.-C. Fung. “Stochastic flow in capillary blood vessels”. *Microvascular Research* 5 (1) (1973), pp. 34–48.
- [12] K. Svanes and B. Zweifach. “Variations in small blood vessel hematocrits produced in hypothermic rats by micro-occlusion”. *Microvascular Research* 1 (2) (1968), pp. 210–220.
- [13] D. Halpern and T. W. Secomb. “The squeezing of red blood cells through capillaries with near-minimal diameters”. *Journal of Fluid Mechanics* 203 (1989), pp. 381–400.
- [14] J. B. Freund. “The flow of red blood cells through a narrow spleen-like slit”. *Physics of Fluids* 25 (11) (2013), p. 110807.
- [15] J. Picot, P. A. Ndour, et al. “A biomimetic microfluidic chip to study the circulation and mechanical retention of red blood cells in the spleen: Red blood cells deformability in a spleen-like-microfluidic-chip”. *American Journal of Hematology* 90 (4) (2015), pp. 339–345.

- [16] S. Salehyar and Q. Zhu. “Deformation and internal stress in a red blood cell as it is driven through a slit by an incoming flow”. *Soft Matter* 12 (13) (2016), pp. 3156–3164.
- [17] M. Abkarian, M. Faivre, et al. “Cellular-scale hydrodynamics”. *Biomedical Materials* 3 (3) (2008), p. 034011.
- [18] G. Deplaine, I. Safeukui, et al. “The Sensing of Poorly Deformable Red Blood Cells by the Human Spleen Can Be Mimicked in Vitro”. *Blood* 117 (8) (2011), e88–e95.
- [19] I. V. Pivkin, Z. Peng, et al. “Biomechanics of Red Blood Cells in Human Spleen and Consequences for Physiology and Disease”. *PNAS* 113 (28) (2016), pp. 7804–7809.
- [20] A. M. Forsyth, J. Wan, et al. “Multiscale Approach to Link Red Blood Cell Dynamics, Shear Viscosity, and ATP Release”. *Proc. Natl. Acad. Sci.* 108 (27) (2011), pp. 10986–10991.
- [21] A. Farutin and C. Misbah. “Symmetry Breaking and Cross-Streamline Migration of Three-Dimensional Vesicles in an Axial Poiseuille Flow”. *Phys. Rev. E* 89 (4) (2014), p. 042709.
- [22] M. Brust, O. Aouane, et al. “The Plasma Protein Fibrinogen Stabilizes Clusters of Red Blood Cells in Microcapillary Flows”. *Sci. Rep.* 4 (2014), p. 4348.
- [23] R. Skalak and P. I. Branemark. “Deformation of Red Blood Cells in Capillaries”. *Science* 164 (3880) (1969), pp. 717–719.
- [24] P. Gaehtgens, C. Dührssen, and K. H. Albrecht. “Motion, deformation, and interaction of blood cells and plasma during flow through narrow capillary tubes”. *Blood Cells* 6 (4) (1980), pp. 799–817.
- [25] K. Kubota, J. Tamura, et al. “The Behaviour of Red Cells in Narrow Tubes in Vitro as a Model of the Microcirculation”. *Br. J. Haematol.* 94 (2) (1996), pp. 266–272.
- [26] J. L. McWhirter, H. Noguchi, and G. Gompper. “Flow-induced clustering and alignment of vesicles and red blood cells in microcapillaries”. *Proceedings of the National Academy of Sciences of the United States of America* 106 (15) (2009), pp. 6039–6043.
- [27] J. L. McWhirter, H. Noguchi, and G. Gompper. “Deformation and Clustering of Red Blood Cells in Microcapillary Flows”. *Soft Matter* 7 (22) (2011), pp. 10967–10977.
- [28] G. Tomaiuolo, L. Lanotte, et al. “Red Blood Cell Clustering in Poiseuille Microcapillary Flow”. *Phys. Fluids* 24 (5) (2012), pp. 1–8.
- [29] C. Wagner, P. Steffen, and S. Svetina. “Aggregation of Red Blood Cells: From Rouleaux to Clot Formation”. *Comptes Rendus Phys. Living fluids / Fluides vivants* 14 (6) (2013), pp. 459–469.
- [30] V. Clavería, O. Aouane, et al. “Clusters of red blood cells in microcapillary flow: hydrodynamic versus macromolecule induced interaction”. *Soft Matter* 12 (39) (2016), pp. 8235–8245.
- [31] M. M. Guest, T. P. Bond, et al. “Red Blood Cells: Change in Shape in Capillaries”. *Science* 142 (3597) (1963), pp. 1319–1321.
- [32] S. Guido and G. Tomaiuolo. “Microconfined Flow Behavior of Red Blood Cells in Vitro”. *Comptes Rendus Phys.* 10 (8) (2009), pp. 751–763.
- [33] G. Tomaiuolo, L. Lanotte, et al. “Microconfined Flow Behavior of Red Blood Cells”. *Med. Eng. Phys.* 38 (1) (2016), pp. 11–16.

- 
- [34] H. L. Goldsmith, J. Marlow, and F. C. MacIntosh. “Flow behaviour of erythrocytes - I. Rotation and deformation in dilute suspensions”. *Proceedings of the Royal Society of London. Series B. Biological Sciences* 182 (1068) (1972), pp. 351–384.
- [35] U. Bagge, P. I. Br{\textbackslash}aanemark, et al. “Three-Dimensional Observations of Red Blood Cell Deformation in Capillaries”. *Blood Cells* 6 (2) (1980), pp. 231–239.
- [36] R. Hochmuth, R. Marple, and S. Sutera. “Capillary blood flow”. *Microvascular Research* 2 (4) (1970), pp. 409–419.
- [37] V. Seshadri, R. M. Hochmuth, et al. “Capillary Blood Flow: III. Deformable Model Cells Compared to Erythrocytes in Vitro”. *Microvascular Research* 2 (4) (1970), pp. 434–442.
- [38] L. Lanotte. “Deformation and Aggregation of Red Blood Cells and Vesicles Flowing in Microchannels”. PhD thesis. Università degli Studi di Napoli Federico II, 2013.
- [39] L. Lanotte, G. Tomaiuolo, et al. “Red Blood Cell Dynamics in Polymer Brush-Coated Microcapillaries: A Model of Endothelial Glycocalyx in Vitro”. *Biomicrofluidics* 8 (1) (2014), p. 014104.
- [40] G. Prado, A. Farutin, et al. “Viscoelastic Transient of Confined Red Blood Cells”. *Biophysical Journal* 108 (9) (2015), pp. 2126–2136.
- [41] G. Tomaiuolo and S. Guido. “Start-up shape dynamics of red blood cells in microcapillary flow”. *Microvascular Research* 82 (1) (2011), pp. 35–41.
- [42] V. P. Zharov, E. I. Galanzha, et al. “In Vivo High-Speed Imaging of Individual Cells in Fast Blood Flow”. *J. Biomed. Opt* 11 (5) (2006), pp. 054034–054034–4.
- [43] K. Tsukada, E. Sekizuka, et al. “Direct Measurement of Erythrocyte Deformability in Diabetes Mellitus with a Transparent Microchannel Capillary Model and High-Speed Video Camera System”. *Microvasc. Res.* 61 (3) (2001), pp. 231–239.
- [44] T. Secomb and R. Skalak. “A two-dimensional model for capillary flow of an asymmetric cell”. *Microvascular Research* 24 (2) (1982), pp. 194–203.
- [45] T. W. Secomb, R. Skalak, et al. “Flow of Axisymmetric Red Blood Cells in Narrow Capillaries”. *J. Fluid Mech.* 163 (1986), pp. 405–423.
- [46] T. W. Secomb. “Flow-Dependent Rheological Properties of Blood in Capillaries”. *Microvascular Research* 34 (1) (1987), pp. 46–58.
- [47] T. W. Secomb, B. Styp-Rekowska, and A. R. Pries. “Two-Dimensional Simulation of Red Blood Cell Deformation and Lateral Migration in Microvessels”. *Annals of Biomedical Engineering* 35 (5) (2007), pp. 755–765.
- [48] O. Aouane, M. Thiébaud, et al. “Vesicle Dynamics in a Confined Poiseuille Flow: From Steady State to Chaos”. *Phys. Rev. E* 90 (3) (2014), p. 033011.
- [49] B. Kaoui, J. Harting, and C. Misbah. “Two-Dimensional Vesicle Dynamics under Shear Flow: Effect of Confinement”. *Phys. Rev. E* 83 (6) (2011), p. 066319.
- [50] N. Tahiri, T. Biben, et al. “On the problem of slipper shapes of red blood cells in the microvasculature”. *Microvascular Research* 85 (2013), pp. 40–45.
- [51] G. R. Cokelet and H. J. Meiselman. “Rheological Comparison of Hemoglobin Solutions and Erythrocyte Suspensions”. *Science* 162 (3850) (1968), pp. 275–277.
- [52] R. E. Waugh and R. M. Hochmuth. “Chapter 60: Mechanics and Deformability of Hematocytes”. *Biomedical Engineering Fundamentals*. Ed. by J. D. Bronzino. 1st ed. CRC Press, 2006, pp. 60–63.

- [53] R. Skalak and S. Chien, eds. *Handbook of bioengineering*. New York: McGraw-Hill, 1987. 1 p.
- [54] H. Noguchi and G. Gompper. “Shape transitions of fluid vesicles and red blood cells in capillary flows”. *Proceedings of the National Academy of Sciences* 102(40) (2005), pp. 14159–14164.
- [55] D. A. Fedosov, M. Peltomäki, and G. Gompper. “Deformation and dynamics of red blood cells in flow through cylindrical microchannels”. *Soft Matter* 10(24) (2014), pp. 4258–4267.
- [56] M. Faivre, M. Abkarian, et al. “Geometrical Focusing of Cells in a Microfluidic Device: An Approach to Separate Blood Plasma”. *Biorheology* 43(2) (2006), pp. 147–159.
- [57] G. Tomaiuolo, M. Simeone, et al. “Red blood cell deformation in microconfined flow”. *Soft Matter* 5(19) (2009), p. 3736.
- [58] R. T. Carr and J. Xiao. “Plasma Skimming in Vascular Trees: Numerical Estimates of Symmetry Recovery Lengths”. *Microcirculation* 2(4) (1995), pp. 345–353.
- [59] T. Ye, H. Shi, et al. “Relationship between Transit Time and Mechanical Properties of a Cell through a Stenosed Microchannel”. *Soft Matter* (2017).
- [60] T. Ye, N. Phan-Thien, et al. “Red Blood Cell Motion and Deformation in a Curved Microvessel”. *J. Biomech.* (2017).
- [61] H. Lipowsky and B. Zweifach. “Network analysis of microcirculation of cat mesentery”. *Microvascular Research* 7(1) (1974), pp. 73–83.
- [62] H. H. Lipowsky, S. Kovalcheck, and B. W. Zweifach. “The distribution of blood rheological parameters in the microvasculature of cat mesentery.” *Circulation Research* 43(5) (1978), pp. 738–749.
- [63] H. H. Lipowsky, S. Usami, and S. Chien. “In Vivo Measurements of “Apparent Viscosity” and Microvessel Hematocrit in the Mesentery of the Cat”. *Microvasc. Res.* 19(3) (1980), pp. 297–319.
- [64] B. M. Fenton, R. T. Carr, and G. R. Cokelet. “Nonuniform red cell distribution in 20 to 100  $\mu\text{m}$  bifurcations”. *Microvascular Research* 29(1) (1985), pp. 103–126.
- [65] G. W. Schmid-Schönbein, R. Skalak, et al. “Cell distribution in capillary networks”. *Microvascular Research* 19(1) (1980), pp. 18–44.
- [66] A. R. Pries, K. Ley, et al. “Red cell distribution at microvascular bifurcations”. *Microvascular Research* 38(1) (1989), pp. 81–101.
- [67] R. T. Carr and L. L. Wickham. “Plasma skimming in serial microvascular bifurcations”. *Microvascular Research* 40(2) (1990), pp. 179–190.
- [68] J. M. Sherwood, D. Holmes, et al. “Spatial Distributions of Red Blood Cells Significantly Alter Local Haemodynamics”. *PLoS ONE* 9(6) (2014). Ed. by J. C. d. Alamo, e100473.
- [69] Z. Shen, G. Couplier, et al. “Inversion of hematocrit partition at microfluidic bifurcations”. *Microvascular Research* 105 (2016), pp. 40–46.
- [70] S. Yang, A. Ündar, and J. D. Zahn. “A microfluidic device for continuous, real time blood plasma separation”. *Lab Chip* 6(7) (2006), pp. 871–880.

- 
- [71] X. Li, A. S. Popel, and G. E. Karniadakis. “Blood–plasma Separation in Y-Shaped Bifurcating Microfluidic Channels: A Dissipative Particle Dynamics Simulation Study”. *Phys. Biol.* 9 (2) (2012), p. 026010.
- [72] S. Tripathi, A. Prabhakar, et al. “Blood plasma separation in elevated dimension T-shaped microchannel”. *Biomedical Microdevices* 15 (3) (2013), pp. 415–425.
- [73] S. Tripathi, Y. V. B. Varun Kumar, et al. “Passive blood plasma separation at the microscale: a review of design principles and microdevices”. *Journal of Micromechanics and Microengineering* 25 (8) (2015), p. 083001.
- [74] T. Wang, U. Rongin, and Z. Xing. “A micro-scale simulation of red blood cell passage through symmetric and asymmetric bifurcated vessels”. *Scientific Reports* 6 (1) (2016), p. 20262.
- [75] P. Balogh and P. Bagchi. “Direct Numerical Simulation of Cellular-Scale Blood Flow in 3D Microvascular Networks”. *Biophysical Journal* 113 (12) (2017), pp. 2815–2826.
- [76] P. Balogh and P. Bagchi. “Analysis of red blood cell partitioning at bifurcations in simulated microvascular networks”. *Physics of Fluids* 30 (5) (2018), p. 051902.
- [77] X. Yin, T. Thomas, and J. Zhang. “Multiple Red Blood Cell Flows through Microvascular Bifurcations: Cell Free Layer, Cell Trajectory, and Hematocrit Separation”. *Microvasc. Res.* 89 (2013), pp. 47–56.
- [78] T. Ye and L. Peng. “Motion, deformation, and aggregation of multiple red blood cells in three-dimensional microvessel bifurcations”. *Physics of Fluids* 31 (2) (2019), p. 021903.
- [79] E. Schrödinger and R. Penrose. *What is Life?: With Mind and Matter and Autobiographical Sketches*. 1st ed. Cambridge University Press, 1992. pp 76-85.
- [80] O. Baskurt, B. Neu, and H. J. Meiselman. *Red Blood Cell Aggregation*. 0th ed. CRC Press, 2011.
- [81] G. Molineux, M. A. Foote, and S. G. Elliott, eds. *Erythropoietins and Erythropoiesis: Molecular, Cellular, Preclinical, and Clinical Biology*. Basel: Birkhäuser Basel, 2006.
- [82] S. Svetina, D. Kuzman, et al. “The cooperative role of membrane skeleton and bilayer in the mechanical behaviour of red blood cells”. *Bioelectrochemistry* 62 (2) (2004), pp. 107–113.
- [83] N. Mohandas and P. G. Gallagher. “Red Cell Membrane: Past, Present, and Future”. *Blood* 112 (10) (2008), pp. 3939–3948.
- [84] Y. Kim, K. Kim, and Y. Park. “Measurement Techniques for Red Blood Cell Deformability: Recent Advances”. *Blood Cell - An Overview of Studies in Hematology*. Ed. by T. Moschandreu. InTech, 2012.
- [85] E. Evans, R. Waugh, and L. Melnik. “Elastic area compressibility modulus of red cell membrane”. *Biophysical Journal* 16 (6) (1976), pp. 585–595.
- [86] G. H. W. Lim, M. Wortis, and R. Mukhopadhyay. “Red Blood Cell Shapes and Shape Transformations: Newtonian Mechanics of a Composite Membrane”. *Soft Matter, Vol. 4: Lipid Bilayers and Red Blood Cells*. Ed. by G. Gompper and M. Schick. Soft Matter 4. Weinheim: Wiley-VCH, 2008, pp. 83–249.
- [87] F. Li, C. U. Chan, and C. D. Ohl. “Yield Strength of Human Erythrocyte Membranes to Impulsive Stretching”. *Biophysical Journal* 105 (4) (2013), pp. 872–879.

- [88] R. Skalak, N. Ozkaya, and T. C. Skalak. “Biofluid Mechanics”. *Annu. Rev. Fluid Mech.* 21 (1) (1989), pp. 167–200.
- [89] E. Evans and Y.-C. Fung. “Improved Measurements of the Erythrocyte Geometry”. *Microvasc. Res.* 4 (4) (1972), pp. 335–347.
- [90] Y.-C. Fung. *Biomechanics*. New York, NY: Springer New York, 1993.
- [91] D. C. Betticher, W. H. Reinhart, and J. Geiser. “Effect of RBC shape and deformability on pulmonary O<sub>2</sub> diffusing capacity and resistance to flow in rabbit lungs”. *Journal of Applied Physiology* 78 (3) (1995), pp. 778–783.
- [92] S. Palta, R. Saroa, and A. Palta. “Overview of the coagulation system”. *Indian Journal of Anaesthesia* 58 (5) (2014), p. 515.
- [93] P. A. Holme, U. Ørvim, et al. “Shear-Induced Platelet Activation and Platelet Microparticle Formation at Blood Flow Conditions as in Arteries With a Severe Stenosis”. *Arteriosclerosis, Thrombosis, and Vascular Biology* 17 (4) (1997), pp. 646–653.
- [94] A. Rana, E. Westein, et al. “Shear-Dependent Platelet Aggregation: Mechanisms and Therapeutic Opportunities”. *Frontiers in Cardiovascular Medicine* 6 (2019), p. 141.
- [95] N. Jeffries, M. A. Miller, et al. “What is the truth behind pump thrombosis in the HeartMate II device? A National Heart, Lung, and Blood Institute perspective based on data from the Interagency Registry for Mechanically Assisted Circulatory Support”. *The Journal of Heart and Lung Transplantation* 34 (12) (2015), pp. 1505–1510.
- [96] I. H. Jaffer, J. C. Fredenburgh, et al. “Medical device-induced thrombosis: what causes it and how can we prevent it?” *Journal of Thrombosis and Haemostasis* 13 (2015), S72–S81.
- [97] U. Nobis, A. Pries, et al. “Radial distribution of white cells during blood flow in small tubes”. *Microvascular Research* 29 (3) (1985), pp. 295–304.
- [98] G. W. Schmid-Schönbein, S. Usami, et al. “The interaction of leukocytes and erythrocytes in capillary and postcapillary vessels”. *Microvascular Research* 19 (1) (1980), pp. 45–70.
- [99] B. P. Helmke, S. N. Bremner, et al. “Mechanisms for increased blood flow resistance due to leukocytes”. *American Journal of Physiology-Heart and Circulatory Physiology* 273 (6) (1997), H2884–H2890.
- [100] M. Lasta, G. Fuchsjager-Mayrl, et al. “Effects of increased white blood cell count on retinal perfusion during hyperoxia-induced vasoconstriction”. *Microvascular Research* 83 (2) (2012), pp. 126–130.
- [101] O. Forouzan, X. Yang, et al. “Spontaneous Oscillations of Capillary Blood Flow in Artificial Microvascular Networks”. *Microvasc. Res.* 84 (2) (2012), pp. 123–132.
- [102] M. Brust, C. Schaefer, et al. “Rheology of Human Blood Plasma: Viscoelastic Versus Newtonian Behavior”. *Physical Review Letters* 110 (7) (2013), p. 078305.
- [103] A. Nans, N. Mohandas, and D. L. Stokes. “Native Ultrastructure of the Red Cell Cytoskeleton by Cryo-Electron Tomography”. *Biophys. J.* 101 (10) (2011), pp. 2341–2350.
- [104] D. Barthès-Biesel. “Motion and Deformation of Elastic Capsules and Vesicles in Flow”. *Annu. Rev. Fluid Mech.* 48 (1) (2016), pp. 25–52.

- 
- [105] T. M. Fischer, M. Stohr-Lissen, and H. Schmid-Schonbein. “The Red Cell as a Fluid Droplet: Tank Tread-like Motion of the Human Erythrocyte Membrane in Shear Flow”. *Science* 202 (4370) (1978), pp. 894–896.
- [106] T. M. Fischer. “Shape Memory of Human Red Blood Cells”. *Biophys. J.* 86 (5) (2004), pp. 3304–3313.
- [107] T. M. Fischer. “Tank-Tread Frequency of the Red Cell Membrane: Dependence on the Viscosity of the Suspending Medium”. *Biophys. J.* 93 (7) (2007), pp. 2553–2561.
- [108] T. M. Fischer and R. Korzeniewski. “Threshold Shear Stress for the Transition between Tumbling and Tank-Treading of Red Blood Cells in Shear Flow: Dependence on the Viscosity of the Suspending Medium”. *J. Fluid Mech.* 736 (2013), pp. 351–365.
- [109] T. M. Fischer and R. Korzeniewski. “Angle of Inclination of Tank-Treading Red Cells: Dependence on Shear Rate and Suspending Medium”. *Biophys. J.* 108 (6) (2015), pp. 1352–1360.
- [110] M. Abkarian, C. Lartigue, and A. Viallat. “Tank Treading and Unbinding of Deformable Vesicles in Shear Flow: Determination of the Lift Force”. *Phys. Rev. Lett.* 88 (6) (2002), p. 068103.
- [111] M. Abkarian and A. Viallat. “Vesicles and Red Blood Cells in Shear Flow”. *Soft Matter* 4 (4) (2008), pp. 653–657.
- [112] M. Abkarian, M. Faivre, and A. Viallat. “Swinging of Red Blood Cells under Shear Flow”. *Phys. Rev. Lett.* 98 (18) (2007), p. 188302.
- [113] B. Kaoui, A. Farutin, and C. Misbah. “Vesicles under Simple Shear Flow: Elucidating the Role of Relevant Control Parameters”. *Phys. Rev. E* 80 (6) (2009), p. 061905.
- [114] T. Biben and C. Misbah. “Tumbling of Vesicles under Shear Flow within an Advected-Field Approach”. *Phys. Rev. E* 67 (3) (2003), p. 031908.
- [115] T. Biben, A. Farutin, and C. Misbah. “Three-Dimensional Vesicles under Shear Flow: Numerical Study of Dynamics and Phase Diagram”. *Phys. Rev. E* 83 (3) (2011), p. 031921.
- [116] P. B. Canham. “The Minimum Energy of Bending as a Possible Explanation of the Biconcave Shape of the Human Red Blood Cell”. *J. Theor. Biol.* 26 (1) (1970), pp. 61–81.
- [117] W. Helfrich. “Elastic Properties of Lipid Bilayers: Theory and Possible Experiments”. *Zeitschrift für Naturforschung C* 28 (11) (1973), pp. 693–703.
- [118] M. Deserno. “Fluid Lipid Membranes: From Differential Geometry to Curvature Stresses”. *Chem. Phys. Lipids* 185 (2015), pp. 11–45.
- [119] G. Segré and A. Silberberg. “Radial Particle Displacements in Poiseuille Flow of Suspensions”. *Nature* 189 (4760) (1961), pp. 209–210.
- [120] G. Segré and A. Silberberg. “Behaviour of Macroscopic Rigid Spheres in Poiseuille Flow Part 2. Experimental Results and Interpretation”. *J. Fluid Mech.* 14 (1) (1962), pp. 136–157.
- [121] P. G. Saffman. “The lift on a small sphere in a slow shear flow”. *Journal of Fluid Mechanics* 22 (2) (1965), pp. 385–400.
- [122] B. P. Ho and L. G. Leal. “Inertial migration of rigid spheres in two-dimensional unidirectional flows”. *Journal of Fluid Mechanics* 65 (2) (1974), pp. 365–400.

- [123] D. Di Carlo, J. F. Edd, et al. “Particle Segregation and Dynamics in Confined Flows”. *Physical Review Letters* 102 (9) (2009), p. 094503.
- [124] H. L. Goldsmith and S. G. Mason. “Axial Migration of Particles in Poiseuille Flow”. *Nature* 190 (4781) (1961), pp. 1095–1096.
- [125] B. Kaoui, G. Ristow, et al. “Lateral Migration of a Two-Dimensional Vesicle in Unbounded Poiseuille Flow”. *Phys. Rev. E* 77 (2) (2008).
- [126] G. Couplier, B. Kaoui, et al. “Noninertial lateral migration of vesicles in bounded Poiseuille flow”. *Physics of Fluids* 20 (11) (2008), p. 111702.
- [127] R. Fåhræus. “The suspension stability of the blood”. *Physiological Reviews* 9 (2) (1929), pp. 241–274.
- [128] A. R. Pries, D. Neuhaus, and P. Gaehtgens. “Blood viscosity in tube flow: dependence on diameter and hematocrit”. *American Journal of Physiology-Heart and Circulatory Physiology* 263 (6) (1992), H1770–H1778.
- [129] A. Mantegazza, F. Clavica, and D. Obrist. “In vitro investigations of red blood cell phase separation in a complex microchannel network”. *Biomicrofluidics* 14 (1) (2020), p. 014101.
- [130] Y. Kodama, H. Aoki, et al. “In vitro analysis of blood flow in a microvascular network with realistic geometry”. *Journal of Biomechanics* 88 (2019), pp. 88–94.
- [131] A. Mantegazza, M. Ungari, et al. “Local vs. Global Blood Flow Modulation in Artificial Microvascular Networks: Effects on Red Blood Cell Distribution and Partitioning”. *Frontiers in Physiology* 11 (2020), p. 566273.
- [132] F. Clavica, A. Homsy, et al. “Red blood cell phase separation in symmetric and asymmetric microchannel networks: effect of capillary dilation and inflow velocity”. *Scientific Reports* 6 (1) (2016), p. 36763.
- [133] A. R. Pries and T. W. Secomb. “Microvascular blood viscosity in vivo and the endothelial surface layer”. *American Journal of Physiology-Heart and Circulatory Physiology* 289 (6) (2005), H2657–H2664.
- [134] Pries A R, Secomb T W, et al. “Blood flow in microvascular networks. Experiments and simulation.” *Circulation Research* 67 (4) (1990), pp. 826–834.
- [135] F. M. White. *Fluid mechanics*. 6th ed. McGraw-Hill series in mechanical engineering. New York, NY: McGraw-Hill, 2009. 862 pp.
- [136] O. Reynolds. “XXIX. An experimental investigation of the circumstances which determine whether the motion of water shall be direct or sinuous, and of the law of resistance in parallel channels”. *Philosophical Transactions of the Royal Society of London* 174 (1883), pp. 935–982.
- [137] E. M. Purcell. “Life at low Reynolds number”. *American Journal of Physics* 45 (1) (1977), pp. 3–11.
- [138] O. K. Baskurt, M. Boynard, et al. “New guidelines for hemorheological laboratory techniques”. *Clinical Hemorheology and Microcirculation* 42 (2) (2009), pp. 75–97.
- [139] A. Keidan, M. Sowter, et al. “Evaluation of HEPES and phosphate buffers for rheological studies of sickle cells”. *Clinical Hemorheology and Microcirculation* 7 (4) (2016), pp. 599–610.

- 
- [140] L. Eriksson. “On the shape of human red blood cells interacting with flat artificial surfaces — the ‘glass effect’”. *Biochimica et Biophysica Acta (BBA) - General Subjects* 1036 (3) (1990), pp. 193–201.
- [141] X. Sun and K. Cheng. “Micro-/Nano-machining through Mechanical Cutting”. *Micro-manufacturing Engineering and Technology*. Elsevier, 2015, pp. 35–59.
- [142] M. Worgull. “Hot Embossing”. *Micromanufacturing Engineering and Technology*. Elsevier, 2015, pp. 147–178.
- [143] V. Maselli, R. Osellame, et al. “Fabrication of long microchannels with circular cross section using astigmatically shaped femtosecond laser pulses and chemical etching”. *Applied Physics Letters* 88 (19) (2006), p. 191107.
- [144] A. Gillner and P. Gretzki. “Laser Micro-structuring”. *Micromanufacturing Engineering and Technology*. Elsevier, 2015, pp. 107–119.
- [145] L. K. Fiddes, N. Raz, et al. “A circular cross-section PDMS microfluidics system for replication of cardiovascular flow conditions”. *Biomaterials* 31 (13) (2010), pp. 3459–3464.
- [146] M. Raffel, J. Kompenhans, et al. *Particle Image Velocimetry A Practical Guide*. Berlin, Heidelberg: Springer-Verlag Berlin Heidelberg, 2007.
- [147] A. Guckenberger, A. Kihm, et al. “Numerical–experimental observation of shape bistability of red blood cells flowing in a microchannel”. *Soft Matter* 14 (11) (2018), pp. 2032–2043.
- [148] E. Henry, S. H. Holm, et al. “Sorting cells by their dynamical properties”. *Scientific Reports* 6 (1) (2016), p. 34375.
- [149] T. Ye, N. Phan-Thien, et al. “A file of red blood cells in tube flow: A three-dimensional numerical study”. *Journal of Applied Physics* 116 (12) (2014), p. 124703.
- [150] L. Lanotte, J. Mauer, et al. “Red cells’ dynamic morphologies govern blood shear thinning under microcirculatory flow conditions”. *Proceedings of the National Academy of Sciences* 113 (47) (2016), pp. 13289–13294.
- [151] B. Cui, H. Diamant, and B. Lin. “Screened Hydrodynamic Interaction in a Narrow Channel”. *Phys. Rev. Lett.* 89 (18) (2002), p. 188302.
- [152] A. Guckenberger, M. P. Schraml, et al. “On the Bending Algorithms for Soft Objects in Flows”. *Comput. Phys. Commun.* 207 (2016), pp. 1–23.
- [153] J. C. A. Cluitmans, V. Chokkalingam, et al. “Alterations in Red Blood Cell Deformability during Storage: A Microfluidic Approach”. *BioMed Research International* 2014 (2014), pp. 1–9.
- [154] Y. Suzuki, N. Tateishi, et al. “Deformation of Erythrocytes in Microvessels and Glass Capillaries: Effects of Erythrocyte Deformability”. *Microcirculation* 3 (1) (1996), pp. 49–57.
- [155] S. Quint, A. F. Christ, et al. “3D tomography of cells in micro-channels”. *Applied Physics Letters* 111 (10) (2017), p. 103701.
- [156] A. Kihm, L. Kaestner, et al. “Classification of red blood cell shapes in flow using outlier tolerant machine learning”. *PLOS Computational Biology* 14 (6) (2018). Ed. by I. V. Pivkin, e1006278.

- [157] O. Alvarez, N. S. Montague, et al. “Quantification of Sickle Cells in the Peripheral Smear as a Marker of Disease Severity”. *Fetal and Pediatric Pathology* 34 (3) (2015), pp. 149–154.
- [158] D. I. Rubin and J. R. Daube, eds. *Clinical neurophysiology*. Fourth edition. Contemporary neurology series 92. Oxford ; New York: Oxford University Press, 2016. 991 pp.
- [159] R. Rojas. *Neural networks: a systematic introduction*. Berlin ; New York: Springer-Verlag, 1996. 502 pp.
- [160] F. Rosenblatt. “The perceptron: A probabilistic model for information storage and organization in the brain.” *Psychological Review* 65 (6) (1958), pp. 386–408.
- [161] P. Lee, S. Hui, and A. Fong. “Neural networks for web content filtering”. *IEEE Intelligent Systems* 17 (5) (2002), pp. 48–57.
- [162] G. Hinton, L. Deng, et al. “Deep Neural Networks for Acoustic Modeling in Speech Recognition: The Shared Views of Four Research Groups”. *IEEE Signal Processing Magazine* 29 (6) (2012), pp. 82–97.
- [163] D. C. Cireşan, U. Meier, et al. “High-Performance Neural Networks for Visual Object Classification”. *arXiv:1102.0183 [cs]* (2011). arXiv: 1102.0183.
- [164] B. J. Bain. *Blood cells: a practical guide*. Fifth edition. Chichester, West Sussex ; Hoboken, NJ: John Wiley & Sons Ltd, 2015.
- [165] P. Ehrlich. *Farbenanalytische Untersuchungen zur Histologie und Klinik des Blutes: gesammelte Mitteilungen*. Berlin, Germany: August Hirschwald, 1891.
- [166] M. Xu, D. P. Papageorgiou, et al. “A deep convolutional neural network for classification of red blood cells in sickle cell anemia”. *PLOS Computational Biology* 13 (10) (2017). Ed. by Q. Nie, e1005746.
- [167] N. Meng, H. K. H. So, and E. Y. Lam. “Computational single-cell classification using deep learning on bright-field and phase images”. *2017 Fifteenth IAPR International Conference on Machine Vision Applications (MVA)*. 2017 Fifteenth IAPR International Conference on Machine Vision Applications (MVA). Nagoya, Japan: IEEE, 2017, pp. 190–193.
- [168] R. K. Tripathy, S. Mahanta, and S. Paul. “Artificial intelligence-based classification of breast cancer using cellular images”. *RSC Advances* 4 (18) (2014), p. 9349.
- [169] R. W. Oei, G. Hou, et al. “Convolutional neural network for cell classification using microscope images of intracellular actin networks”. *PLOS ONE* 14 (3) (2019). Ed. by D. Horvath, e0213626.
- [170] G. Apostolopoulos, S. Tsinopoulos, and E. Dermatas. “Recognition and Identification of Red Blood Cell Size Using Angular Radial Transform and Neural Networks”. *XII Mediterranean Conference on Medical and Biological Engineering and Computing 2010*. Ed. by P. D. Bamidis and N. Pallikarakis. Red. by R. Magjarevic. Vol. 29. Berlin, Heidelberg: Springer Berlin Heidelberg, 2010, pp. 707–710.
- [171] F. L. Kriegel, R. Köhler, et al. “Cell shape characterization and classification with discrete Fourier transforms and self-organizing maps: Cell Shape Characterization and Classification”. *Cytometry Part A* 93 (3) (2018), pp. 323–333.
- [172] G. Simionato, K. Hinkelmann, et al. “Artificial neural networks for 3D cell shape recognition from confocal images”. *arXiv:2005.08040 [eess, q-bio]* (2020). arXiv: 2005.08040.

- 
- [173] I. Goodfellow, Y. Bengio, and A. Courville. *Deep learning*. Adaptive computation and machine learning. Cambridge, Massachusetts: The MIT Press, 2016. 775 pp.
- [174] F. Chollet. *Deep learning with Python*. Shelter Island, New York: Manning Publications Co, 2018. 361 pp.
- [175] K. P. Murphy. *Machine learning: a probabilistic perspective*. Adaptive computation and machine learning series. Cambridge, MA: MIT Press, 2012. 1067 pp.
- [176] N. Qian. “On the momentum term in gradient descent learning algorithms”. *Neural Networks: The Official Journal of the International Neural Network Society* 12 (1) (1999), pp. 145–151.
- [177] R. A. Jacobs. “Increased rates of convergence through learning rate adaptation”. *Neural Networks* 1 (4) (1988), pp. 295–307.
- [178] C. M. Bishop. *Pattern recognition and machine learning*. Information science and statistics. New York: Springer, 2006. 738 pp.
- [179] M. Kubat. *An introduction to machine learning*. Cham Heidelberg New York Dordrecht London: Springer, 2015. 291 pp.
- [180] T. Hastie, R. Tibshirani, and J. Friedman. *The Elements of Statistical Learning*. Springer Series in Statistics. New York, NY: Springer New York, 2009.
- [181] D. Masters and C. Luschi. “Revisiting Small Batch Training for Deep Neural Networks”. *arXiv:1804.07612 [cs, stat]* (2018). arXiv: 1804.07612.
- [182] Y. Bengio. “Practical recommendations for gradient-based training of deep architectures”. *arXiv:1206.5533 [cs]* (2012). arXiv: 1206.5533.
- [183] A. Krizhevsky, I. Sutskever, and G. E. Hinton. “ImageNet classification with deep convolutional neural networks”. *Communications of the ACM* 60 (6) (2017), pp. 84–90.
- [184] A. Kihm, S. Quint, et al. “Lingering Dynamics in Microvascular Blood Flow”. *Biophysical Journal* 120 (3) (2021), pp. 432–439.
- [185] A. S. Popel and P. C. Johnson. “Microcirculation and hemorheology”. *Annual Review of Fluid Mechanics* 37 (1) (2005), pp. 43–69.
- [186] O. Sorop, T. D. Olver, et al. “The microcirculation: a key player in obesity-associated cardiovascular disease”. *Cardiovascular Research* 113 (9) (2017), pp. 1035–1045.
- [187] S. M. Factor. “Pathology and Pathophysiology of the Coronary Microcirculation in Myocardial Ischemia”. *The Stressed Heart*. Ed. by M. J. Legato. Vol. 62. Boston, MA: Springer US, 1987, pp. 125–147.
- [188] H. Tillmanns, H. Leinberger, et al. “Microcirculation in Myocardial Ischemia and Reperfusion”. *Reperfusion and Revascularization in Acute Myocardial Infarction*. Ed. by G. Schettler, R. B. Jennings, et al. Berlin, Heidelberg: Springer Berlin Heidelberg, 1988, pp. 46–51.
- [189] C. Bächer, A. Kihm, et al. “Antimargination of Microparticles and Platelets in the Vicinity of Branching Vessels”. *Biophysical Journal* 115 (2) (2018), pp. 411–425.
- [190] C. Pozrikidis. “Numerical Simulation of Blood Flow Through Microvascular Capillary Networks”. *Bulletin of Mathematical Biology* 71 (6) (2009), pp. 1520–1541.
- [191] P. Bagchi. “Mesoscale Simulation of Blood Flow in Small Vessels”. *Biophysical Journal* 92 (6) (2007), pp. 1858–1877.

- [192] P. Balogh and P. Bagchi. “A computational approach to modeling cellular-scale blood flow in complex geometry”. *Journal of Computational Physics* 334 (2017), pp. 280–307.
- [193] L. Kaestner. *Calcium signalling Approaches and Findings in the Heart and Blood*. Berlin, Heidelberg: Springer Berlin Heidelberg, 2013.
- [194] J. Poiseuille. *Recherches sur les causes du mouvement du sang dans les veines*. 1832.
- [195] A. R. Pries, T. W. Secomb, et al. “Resistance to blood flow in microvessels in vivo.” *Circulation Research* 75 (5) (1994), pp. 904–915.
- [196] I. G. Gould, P. Tsai, et al. “The capillary bed offers the largest hemodynamic resistance to the cortical blood supply”. *Journal of Cerebral Blood Flow & Metabolism* 37 (1) (2017), pp. 52–68.
- [197] G. S. Kassab. *Coronary Circulation: Anatomy, Mechanical Properties, and Biomechanics*. Cham: Springer International Publishing, 2019.
- [198] B. Gunnar Wallin. “Neural control of human skin blood flow”. *Journal of the Autonomic Nervous System* 30 (1990), S185–S190.
- [199] A. Sato, K. Terata, et al. “Mechanism of vasodilation to adenosine in coronary arterioles from patients with heart disease”. *American Journal of Physiology-Heart and Circulatory Physiology* 288 (4) (2005), H1633–H1640.
- [200] B. Fromy, S. Merzeau, et al. “Mechanisms of the cutaneous vasodilator response to local external pressure application in rats: involvement of CGRP, neurokinins, prostaglandins and NO”. *British Journal of Pharmacology* 131 (6) (2000), pp. 1161–1171.
- [201] C. D. Murray. “The Physiological Principle of Minimum Work: II. Oxygen Exchange in Capillaries”. *Proceedings of the National Academy of Sciences* 12 (5) (1926), pp. 299–304.
- [202] K. A. McCulloh, J. S. Sperry, and F. R. Adler. “Water transport in plants obeys Murray’s law”. *Nature* 421 (6926) (2003), pp. 939–942.
- [203] A. R. Pries, B. Reglin, and T. W. Secomb. “Structural response of microcirculatory networks to changes in demand: information transfer by shear stress”. *American Journal of Physiology-Heart and Circulatory Physiology* 284 (6) (2003), H2204–H2212.
- [204] J. B. Bassingthwaighe, L. S. Liebovitch, and B. J. West. *Fractal Physiology*. New York, NY: Springer New York, 1994.
- [205] K. Ley, A. Pries, and P. Gaehtgens. “Topological structure of rat mesenteric microvessel networks”. *Microvascular Research* 32 (3) (1986), pp. 315–332.
- [206] R. Potter and A. Groom. “Capillary diameter and geometry in cardiac and skeletal muscle studied by means of corrosion casts”. *Microvascular Research* 25 (1) (1983), pp. 68–84.
- [207] T. W. Secomb, J. P. Alberding, et al. “Angiogenesis: An Adaptive Dynamic Biological Patterning Problem”. *PLoS Computational Biology* 9 (3) (2013). Ed. by C. D. Little, e1002983.
- [208] M. Zygmunt, F. Herr, et al. “Angiogenesis and vasculogenesis in pregnancy”. *European Journal of Obstetrics & Gynecology and Reproductive Biology*. The Regulation of Fetal Growth, Fetal Oxygen Supply and Intrauterine Development 110 (2003), S10–S18.

- 
- [209] C. Morland, K. A. Andersson, et al. “Exercise induces cerebral VEGF and angiogenesis via the lactate receptor HCAR1”. *Nature Communications* 8 (1) (2017), p. 15557.
- [210] P. Wahl, F. Jansen, et al. “Effects of High Intensity Training and High Volume Training on Endothelial Microparticles and Angiogenic Growth Factors”. *PLoS ONE* 9 (4) (2014). Ed. by P. Madeddu, e96024.
- [211] M. G. Tonnesen, X. Feng, and R. A. F. Clark. “Angiogenesis in Wound Healing”. *Journal of Investigative Dermatology Symposium Proceedings* 5 (1) (2000), pp. 40–46.
- [212] M. E. Maragoudakis, P. Gullino, and P. I. Lelkes, eds. *Angiogenesis in Health and Disease*. Boston, MA: Springer US, 1992.
- [213] B. M. Prior, H. T. Yang, and R. L. Terjung. “What makes vessels grow with exercise training?” *Journal of Applied Physiology* 97 (3) (2004), pp. 1119–1128.
- [214] M. Laschke, A. Strohe, et al. “In vivo biocompatibility and vascularization of biodegradable porous polyurethane scaffolds for tissue engineering”. *Acta Biomaterialia* 5 (6) (2009), pp. 1991–2001.
- [215] M. W. Laschke, B. Vollmar, et al. “The dorsal skinfold chamber: window into the dynamic interaction of biomaterials with their surrounding host tissue”. *European Cells and Materials* 22 (2011), pp. 147–167.
- [216] L. Hertz, S. Ruppenthal, et al. “The Evolution of Erythrocytes Becoming Red in Respect to Fluorescence”. *Frontiers in Physiology* 10 (2019).
- [217] E. Limpert, W. A. Stahel, and M. Abbt. “Log-normal Distributions across the Sciences: Keys and Clues”. *BioScience* 51 (5) (2001), p. 341.
- [218] N. Mohandas and E. Evans. “Mechanical Properties of the Red Cell Membrane in Relation to Molecular Structure and Genetic Defects”. *Annual Review of Biophysics and Biomolecular Structure* 23 (1) (1994), pp. 787–818.
- [219] V. Heinrich, K. Ritchie, et al. “Elastic Thickness Compressibility of the Red Cell Membrane”. *Biophysical Journal* 81 (3) (2001), pp. 1452–1463.



# Appendix



## A List of devices and consumables

- ▶ **Phosphate buffered saline (PBS):** Thermo Fisher, Gibco, pH 7.4, 280–315 mOsm kg<sup>-1</sup>
- ▶ **Bovine serum albumin (BSA):** Thermo Fisher Scientific
- ▶ **Blood withdrawal container:** S-Monovette K3 EDTA, 9 ml, Sarstedt AG
- ▶ **High-speed camera (in vitro):** Fastec HiSpec 1, 2 GB internal memory, physical pixel size: 14 μm×14 μm, 1280 px × 1024px
- ▶ **Microscope:** Nikon TE2000-S, equipped with a 60× oil-immersion plan-apochromatic objective, NA=1.6
- ▶ **Tubing:** Scientific Commodities, Inc., Low Density Polyethylen, inner diameter: 0.9 mm, outer diameter: 1.3 mm
- ▶ **Red light illumination:** Zett Optics ZLED CLS 9000 MV-R,  $\lambda = 640 \text{ nm} \pm 20 \text{ nm}$
- ▶ **Pressure controller:** Elvexys Elveflow OB1-MkII, maximum pressure 2 bar, pressure stability 0.005 %
- ▶ **High-speed camera (in vivo):** Hamamatsu ORCA-Flash 4.0 V3, Hamamatsu Photonics K.K.



# Acknowledgments

Auch wenn die vorliegende Arbeit von einem Autor verfasst wurde, so gibt es viele Menschen, die mich auf diesem Weg begleitet, unterstützt, motiviert und getröstet haben und diese Menschen sollen hier gewürdigt werden.

Als Erstes möchte ich mich bei meinem Doktorvater Prof. Dr. Christian Wagner bedanken, der mich damals, als ich als Theoretiker durch seine Tür trat, sofort herzlich in seine Arbeitsgruppe aufgenommen hatte. Einen Mentor zu finden, der sich sowohl fachlich als auch menschlich engagiert und stets ein offenes Ohr für alle Anliegen hat, ist nicht selbstverständlich.

Herrn Prof. Dr. Rolf Pelster danke ich für die freundliche und unkomplizierte Übernahme der Aufgabe des Zweitgutachters dieser Arbeit.

In diesem Kontext möchte ich mich auch bei Prof. Dr. Maikel Rheinstädter bedanken, der mich, wie er es einmal formulierte, im Völklingen Kanadas (aber unvergleichlich schöner) mit offenen Armen empfangen hat und mich in die Welt der Neutronenbeugung und Hybrid-Membranen eingeführt hat. Auch wenn die Dauer des Aufenthaltes leider zu kurz war, so hat die Erfahrung nachhaltig mein Leben bereichert und ich möchte die Zeit nicht missen. Danke Maikel!

The past years have been a wonderful time full of joy and plenty of experiences and this is mainly due to both of my workgroups. All past and current members of the AG Wagner, Viviana Clavería, Javad Najafi, Zakaria Boujja, François Yaya, Asena Abay, Stephan Quint, Greta Simionato, Steffen Recktenwald, Yazdan Rashidi, Julia Jansen, Christian Ruloff, Alexey Semenov, Thomas Fischer, Matthias Paulus, Alexis Darras, Nils Boussard, Andreas Tschöpe, Jorge Fiscina, Felix Maurer, Oliver Köhn, Daniel Flormann, Julie Martin-Wortham, Mohammed Nouaman, Mohammed Bendaoud, Bernd Eberle, and Revaz Chachanidze. In Canada, I wish to thank Renée-Claude Bider, Dylan Jacob Malenfant, Matthew Blacker, Gaurav Ambwani, Mughda Khondker, and Sebastian Himbert. Sebastian, thank you so much for everything!

Achim Guckenberger, Katharina Grässel und Stephan Gekle von der Biofluid modeling and simulation group in Bayreuth möchte ich herzlich für die tolle Zusammenarbeit danken!

Besonders hervorheben möchte ich an dieser Stelle Prof. Dr. Lars Kästner, der mich in die faszinierende Welt der Akanthozytose inkl. vieler schöner Bluttransporte durch die gesamte Republik begleitet hat und mir durch sein schier unendliches Wissen über alles, was rote Blutzellen angeht, immer behilflich sein konnte. Ebenso möchte ich Dr. Thomas John danken für seine Hilfe in (programmier-) technischen Fragen und für viele fachliche und witzige Diskussionen, auch abseits der Physik.

Eine so interdisziplinäre Gruppe funktioniert natürlich nur mit der richtigen Organisation. Karin Kretsch danke ich für die kompetente und schnelle Anfertigung aller Proben und Lösungen, die ich selbst garantiert falsch gemischt hätte und dafür, dass sie meine fragwürdigen

Vorschläge bzgl. der Laborsicherheit stets mit einem Lachen quittiert hat. Elke Huschens hat durch ihre lebendige Art schon früh am Morgen für gute Laune gesorgt und wusste stets Rat bei jeglicher Art von bürokratischen Hürden. Genieße deinen wohlverdienten Ruhestand! Nina Apfelbaum führt dieses Werk mit großem Eifer fort und auch dir, Nina, gebührt hierfür mein größter Dank.

Rishab, mein Bruder, was soll ich sagen außer: Ohleck, ey!

Maître Schmidt und der gesamten Werkstatt möchte ich für die schnelle Umsetzungen aller Arbeiten danken und für die vielen „letzten Schichten“. Michael danke ich darüber hinaus für die im wahrsten Sinne des Wortes kulinarischen „Grenz“-Erfahrungen und die gastrosophischen Diskurse mit Dr. Heinz Schmitt bei einem guten Kaffee!

Eva Nossem danke ich für die Korrektur aller sprachlichen Fehler die sich in dieser Arbeit eingeschlichen haben und die dem Auge des Naturwissenschaftlers verborgen geblieben wären.

Henning, Felix, Matze und Christian: Danke, dass ihr mich immer geerdet und für Unterhaltung abseits der Physik gesorgt habt.

Meinen Eltern Gaby und Rainer danke ich für ihre bedingungslose Liebe und Unterstützung in jeglicher Hinsicht, ohne die all das niemals möglich gewesen wäre!

Myriam, grazie di cuore per esserci nella mia vita! Mi rendi una persona migliore e mi dai l'amore e la forza senza i quali non ce l'avrei mai fatta ad arrivare a questo punto. Sei l'amore della mia vita!